

Supporting Information for “Mantle Wavespeed and Discontinuity Structure below East Africa: Implications for Cenozoic Hotspot Tectonism and the Development of the Turkana Depression”

A. Boyce^{1*}, R. Kounoudis², I. D. Bastow², S. Cottaar¹, C. J. Ebinger³, C. S. Ogden^{2,4}

¹University of Cambridge, Department of Earth Science, Bullard Laboratories, Madingley Road, Cambridge, CB3 0EZ, UK.

²Department of Earth Science and Engineering, Royal School of Mines, Prince Consort Road, Imperial College London, London, SW7 2BP, UK.

³Department of Earth and Environmental Sciences, Tulane University, New Orleans, LA 70118, USA.

⁴School of Geography and Geology, University of Leicester, Leicester, LE1 7RH, UK

*Present Address: Université Claude Bernard Lyon 1, ENS de Lyon, CNRS, UMR 5276 LGL-TPE, F-69622, Villeurbanne, France.

Corresponding author: Alistair Boyce, alistair.boyce@univ-lyon1.fr

Contents of this file

1. Introduction
2. The Global Data set
3. Direct P-wave Absolute Arrival-time Residuals
4. Relative Arrival-time Analysis
5. Absolute Arrival-time Analysis
6. Crustal Corrections
7. Adaptive Parameterization
8. Trade-off Curve Approach
9. Regional Scale Resolution Tests
10. Broad Scale Resolution Tests
11. Checkerboard Resolution Tests
12. Ray Path Masking
13. AFRP22 Model
14. 3-D Model Volume Plots
15. P-wave Model Comparison
16. Receiver Function Data set
17. Regional MTZ Depth and Slowness Stacks
18. ak135-CCP: 1D Depth Correction and CCP Stack
19. Quantitative Depth Correction Assessment
20. 3D Depth Correction and CCP Stacks
21. AFRP22-CCP Frequency Testing
22. Mantle Transition Zone Discontinuity Values
23. References

Introduction

This electronic supplement documents material relating to the absolute P-wavespeed seismic tomographic approach and the mantle transition zone receiver function imaging method.

A digital model file of the AFRP22 tomographic model with and without the crustal correction is available at <https://ds.iris.edu/ds/products/emc-afrp22/>. The ray path mask

described in Section ‘Ray Path Masking’ is also available. The code used to determine this mask is accessible at https://github.com/alistairboyce11/Ray_path_mask (see: Boyce et al., 2021). The raw data files, processed data, inversion software package and plotting codes will be available, following lifting of data embargo, on 2024-05-24 at <https://doi.org/10.5281/zenodo.7607098>.

The file *Boyce_et_al_Africa_RF_s_MTZ_thickness.txt* distributed alongside the main manuscript provides picked mantle transition zone (MTZ) thickness below Africa obtained from this study. Values are derived from AFRP22-CCP and SGLOBEani-CCP that combine Pds, PPds, PKPds receiver function (RF) data corrected to depth using the SGLOBEani (Chang et al., 2015) and AFRP22 tomographic models (this manuscript). RFs are calculated up to a maximum frequency of 0.2 Hz. Results are only provided for regions where stacking weight is greater than 2 (Figure S47) and relative amplitude is greater than two standard error from the mean.

The Global Data set

The earthquake and station locations used in the tomographic inversion are shown in Figures S1 and S2. Phase picks from the EHB Bulletin can be accessed at <http://www.isc.ac.uk/ehbulletin/>.

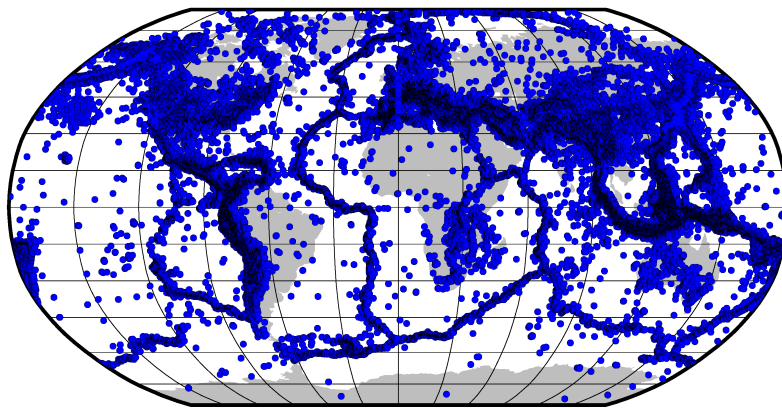


Figure S1. Map of earthquakes derived from the EHB Bulletin (see Li et al., 2008) supplemented with data from Boyce et al. (2021) and teleseismic earthquakes recorded across Africa in this study.

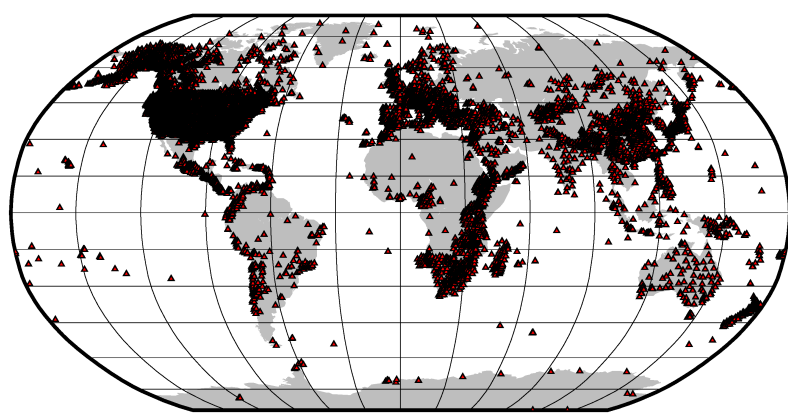


Figure S2. Map of seismograph stations derived from the EHB Bulletin (see Li et al., 2008) supplemented with data from Boyce et al. (2021) and seismograph networks across Africa used in this study.

Direct P-wave Absolute Arrival-time Residuals

Direct-P phase mean absolute arrival-time residuals for stations in the “EHB” database (Engdahl et al., 1998) used by Li et al. (2008), stations processed by Boyce et al. (2021) and new African data processed here (see main manuscript). Additional constraints on the crust and deep mantle are provided by other phases that are not plotted here (e.g., Pn, Pg, pP, PKP and PKIKP).

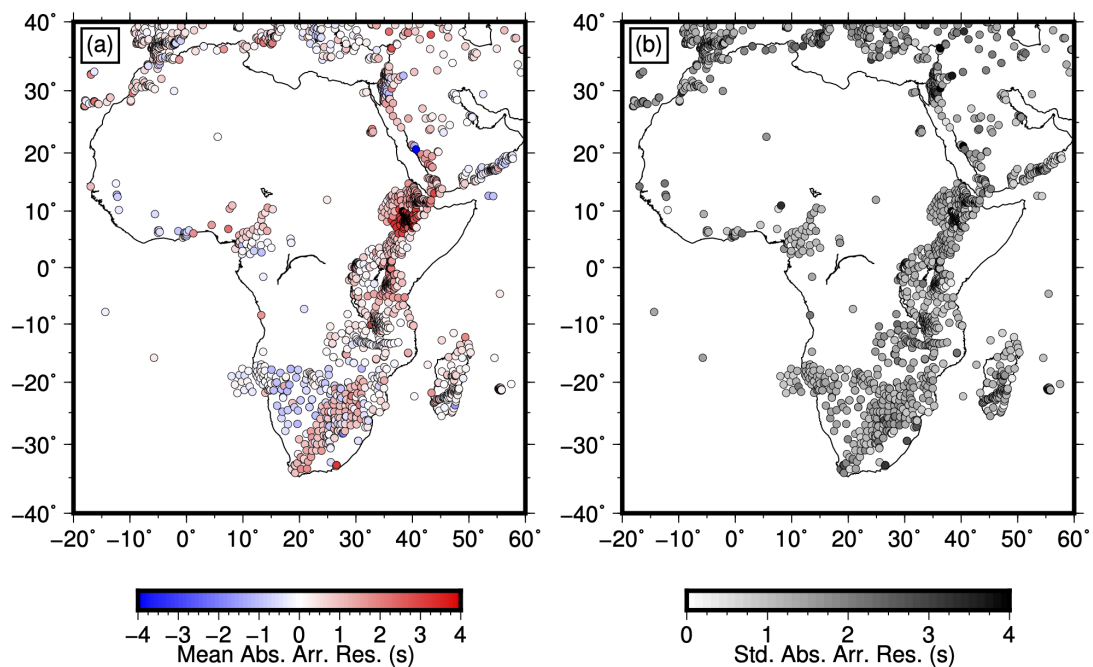


Figure S3. Maps of mean (a) and standard deviation (b) of the direct-P phase absolute arrival-time residuals for African stations. The data set includes residuals from the “EHB” database (Engdahl et al., 1998) used by Li et al. (2008), stations processed by Boyce et al. (2021) and new African data added here (see main manuscript). African “EHB” stations contribute 179,418 direct P-wave arrival-times, data from Boyce et al. (2021) contributes 87,184 arrival-times and our new data contributes 13,455 arrival times. Residuals are corrected for ellipticity and topography.

Relative Arrival-time Analysis

We collect vertical component broadband seismic data from four recently deployed seismic networks across Africa (2011–2020), that significantly improve upon the spatial coverage of Boyce et al. (2021). We follow the identical data processing procedure adopted by Boyce et al. (2021) and initially divide the data up into 4 regions, namely; Turkana Depression, Uganda, Mozambique and Namibia (Figure S4). We use Multi-Channel Cross-correlation (VanDecar & Crosson, 1990) to first calculate direct P-phase relative arrival-time residuals from these networks separately.

For the TRAILS network in Turkana we obtain 13,395 picks from 928 earthquakes recorded at 35 stations. For the Ugandan network we obtain 3,328 picks from 534 earthquakes recorded at 10 stations. For the Mozambique network we obtain 984 picks from 143 earthquakes recorded at 28 stations. For the Namibian network we obtain 1,689 picks from 228 earthquakes recorded at 19 stations. Results are presented in Figures S5–S8. We follow the same process to collect a further total 2,061 PKP, PKIKP and PKiKP phase relative-arrival times from networks in Uganda and Turkana (Nyblade, 2017; Ebinger, 2018; Bastow, 2019).

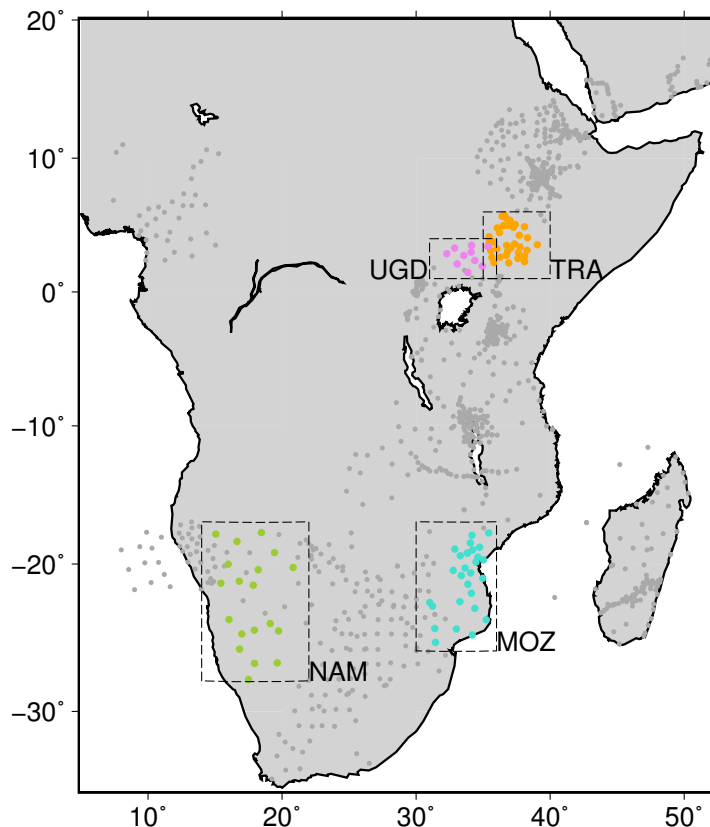


Figure S4. Map of seismic stations across Africa processed separately (Figures S5–S8), colored by sub region. Dark gray circles show locations of stations used by Boyce et al. (2021). TRA (orange circles): TRAILS network in the Turkana Depression (Ebinger, 2018; Bastow, 2019; Kounoudis et al., 2021), UGD (pink circles): Ugandan network (Nyblade, 2017; Andriampeno-manana et al., 2021), MOZ (cyan circles): Mozambique network (Helffrich & Fonseca, 2011; Fonseca et al., 2014), NAM (green circles): Namibian network (Durrheim & Nyblade, 2009; Nyblade, 2015).

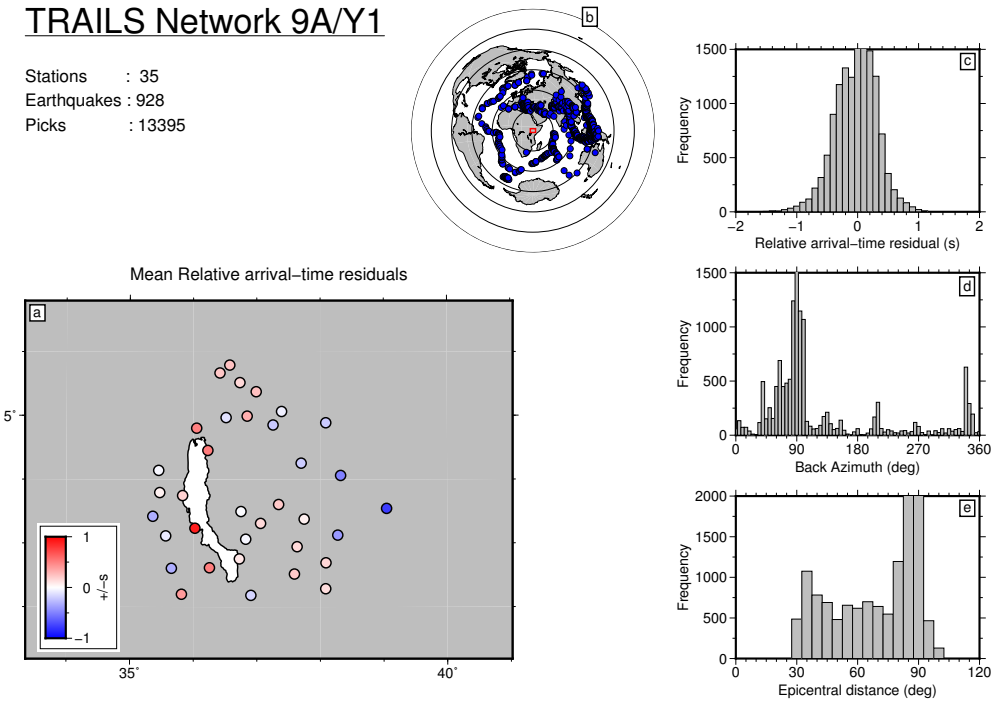


Figure S5. For the TRAILS network data set in the Turkana Depression: (a) Station mean direct P-wave relative arrival-time residuals extracted using Multi-channel cross-correlation (VanDecar & Crosson, 1990). (b) Map of magnitude $m_b >4.0$ teleseismic earthquakes recorded from 2019–2020 (blue dots). Earthquakes are recorded with adequate SNR at a minimum of 4 stations. Concentric rings are separated by 30° epicentral distance increments from network center. (c) Relative arrival-time residual distribution. (d) Back-azimuthal residual distribution. (e) Epicentral distance residual distribution.

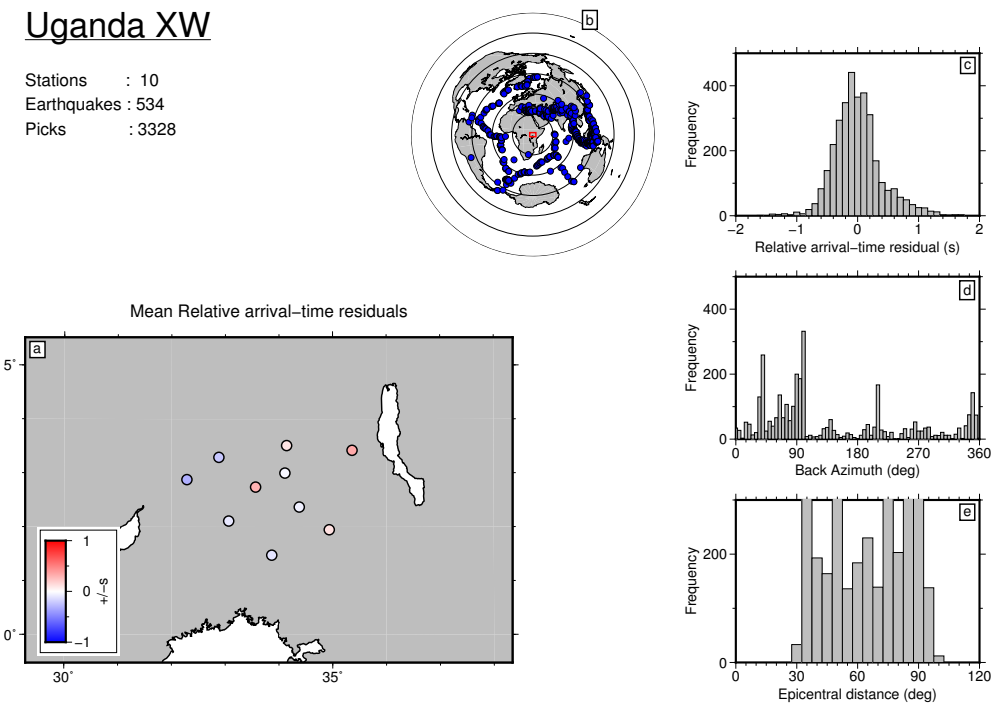


Figure S6. For the Ugandan data set: (a) Station mean direct P-wave relative arrival-time residuals extracted using Multi-channel cross-correlation (VanDecar & Crosson, 1990). (b) Map of magnitude $m_b > 4.0$ teleseismic earthquakes recorded from 2017–2018 (blue dots). Earthquakes are recorded with adequate SNR at a minimum of 4 stations. Concentric rings are separated by 30° epicentral distance increments from network center. (c) Relative arrival-time residual distribution. (d) Back-azimuthal residual distribution. (e) Epicentral distance residual distribution.

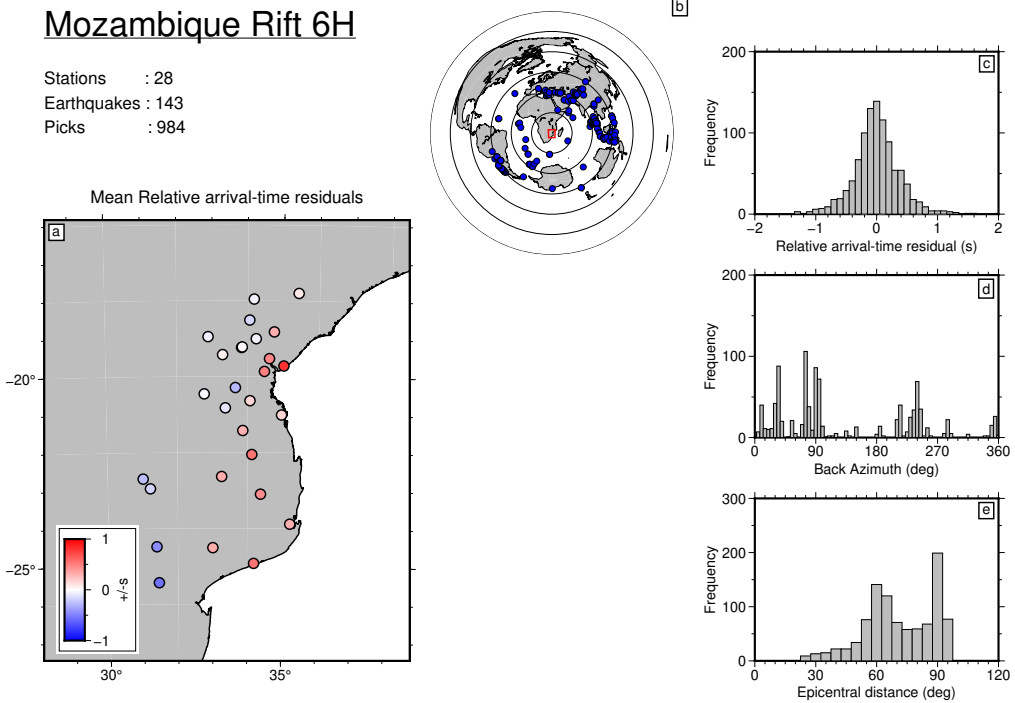


Figure S7. For the Mozambique data set: (a) Station mean direct P-wave relative arrival-time residuals extracted using Multi-channel cross-correlation (VanDecar & Crosson, 1990). (b) Map of magnitude $m_b > 5.5$ teleseismic earthquakes recorded from 2011–2013 (blue dots). Earthquakes are recorded with adequate SNR at a minimum of 4 stations. Concentric rings are separated by 30° epicentral distance increments from network center. (c) Relative arrival-time residual distribution. (d) Back-azimuthal residual distribution. (e) Epicentral distance residual distribution.

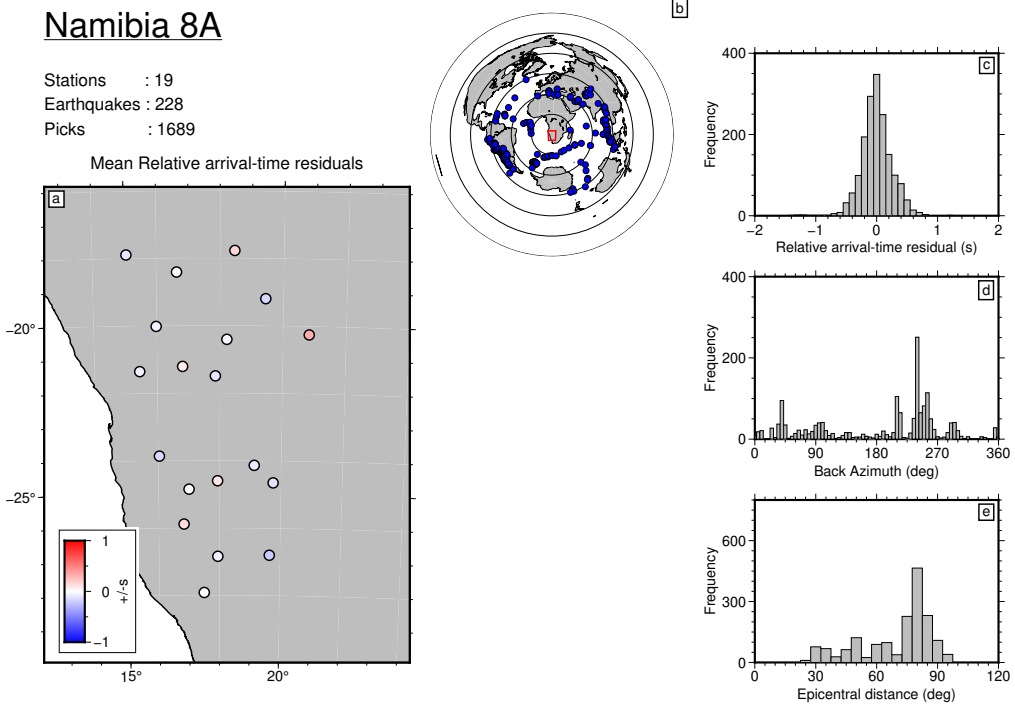


Figure S8. For the Namibian data set: (a) Station mean direct P-wave relative arrival-time residuals extracted using Multi-channel cross-correlation (VanDecar & Crosson, 1990). (b) Map of magnitude $m_b > 5.5$ teleseismic earthquakes recorded from 2015–2018 (blue dots). Earthquakes are recorded with adequate SNR at a minimum of 4 stations. Concentric rings are separated by 30° epicentral distance increments from network center. (c) Relative arrival-time residual distribution. (d) Back-azimuthal residual distribution. (e) Epicentral distance residual distribution.

Absolute Arrival-time Analysis

We process relative arrival-times derived from regional seismic networks using the Absolute Arrival-time Recovery Method (AARM - see Boyce et al., 2017), to extract absolute arrival-times. This procedure yields 9,184 direct-P phase absolute arrival-time picks for the TRAILS network in the Turkana Depression, 1,971 for Uganda, 850 for Mozambique and 1,450 for Namibia (Figures S9–S12). We obtain a further 1,299 PKP, PKIKP and PKiKP phase absolute-arrival times from networks in Uganda and Turkana following the same process.

Figures S9–S12 show statistics for AARM derived picks for each of the four sub regions shown in Figure S4. Sub-figures (*a,d*) show distribution of individual waveform pick error and absolute arrival-time. Sub-figures (*b,c,e*) show a variety of metrics used to assess the robustness of picks on an event-by-event basis by tracking properties of the waveform stacks on which the picks were made. For more detail, please see Boyce et al. (2017).

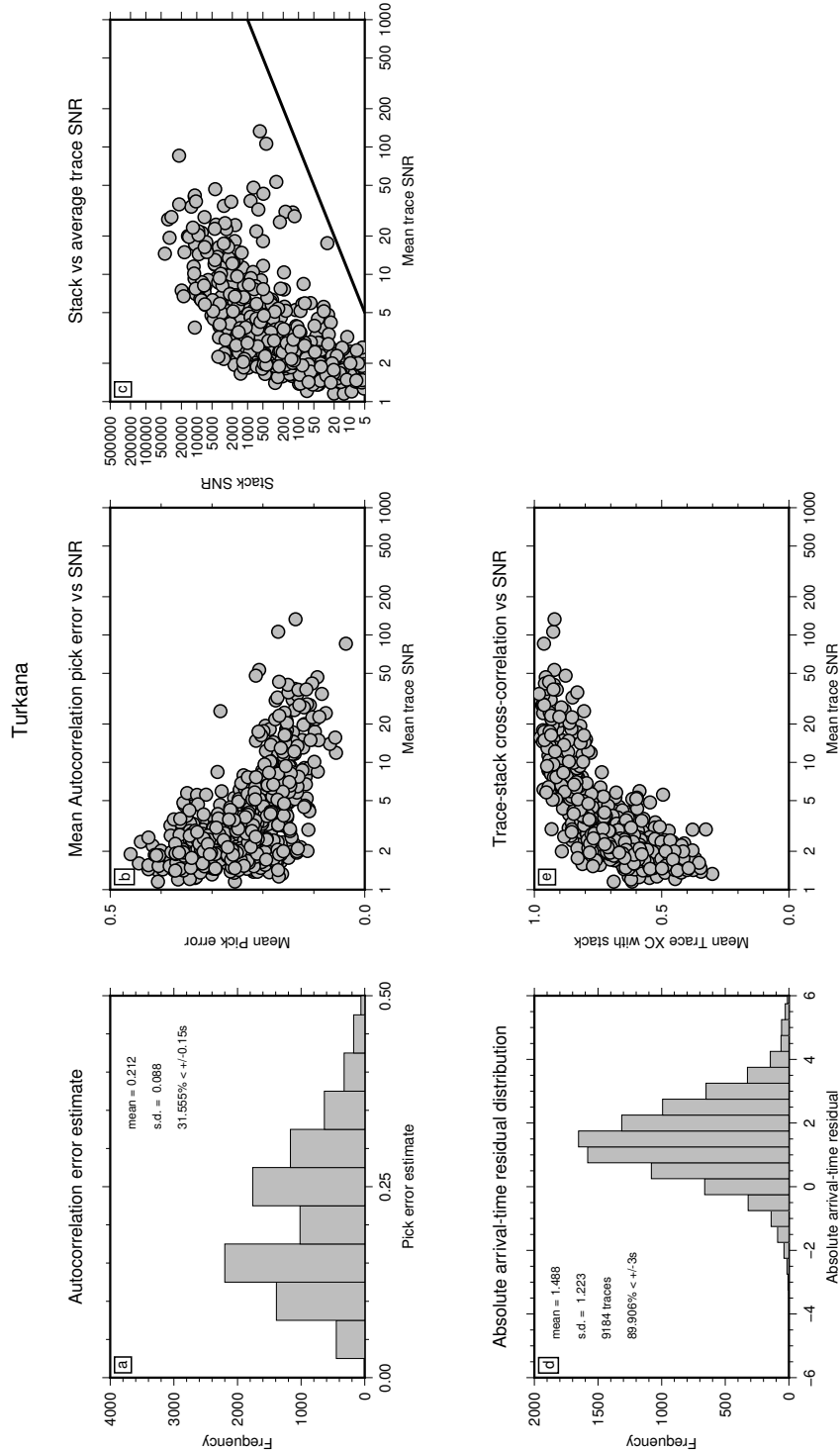


Figure S9. For the TRAILS network data set in the Turkana Depression (Ebinger, 2018; Bastow, 2019; Kounoudis et al., 2021): (a) Autocorrelation pick error estimates for each arrival-time. (b) For each earthquake, mean autocorrelation pick error plotted against mean trace SNR. (c) For each earthquake, stacked trace SNR against mean trace SNR. $y=x$ (black line). (d) Absolute arrival-time residual distribution. (e) For each earthquake, mean trace–stack cross-correlation coefficient against mean trace SNR.

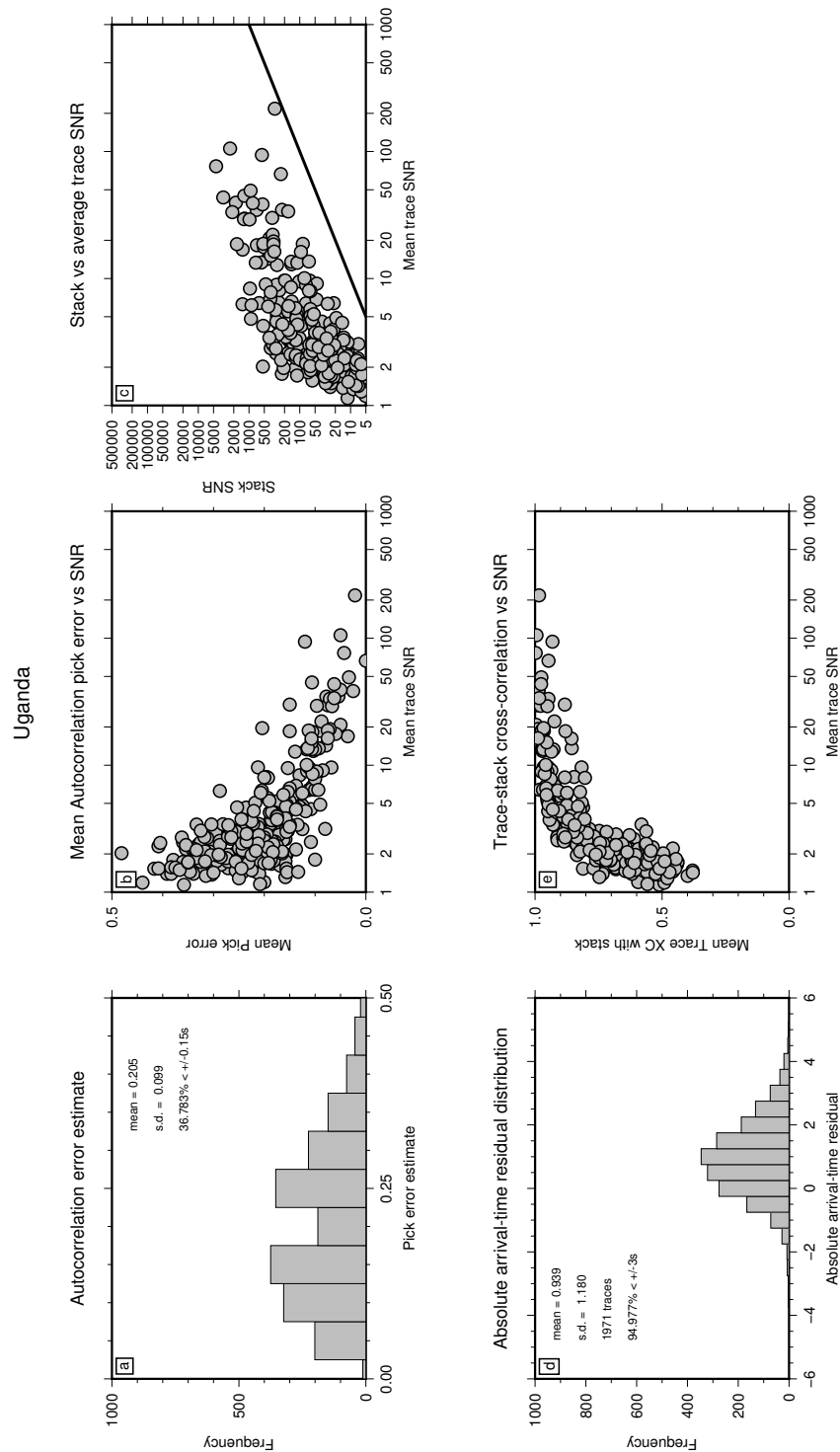


Figure S10. For the Ugandan data set (Nyblade, 2017; Andriampenomanana et al., 2021):

- (a) Autocorrelation pick error estimates for each arrival-time.
- (b) For each earthquake, mean autocorrelation pick error plotted against mean trace SNR.
- (c) For each earthquake, stacked trace SNR against mean trace SNR. $y=x$ (black line).
- (d) Absolute arrival-time residual distribution.
- (e) For each earthquake, mean trace–stack cross-correlation coefficient against mean trace SNR.

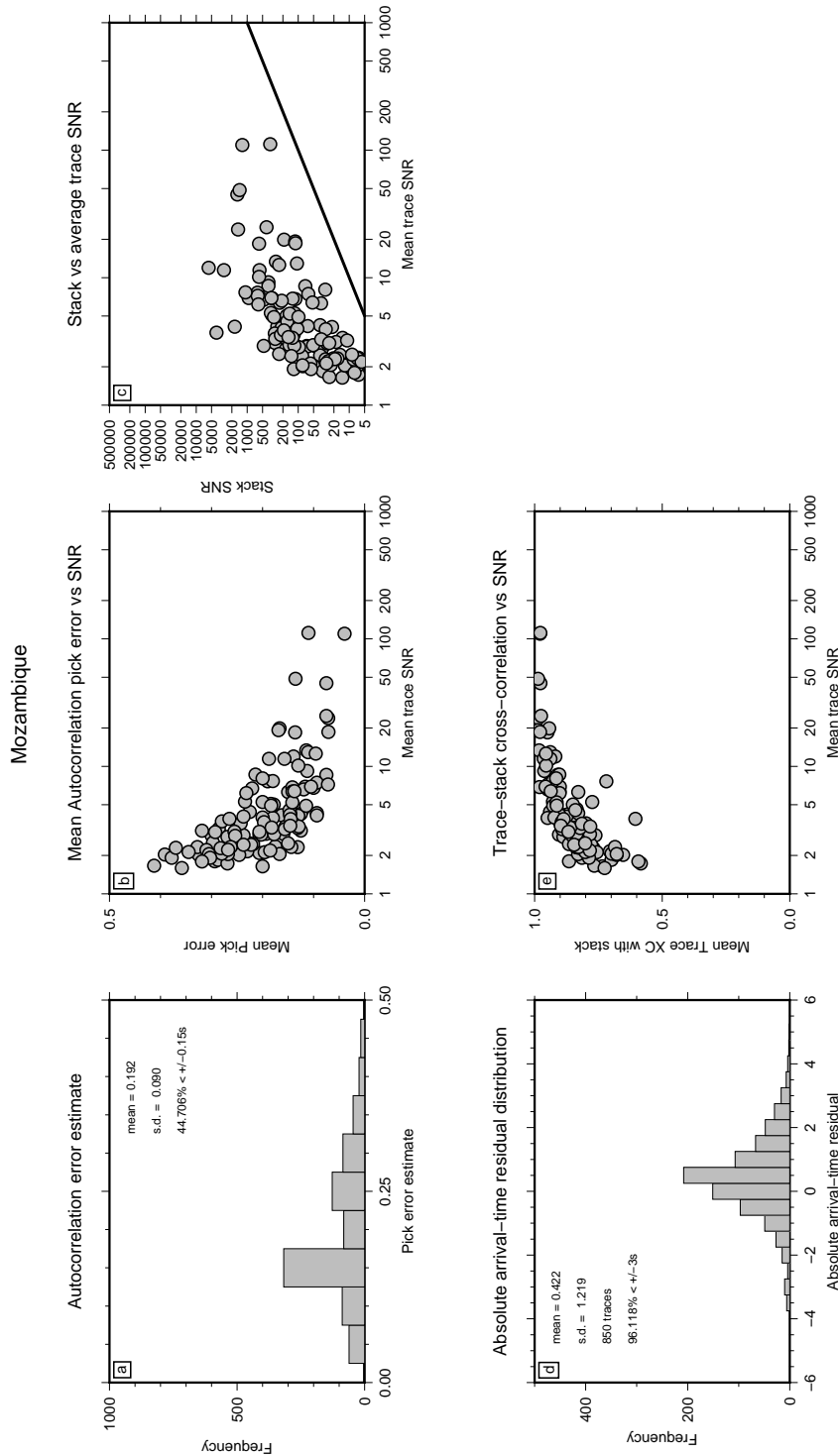


Figure S11. For the Mozambique data set (Helffrich & Fonseca, 2011; Fonseca et al., 2014):
 (a) Autocorrelation pick error estimates for each arrival-time. (b) For each earthquake, mean autocorrelation pick error plotted against mean trace SNR. (c) For each earthquake, stacked trace SNR against mean trace SNR. y=x (black line). (d) Absolute arrival-time residual distribution.
 (e) For each earthquake, mean trace–stack cross-correlation coefficient against mean trace SNR.

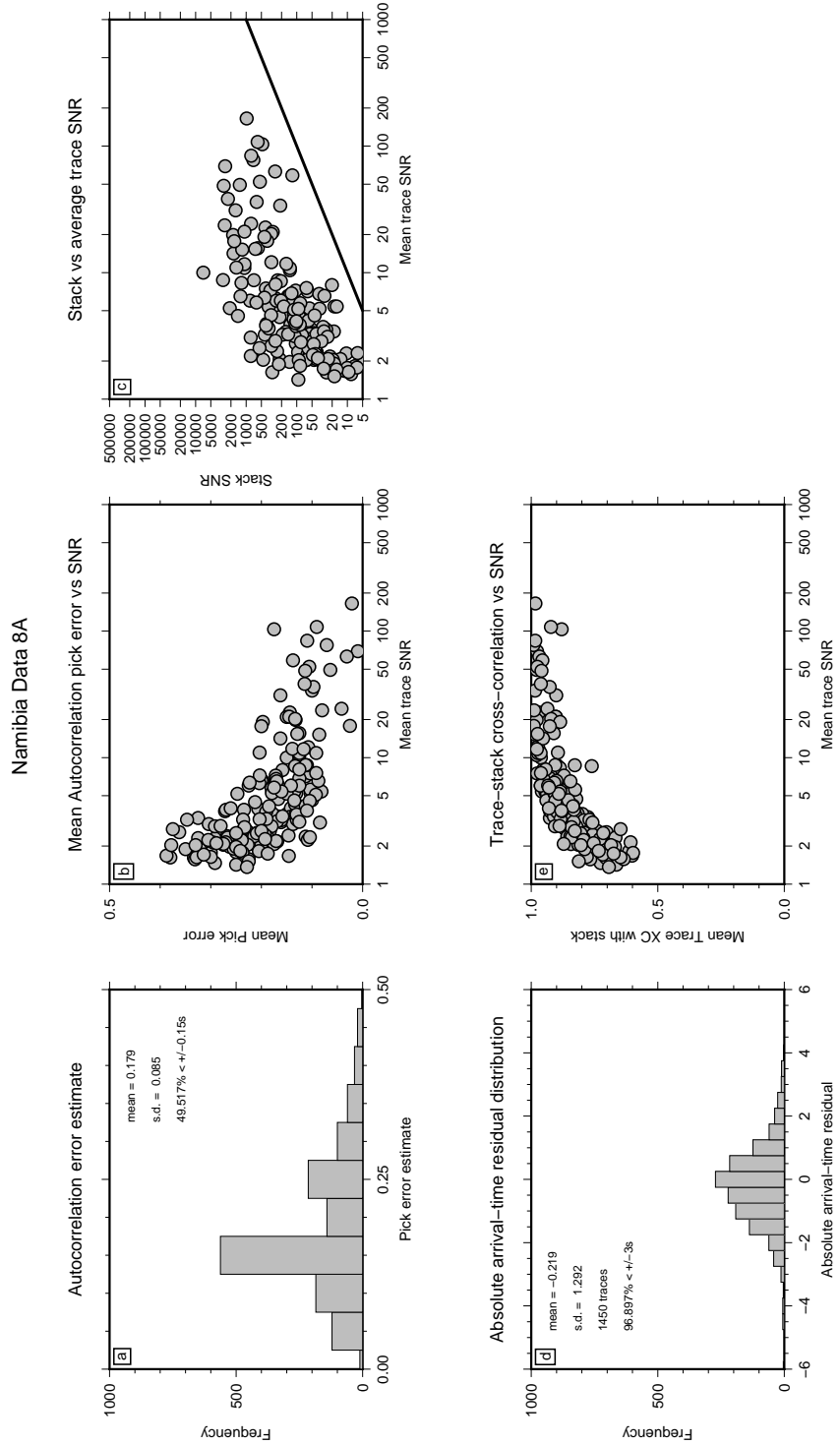


Figure S12. For the Namibian data set (Durrheim & Nyblade, 2009; Nyblade, 2015): (a) Autocorrelation pick error estimates for each arrival-time. (b) For each earthquake, mean autocorrelation pick error plotted against mean trace SNR. (c) For each earthquake, stacked trace SNR against mean trace SNR. $y=x$ (black line). (d) Absolute arrival-time residual distribution. (e) For each earthquake, mean trace–stack cross-correlation coefficient against mean trace SNR.

Crustal Corrections

Topographic and Ellipticity corrections

To recover mantle wavespeeds, we must first correct the measured data for perturbations away from the spherical Earth, not associated with mantle structure. Variations in crustal thickness have a strong influence on teleseismic arrival-times which can be mapped into apparent Earth structure, if not adequately corrected for. Travel-time corrections for station elevation and Earth's ellipticity should also be implemented and are particularly important in regions with significant topographic variation and when imaging over broad scales. We compute travel-time corrections for topography at a given station and account for ray incidence angle. For the African data set, the maximum topographic correction is 0.826 s for a station located just west of Lake Malawi in the data set of Boyce et al. (2021). Travel-time corrections due to Earth's ellipticity are computed using the formulation of Kennett and Gudmundsson (1996). The maximum ellipticity correction for the direct P-wave African data set is 0.965 s but this value can be up to 1.3 s for deeper-diving core phases.

We take the opportunity to highlight the wavespeed differences caused by the sign error in the implementation of the topographic and ellipticity corrections applied to the absolute arrival-time data prior to inversion in our previous model AFRP20 (Boyce et al., 2021). The impact is largest at equatorial latitudes and in regions of high elevation such as the East African Plateau. Consequently the 'true' wavespeeds are often faster than in the previously published work (Boyce et al., 2021). Using identical data to Boyce et al. (2021), the average wavespeed anomaly within AFRP20 of $\delta\bar{V}_P = -0.216\%$ with respect to ak135, increases to a faster average of $\delta\bar{V}_P = -0.129\%$ (also see Figure S13), however the main conclusions of the paper are retained.

Boyce et al. (2021) argue that two disparately sourced whole-mantle plumes underlie East Africa and the depth-limited extent of fast P-wavespeeds below the Tanzanian craton presents evidence for metasomatic modification during the Pan-African Orogeny. These tomographically imaged features are less slow in the corrected model (Figure S13) and the new model presented in the current manuscript, but resolution remains sufficient, so observations of distinct plumes and decrease in wavespeed in the lower portion of the Tanzanian craton are more subtle than previously stated but are still well sampled.

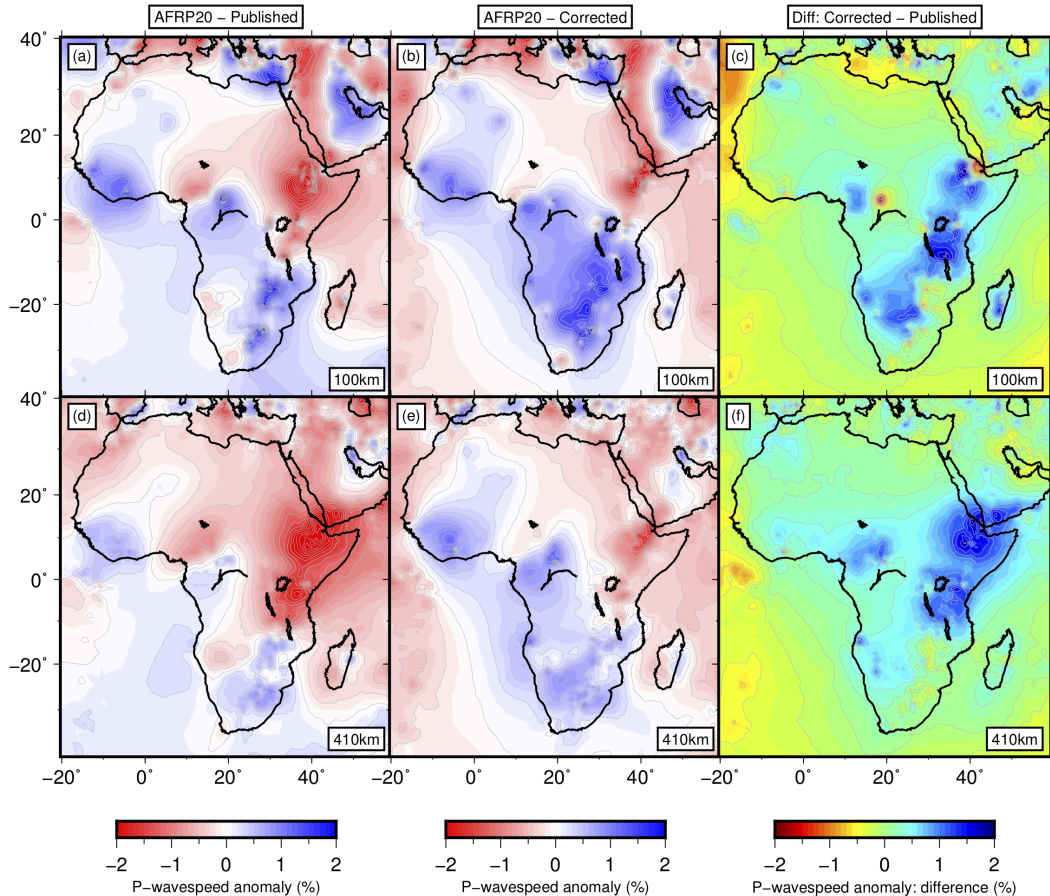


Figure S13. At 100 km and 410 km depth, P-wavespeed anomaly (percentage w.r.t. ak135) for AFRP20-published (Boyce et al., 2021, *a,d*) and AFRP20-corrected (*b,e*) and the difference between them (*c,f*). A positive (blue) difference (*c,f*) indicates the corrected model is faster (less slow) than the published model. Tomographic models constructed using identical data distribution to the published manuscript (Boyce et al., 2021).

Crustal thickness corrections

Next, crustal Moho depths are used to correct the absolute arrival-time residuals prior to inversion in order to only invert for mantle wavespeed structure. We supplement the Moho depth compilation used by Boyce et al. (2021) with Moho depth estimates from Heit et al. (2015), seismic refraction lines in the Turkana Depression (Braile et al., 1994; Mechie et al., 1994; Prodehl et al., 1994). Additional seismograph stations in southern Ethiopia, Kenya and Uganda have been analyzed using the modified H-K stacking receiver function technique (Ogden et al., 2023). These Moho depth estimates are smoothed into Crust1.0 (Laske et al., 2013) and imposed onto the adaptively parameterized grid within the inversion. We propagate rays through this crustal model, and resulting arrival-time residuals are removed from the data prior to inversion. For more discussion, see Boyce et al. (2021).

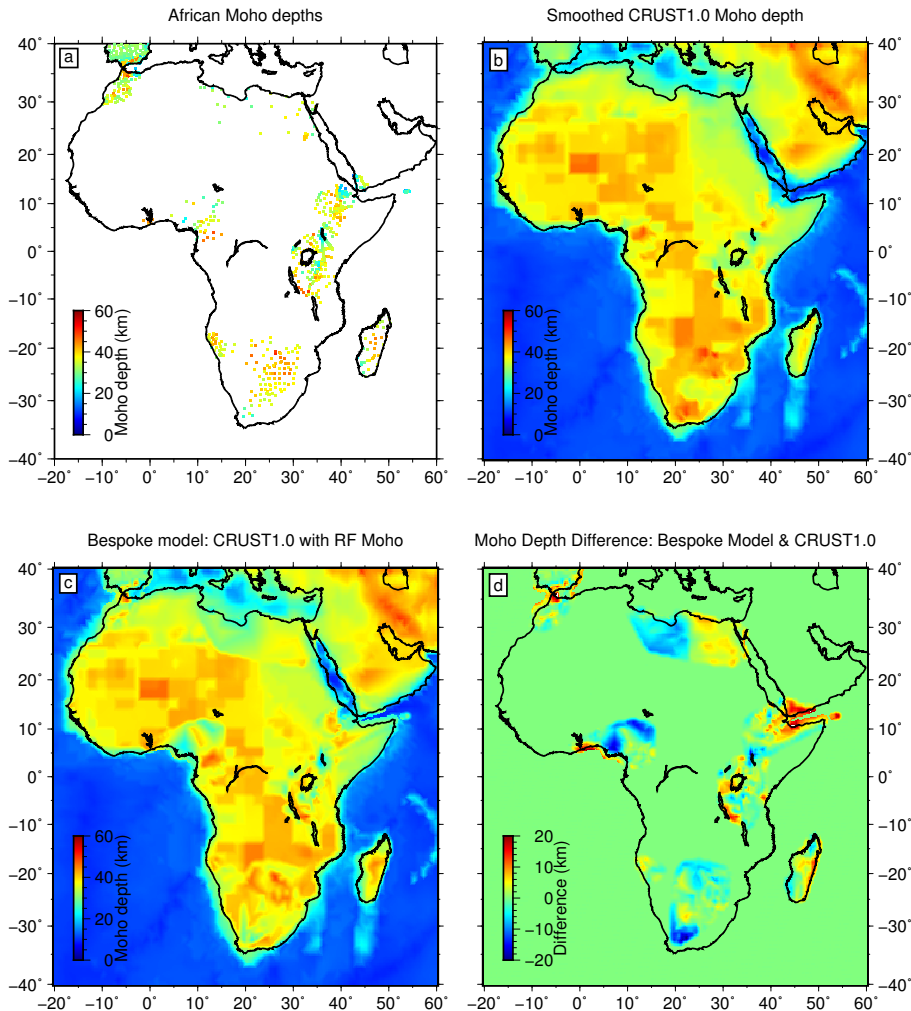


Figure S14. (a) We use Moho depth estimates from Turkana, Uganda and southern Africa (Heit et al., 2015; Braile et al., 1994; Mechie et al., 1994; Prodehl et al., 1994; Ogden et al., 2023) to supplement the compilation of Boyce et al. (2021). These data are smoothed into CRUST1.0 (b: Laske et al., 2013) to produce a bespoke crustal thickness map (c). The difference between the bespoke Moho depth map and CRUST1.0 is shown in (d). Positive values are found where CRUST1.0 is thinner than the bespoke Moho depth compilation.

Adaptive Parameterization

Figure S15 shows the adaptively parameterized grid cells within the inversion at four depths (*a–d*: 100–660 km).

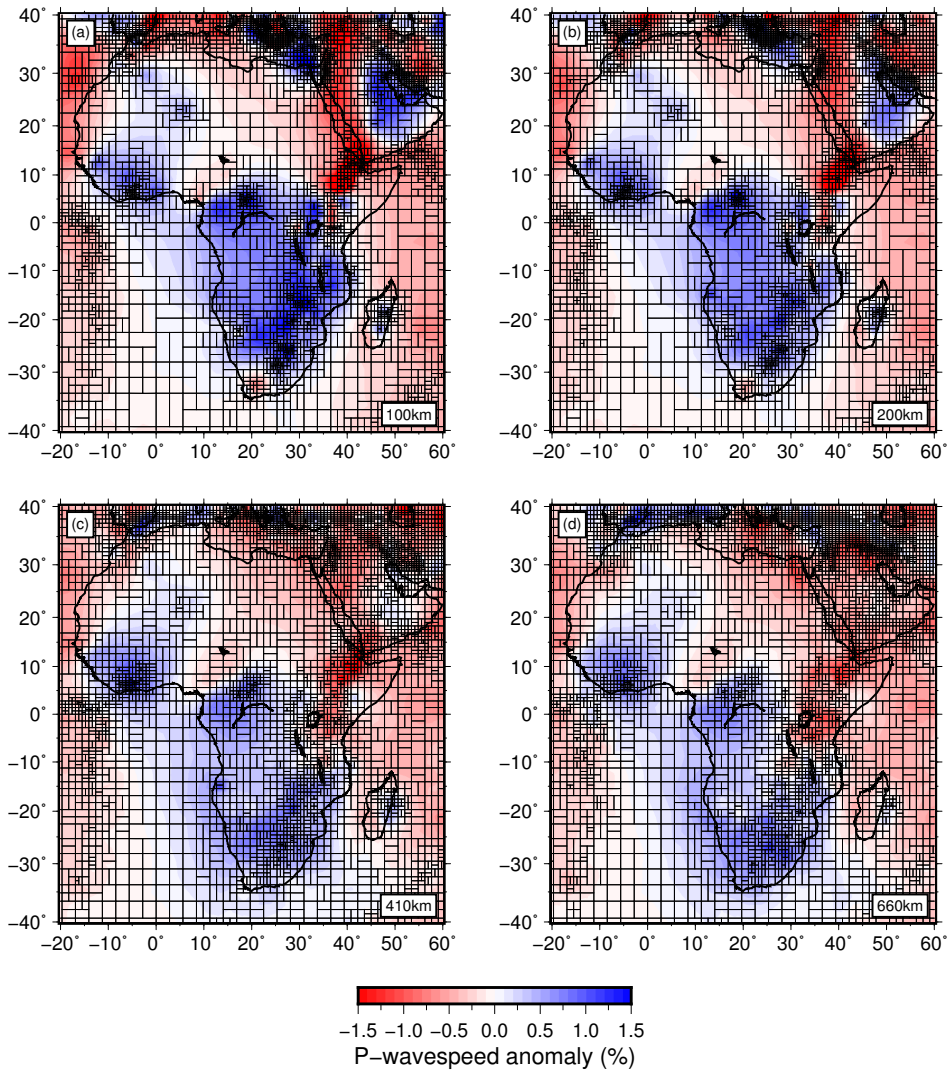


Figure S15. Fine black cell outlines indicate the adaptive parameterization within the AFRP22 tomographic model at four depths (*a–d*: 100–660 km). Wavespeed anomalies are plotted as percentage deviation from ak135 ($\delta V_P = \pm 1.5\%$).

Trade-off Curve Approach

We use a trade-off curve to determine the vertical- and horizontal-gradient regularization parameters within the AFRP22 inversion (Figure S16). The model damping parameter (N) has very little impact on the resulting model around the knee of the trade-off curve. The preferred model “E” lies near the knee of the curve, has regularization values of $H = 2000$, $R = 500$ and $N = 50$, and best balances results for the African part of the global model space. Trade-off parameters are shown in Table S1.

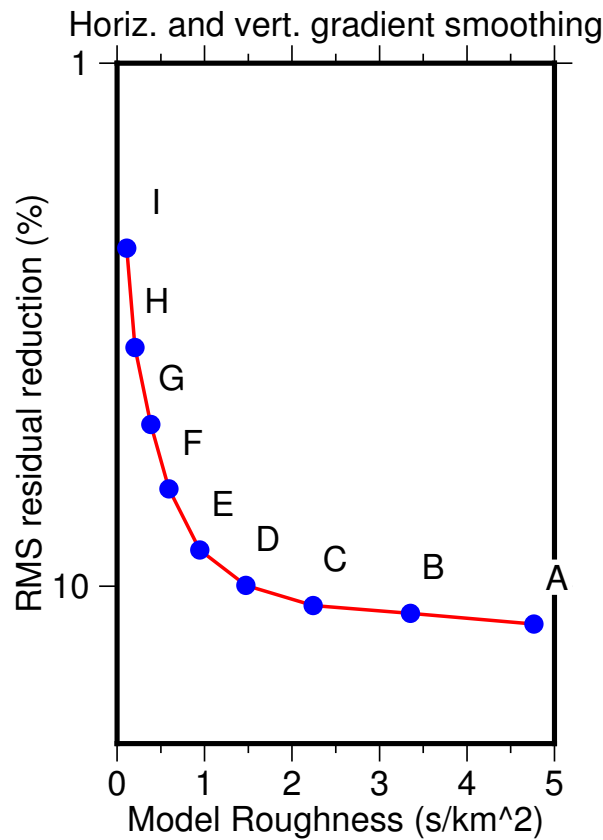


Figure S16. Trade-off curve approach used to determine horizontal and vertical gradient smoothing parameters used in the inversion for AFRP22. Root-mean-squared residual reduction (%) is plotted against model roughness (s/km^2). We choose model “E”. Absolute values can be found in Table S1.

| Horizontal and Vertical Gradient Smoothing | | | | |
|--|-------|------|-----------|---------------|
| Label | H | R | Roughness | RMS res. Red. |
| A | 125 | 31 | 4.76576 | 11.8179 |
| B | 250 | 62 | 3.35298 | 11.2718 |
| C | 500 | 125 | 2.24170 | 10.8886 |
| D | 1000 | 250 | 1.47117 | 9.96815 |
| E | 2000 | 500 | 0.94659 | 8.53128 |
| F | 4000 | 1000 | 0.59285 | 6.51816 |
| G | 8000 | 2000 | 0.38638 | 4.90659 |
| H | 16000 | 4000 | 0.20455 | 3.49572 |
| I | 32000 | 8000 | 0.10987 | 2.25824 |

Table S1. Parameters from combined horizontal (H) and vertical (R) gradient smoothing trade-off analysis corresponding to Figure S16.

Regional Scale Resolution Tests

We follow the resolution tests outlined by Boyce et al. (2021) to further test the sensitivity of AFRP22 to distinct slow wavespeed anomalies at the regional scale (Figures S17–S20).

Slow wavespeed anomalies positioned below the Ethiopian and East African plateaus, and separating Turkana Depression (Figures S17–S19) are well constrained laterally and are recovered with amplitudes of >80%, particularly with the addition of stations in Turkana compared to (Boyce et al., 2021). Lateral smearing between slow wavespeed anomalies is largely restricted to below transition zone depths, while some vertical smearing does occur below the upper mantle. A single slow wavespeed anomaly below the Turkana depression is recovered with peak amplitudes of >90% (Figure S19), a marked improvement compared to (Boyce et al., 2021). Some minor lateral smearing around lower transition zone depths is apparent towards the northeast. A slow wavespeed anomaly below the Turkana depression extending to the core-mantle boundary, should be resolvable in AFRP22 (Figure S20) but with depressed amplitudes, especially below 1500 km depth (as low as \sim 25% of input anomaly). Narrow (\sim 2–3° width) slow wavespeed anomalies in the upper mantle are somewhat resolvable below dense station coverage (Figure S21).

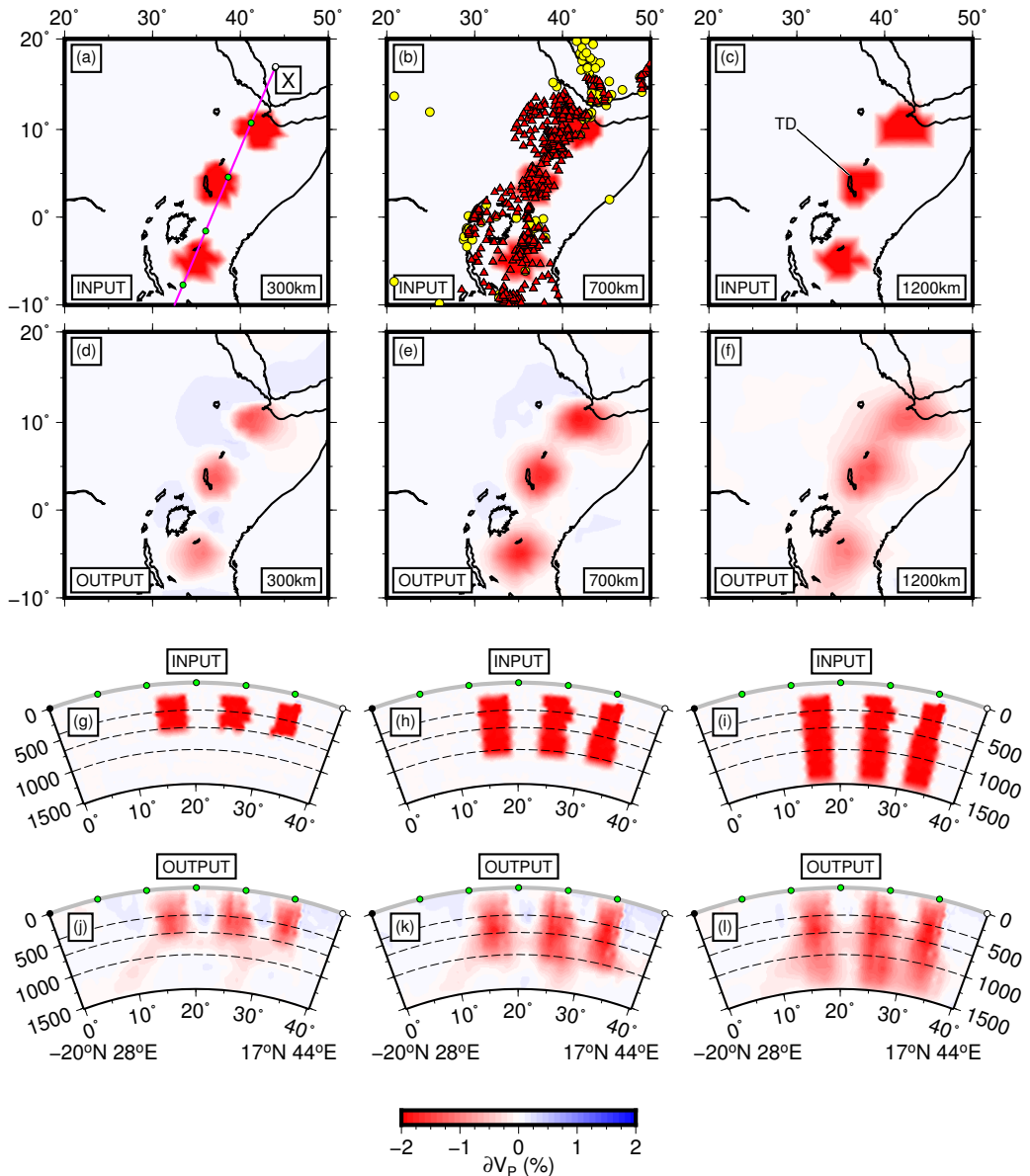


Figure S17. Structural resolution test of three isolated slow wavespeed anomalies ($\delta V_P = -2.0\%$, $\sim 4.5^\circ$ width) with depth extents varying between 660 km (a,g), 1000 km (b,h), 1500 km (c,i). Output models shown in map (d–f) and cross section ‘X’ (j–l) are shown on the same color scale. Cross-section location (‘X’) is shown in (a). Locations of “EHB” stations and temporary deployments are shown as yellow circles and red triangles respectively (b). Visual defects within input models arise from coarse adaptive parameterization due to poor ray path sampling. TD: Location of Turkana Depression.

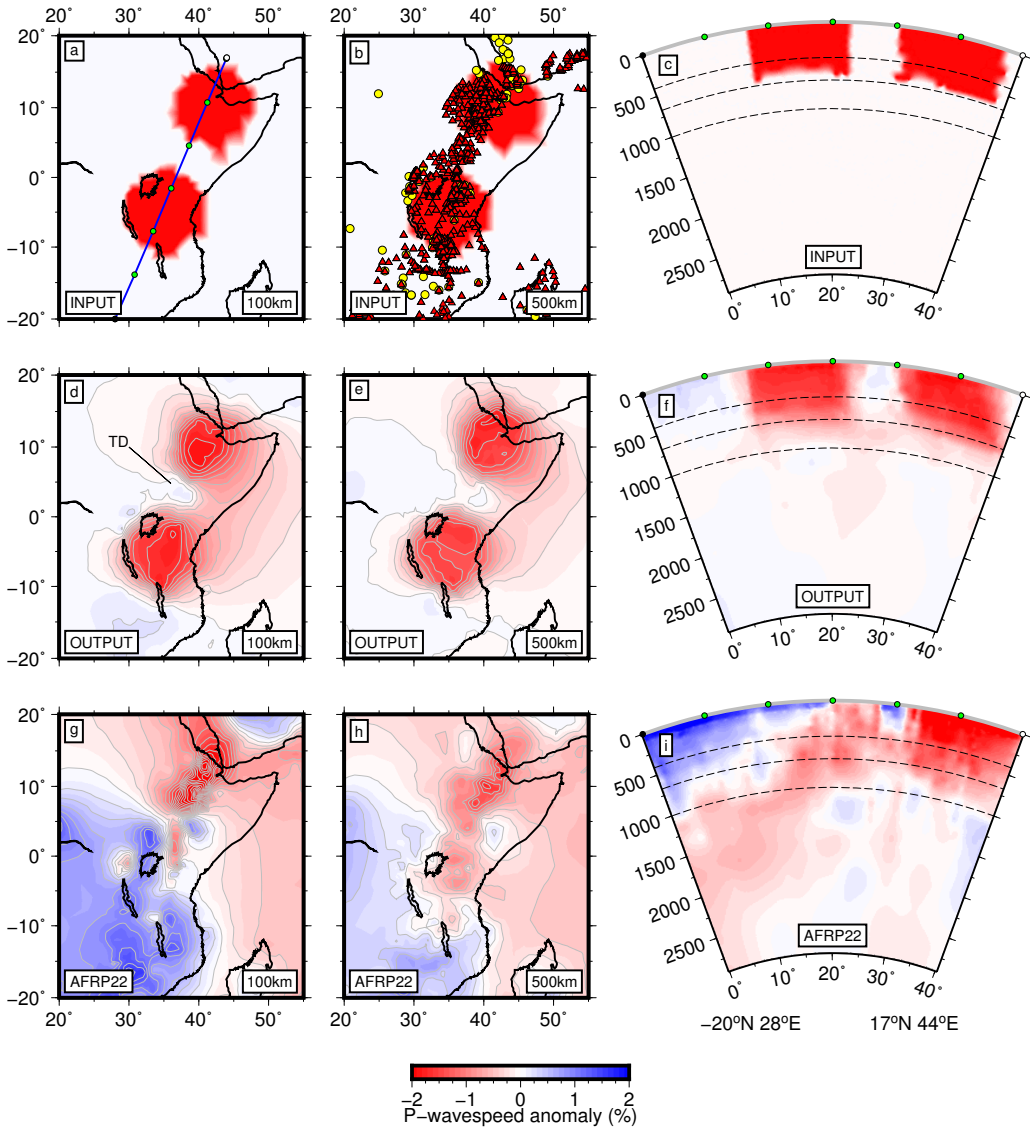


Figure S18. Resolution test for two slow wavespeed anomalies ($\delta V_P = -2.0\%$, $\sim 11^\circ$ width) extending from the surface to 660 km depth below the Ethiopian and East African plateaus after Boyce et al. (2021). Input anomalies (a–c) are shown on an identical color scale to the recovered anomalies (d–f) and AFRP22 (g–i). The cross-section location used is indicated in (a), station distribution (AARM derived stations: red triangles, “EHB” stations: yellow circles) is indicated in (b). TD: Location of Turkana Depression.

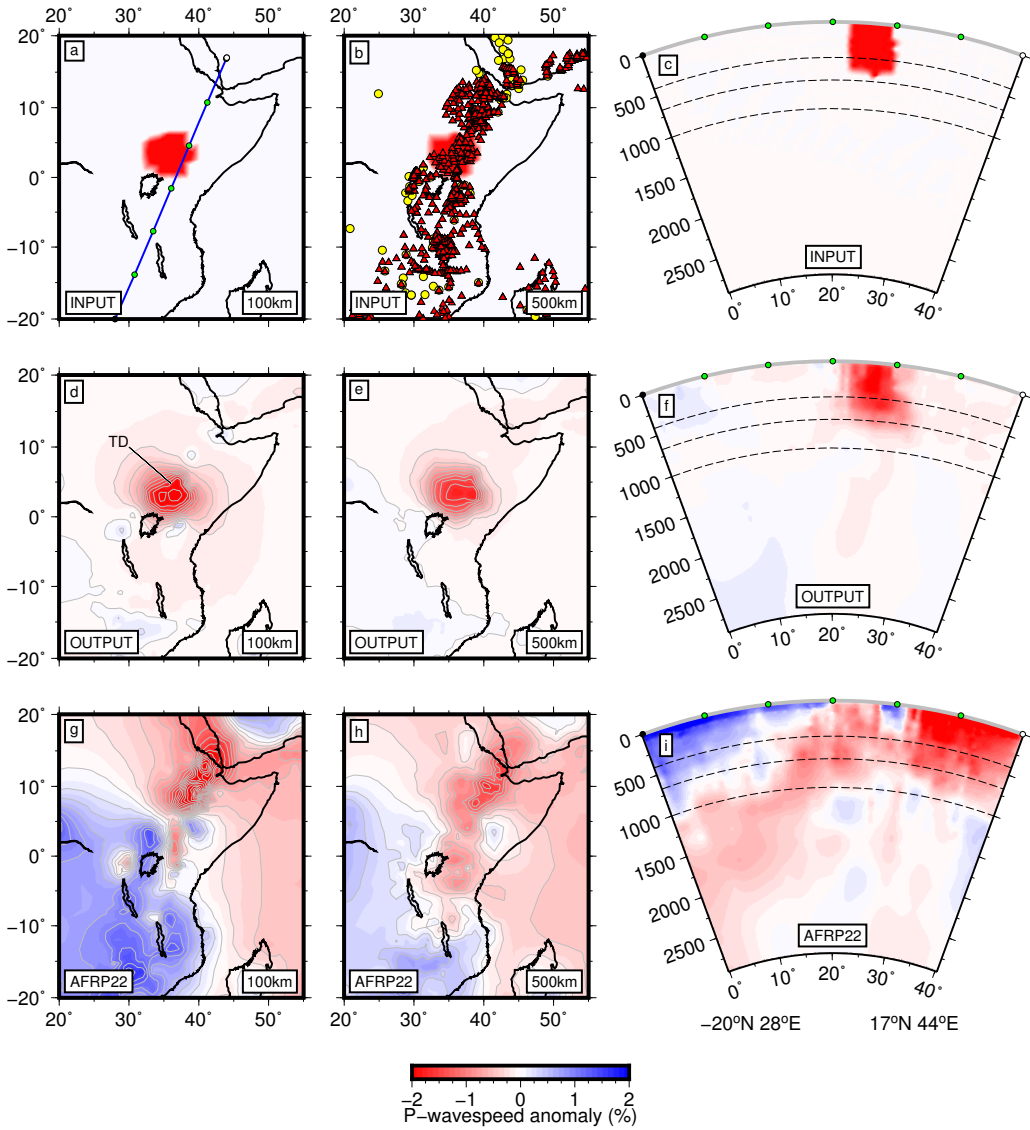


Figure S19. Resolution test for an upper mantle slow wavespeed anomaly ($\delta V_P = -2.0\%$, $\sim 7^\circ$ width) extending from the surface to 660 km depth below the Turkana Depression after Boyce et al. (2021). The input anomaly (a–c) is shown on an identical color scale to the recovered anomaly (d–f) and AFRP22 (g–i). The cross-section location used is indicated in (a), station distribution (AARM derived stations: red triangles, “EHB” stations: yellow circles) is indicated in (b). TD: Location of Turkana Depression.

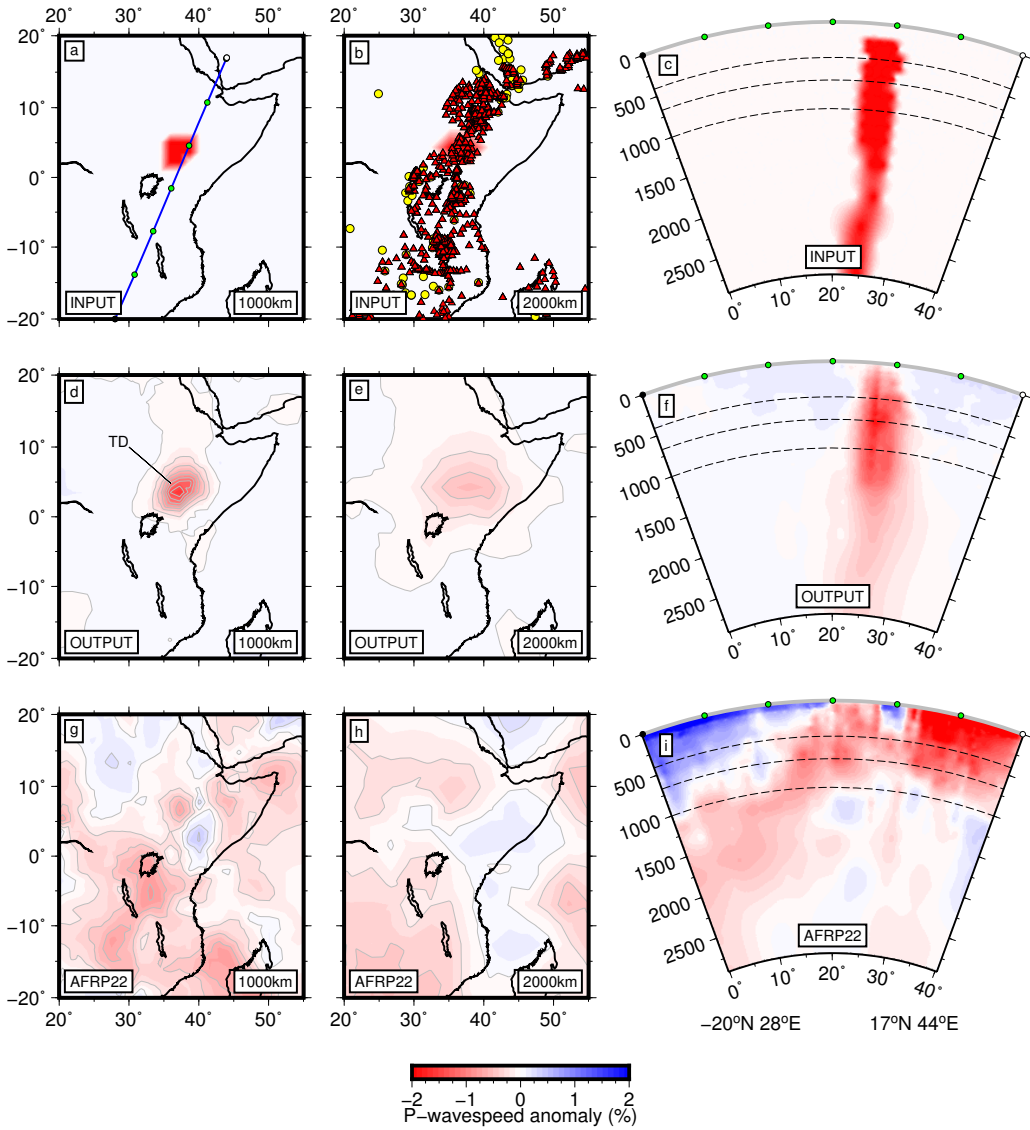


Figure S20. Resolution test for a whole mantle slow wavespeed anomaly ($\delta V_P = -2.0\%$, $\sim 7^\circ$ width) extending from the surface to the core-mantle boundary below the Turkana Depression. The input (a–c), output (d–f) and AFRP22 (g–i) are shown on an identical color scale. The cross-section location used is indicated in (a), station distribution (AARM derived stations: red triangles, “EHB” stations: yellow circles) is indicated in (b). TD: Location of Turkana Depression.

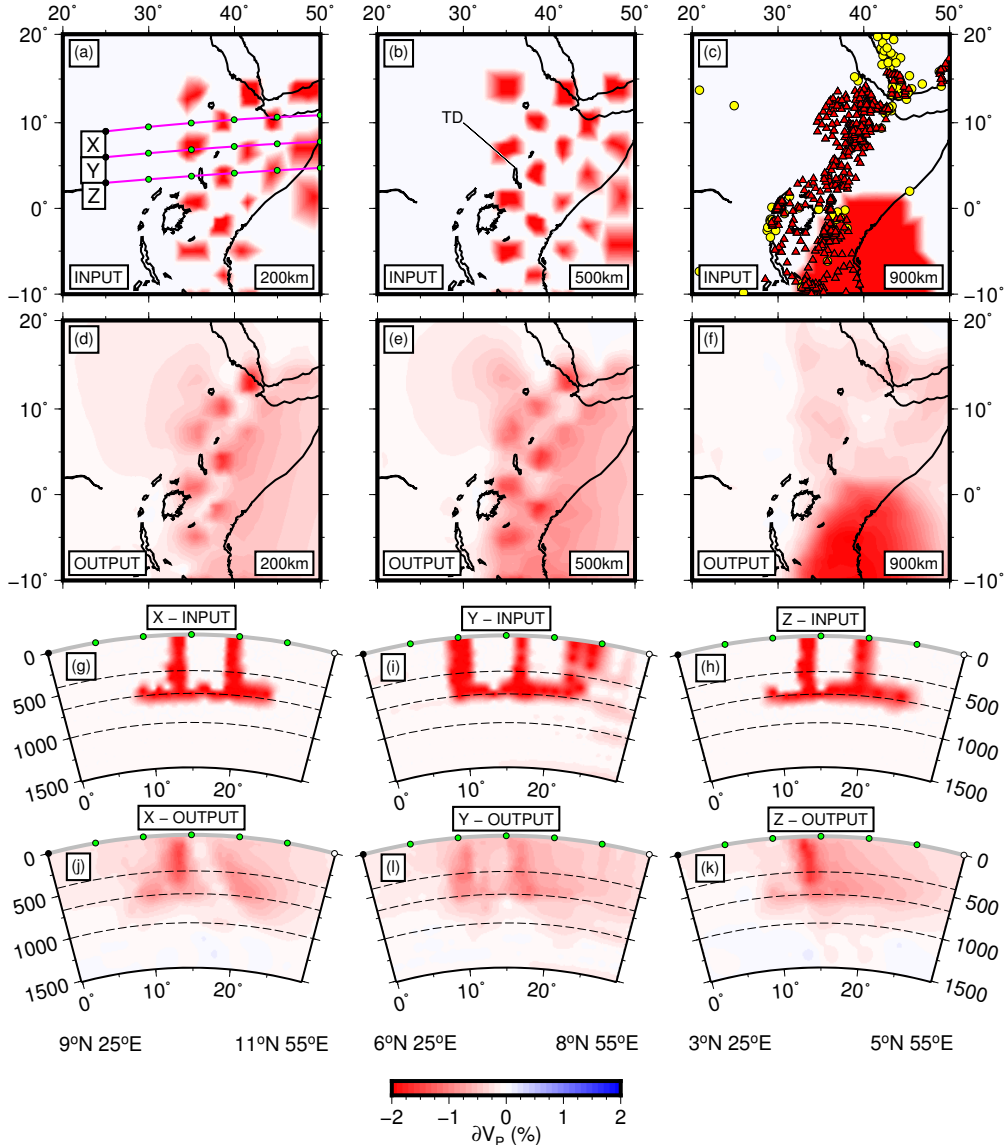


Figure S21. Resolution test for small scale slow wavespeed vertical anomalies ($\delta V_P = -2.0\%$, $\sim 2-3^\circ$ width) extending from the surface to a flattened anomaly at the base of the mantle transition zone. Below a broad slow wavespeed anomaly extends to the core-mantle boundary. The input (a–c, g–h) and output (d–f, j–k) are shown on an identical color scale. Cross-section locations are indicated in (a), TD: Location of Turkana Depression indicated in (b), station distribution (AARM derived stations: red triangles, “EHB” stations: yellow circles) is indicated in (c).

Broad Scale Resolution Tests

We use the ‘two-plume and craton’ synthetic model described by Boyce et al. (2021, Figure 3) to test the broad scale tomographic resolving power of AFRP22 and facilitate comparison to previous work. This model includes two elliptical slow wavespeed anomalies extending from the surface in East Africa to the core-mantle boundary and approximate positions of upper mantle wavespeed anomalies ($\delta V_P = \pm 2.0\%$ – Figure S22). The presence of ponded slow wavespeeds at the base of the East African mantle transition zone and vertical gaps within whole-mantle anomalies are also tested in (Figure S23, S24, S25) following Boyce et al. (2021, Figure S25).

In the upper mantle, similarly to AFRP20 (Boyce et al., 2021), the west African and Congo cratons are poorly resolved here due to the lack of overlying station (Figure S22). Although the southern African cratons exhibit significant vertical smearing, they are recovered with up to $\sim 75\%$ input amplitude. The Tanzanian craton exhibits reasonable lateral recovery but amplitudes are significantly muted at $< 25\%$ of input amplitude at 100 km depth (Figure S22). Muted amplitudes may be influenced by the adjacent slow wavespeed anomaly that exhibits improved amplitude recovery ($> 60\%$) throughout northern Kenya and Ethiopia, compared to Boyce et al. (2021) but this anomaly is poorly resolved laterally beyond station coverage. Broad slow wavespeeds extending to the lower mantle are well recovered with marginally less lateral smearing of anomalies at mid-to-lower mantle depths than in AFRP20 (Boyce et al., 2021). Recovery amplitudes of slow wavespeed anomalies in the upper mantle below the Turkana Depression is $> 75\%$.

Similarly to AFRP20 (Boyce et al., 2021), the ponded plume synthetic test indicates that we expect to identify ponded slow wavespeed material at the base of the MTZ with thickness greater than our vertical parameterization (i.e. > 50 km; Figure S23). A vertical gap of ≥ 300 km (Figure S24) in whole-mantle slow wavespeed anomalies can be visually distinguished by a marked amplitude reduction in recovered images. However some vertical smearing across the gap can take place at up to 700 km length-scales and up to $\sim 30\%$ of input overlying anomaly amplitude. Vertical smearing across a 500 km gap is most significant between ~ 660 – 1000 km depths (Figure S25). Therefore, a significant wavespeed reduction (by $\sim 1/3$ compared to shallower recovered amplitudes) in this depth range, renders a connection between upper and lower mantle anomalies more un-

certain than a gap that occurs at shallower or greater depths. Within these gap tests, recovery amplitudes are often >90% above the gap but are reduced below.

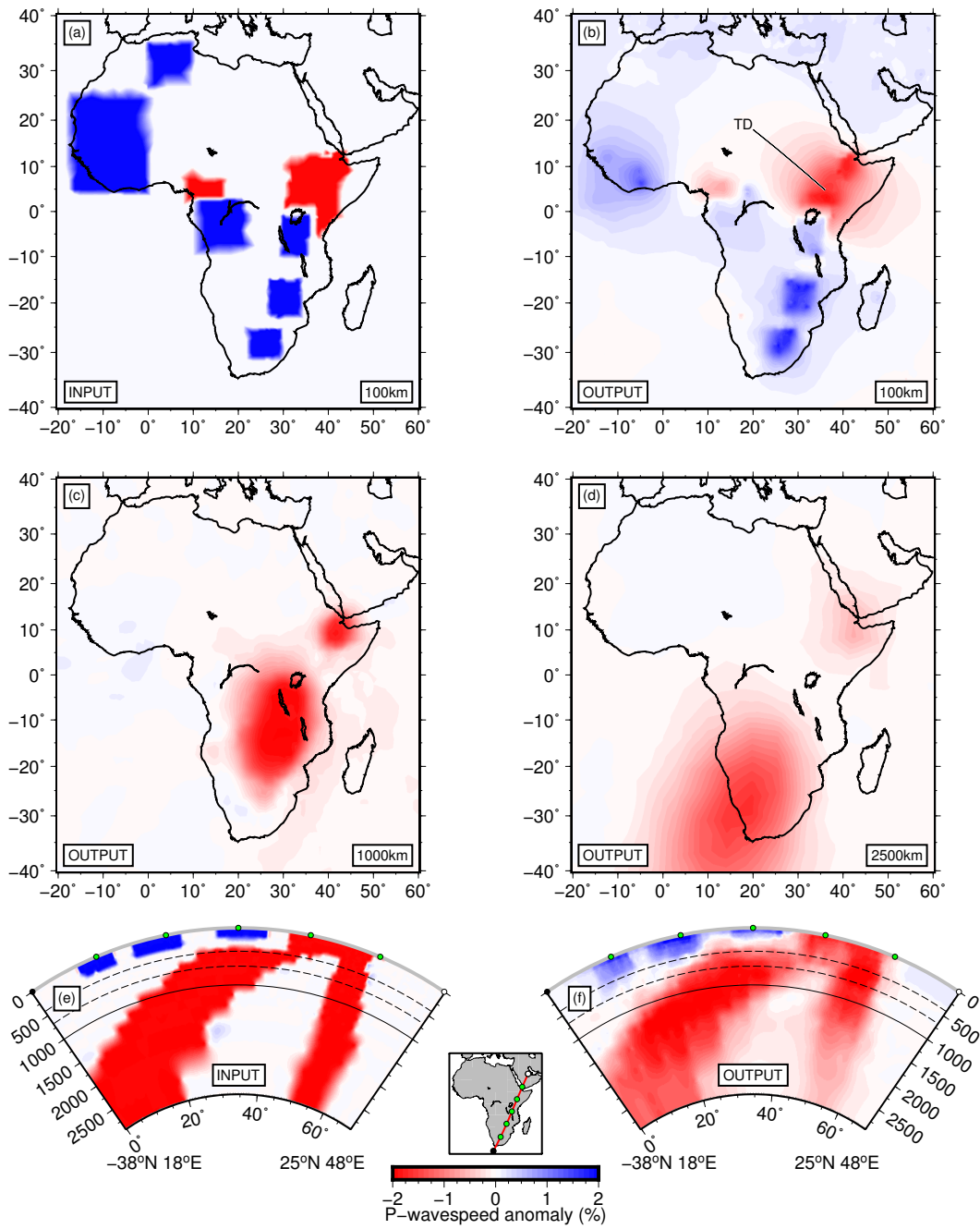


Figure S22. Resolution test for broad-scale wavespeed anomalies below Africa. Input anomalies amplitudes are $\delta V_P = \pm 2.0\%$ (a,e). The broad slow wavespeed, extending to the lower mantle below southern Africa, increases from $\sim 14^\circ$ to $\sim 28^\circ$ width over the mantle depth range. The vertical slow wavespeed anomaly extending below Ethiopia, increases from $\sim 5^\circ$ to $\sim 10^\circ$ width over the mantle depth range. Visual defects occur in coarsely sampled regions - Figure S15. Recovered anomalies (b-d,f) are shown using the same color scale. The inset map between e and f indicates the cross-section location. TD: Location of Turkana Depression.

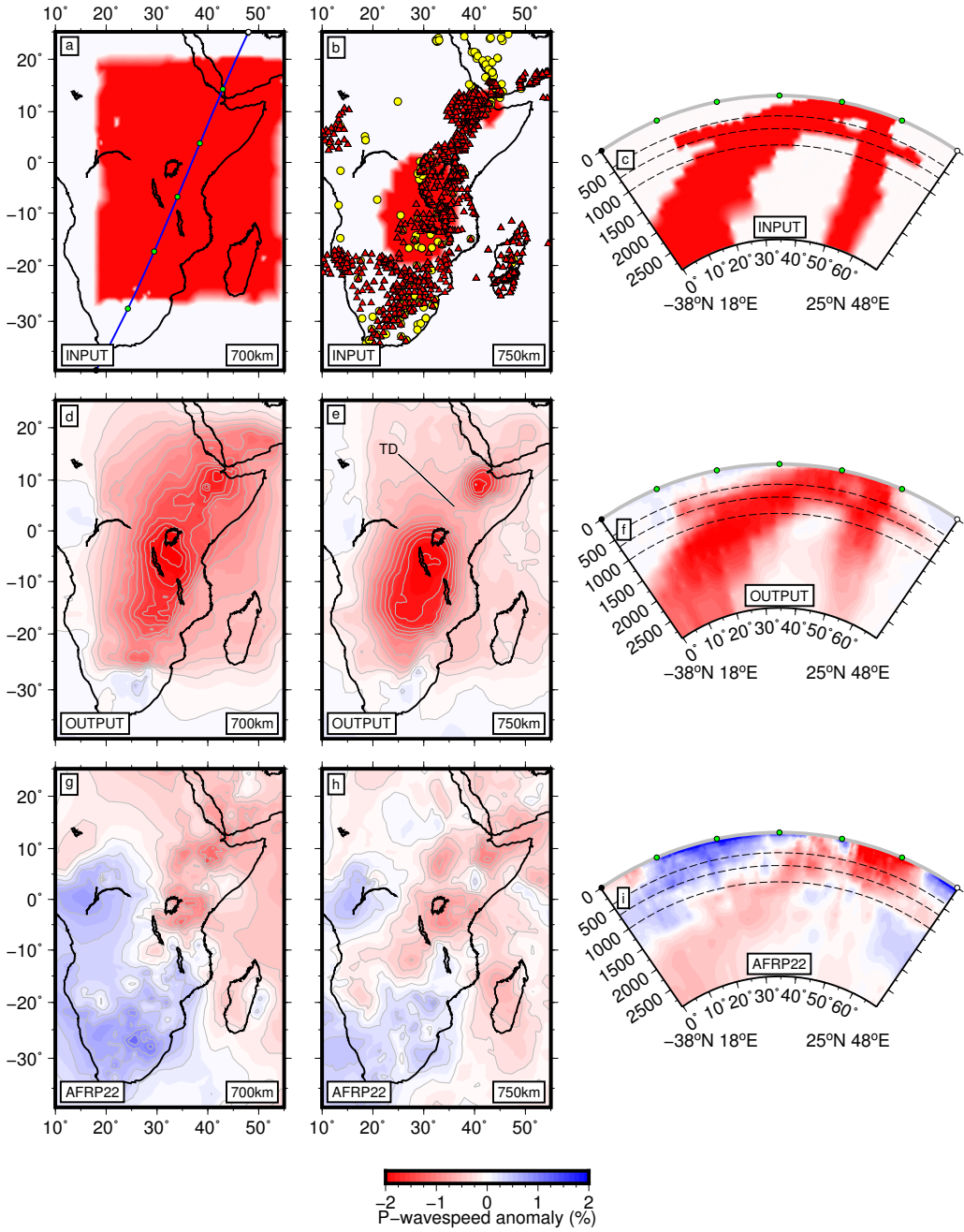


Figure S23. Resolution test for sensitivity of AFRP22 to ponded slow wavespeeds at the base of the mantle transition zone using the identical input to Boyce et al. (2021, Figure S25). The two slow wavespeed anomalies ($\delta V_P = -2.0\%$) extending to the core mantle boundary are modified to include a pervasive slow wavespeed feature throughout East Africa at lower transition zone depths (500–700 km depth). Initial slow wavespeed anomaly sizes, for those extending into the lower mantle, are identical to Figure S22. Visual defects occur in coarsely sampled regions – Figure S15. (a–c) show input anomalies, cross-section location and station distribution (AARM derived stations: red triangles, “EHB” stations: yellow circles). Recovered anomalies (d–f) and AFRP22 (g–i) are plotted on the same color scale as the input. TD: Location of Turkana Depression.

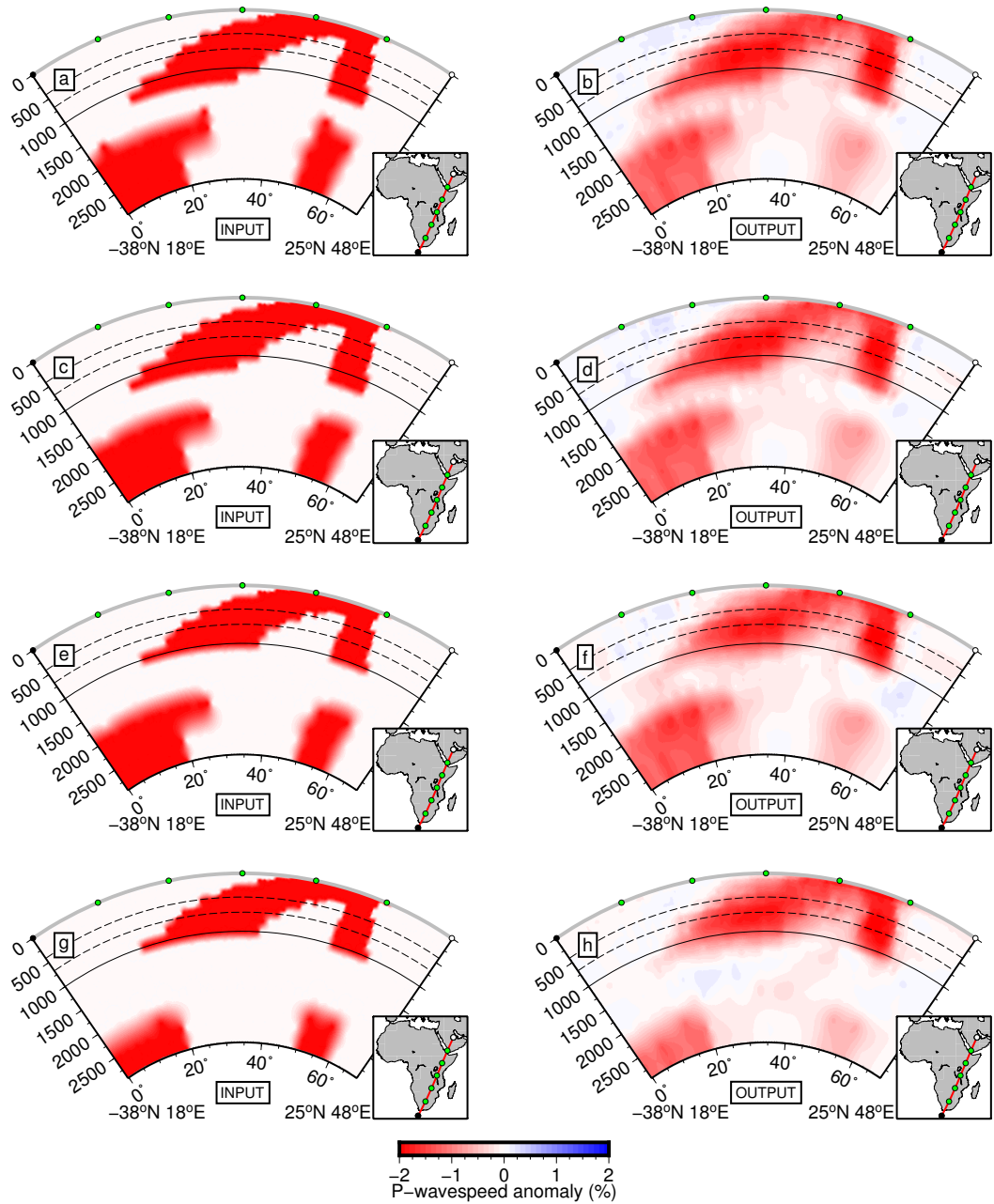


Figure S24. Plume gap width test. Input models comprise two slow wavespeed anomalies ($\delta V_P = -2.0\%$) extending from the surface to the core-mantle boundary below Africa. Initial anomalies mirror those within previous tests (e.g., Figure S22). We modify this structure by creating a gap ($\delta V_P = 0.0\%$) in each anomaly of increasing thickness from top-to-bottom (Thicknesses: 300 km, 500 km, 700 km, 1000 km). Input (a,c,e,g) and output anomalies (b,d,f,h) are displayed on the same color scale.

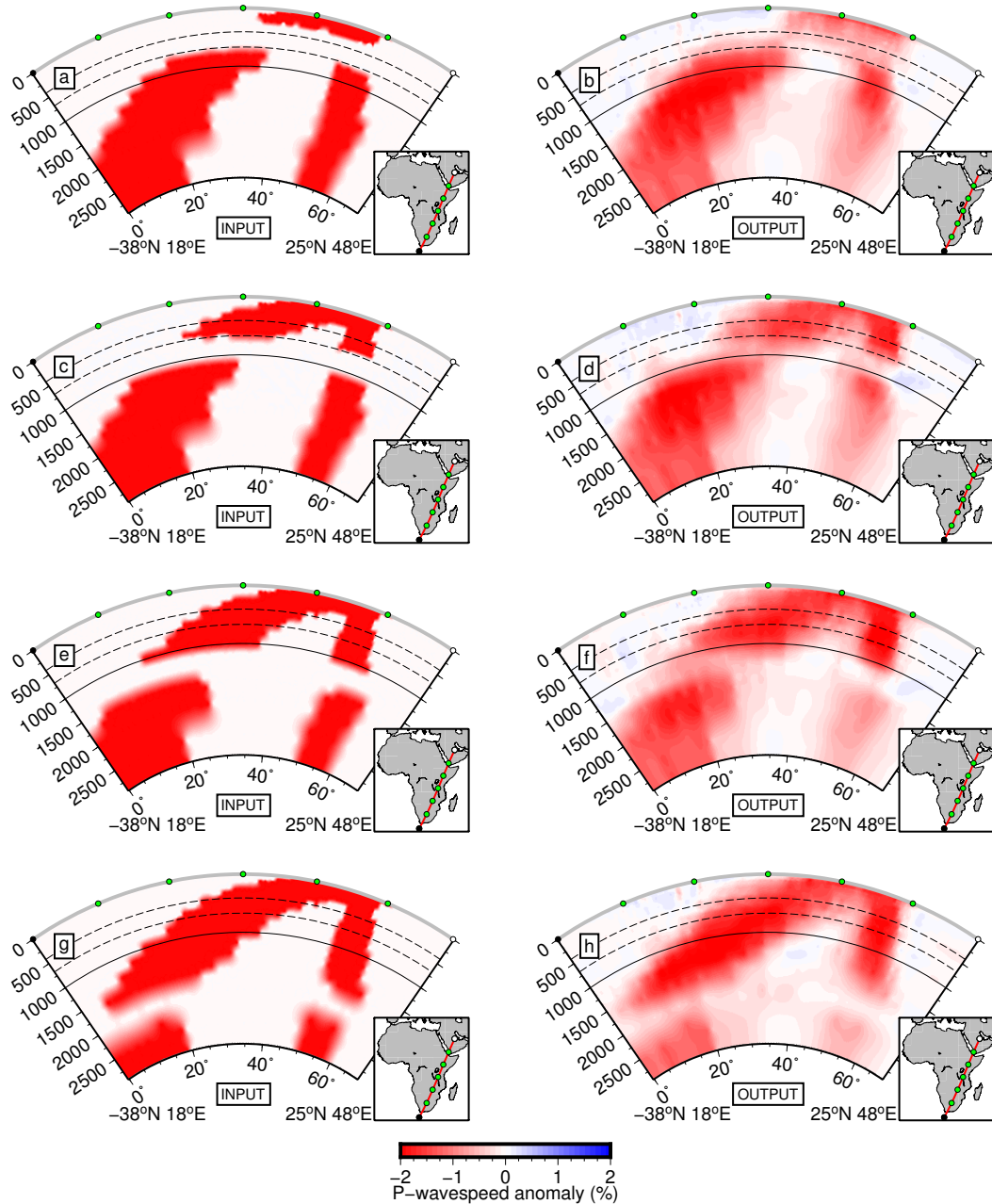


Figure S25. Plume gap location test. Input models comprise two slow wavespeed anomalies ($\delta V_P = -2.0\%$) extending from the surface to the core-mantle boundary below Africa. Initial anomalies mirror those within previous tests (e.g., Figure S22). We modify this structure by creating a gap of 500 km thickness ($\delta V_P = 0.0\%$) in each anomaly, centered at 500 km, 900 km, 1300 km, 1900 km depths (figure top-to-bottom). Input (a,c,e,g) and output anomalies (b,d,f,h) are displayed on the same color scale.

Checkerboard Resolution Tests

We arrange 300 km thick $\delta V_P = \pm 2\%$ wavespeed anomalies throughout the model space at 200 km, 600 km and 900 km depth to form checkerboard input models. We vary the lateral anomaly length scales from 2–10° (Figures S26–S30) across five resolution tests. We also test the recovery of 10° checkerboard anomalies extending into the lower mantle (Figure S31). We focus our attention on East Africa, but show resolution results for the whole of Africa for ease of comparison with Boyce et al. (2021).

2° anomalies are adequately recovered spatially at 200 km depth with ~50% amplitudes in parts of East Africa with dense station coverage (Figure S26). Below 200 km depth, recovery of these small anomalies is weak. 3° anomalies are well recovered spatially throughout the densely sampled regions of eastern and southeastern Africa (at ~50–75% amplitude), particularly at 200 km depth (Figure S27), except below the central Tanzanian craton. Below, at 600 km depth, spatial recovery is less robust with amplitudes of ~50%. New seismic data from Turkana and Uganda contribute significantly to greatly improved resolving power in the region at 200–600 km depth compared to Boyce et al. (2021).

5° anomalies are spatially well recovered often with $\geq 50\%$ amplitude recovery at 200–900 km depth. At the shallowest depths, resolution is again limited to regions of dense station coverage (Figure S28). Despite some vertical smearing these are the smallest anomalies that exhibit some resolvability in depth. Boundaries of 7.5° and 10° anomalies are well recovered at 200 km and 600 km in East Africa (Figures S29–S30) with significant improvement compared to Boyce et al. (2021). 7.5° and 10° anomalies are recovered at ~50% amplitude throughout southern and eastern Africa at 900 km depth and are resolvable in depth despite some vertical smearing on the order of ~100–200 km. Figure S31 shows large 10° anomalies are well resolved into the deep mantle (>2000 km depth) with ~50% amplitude.

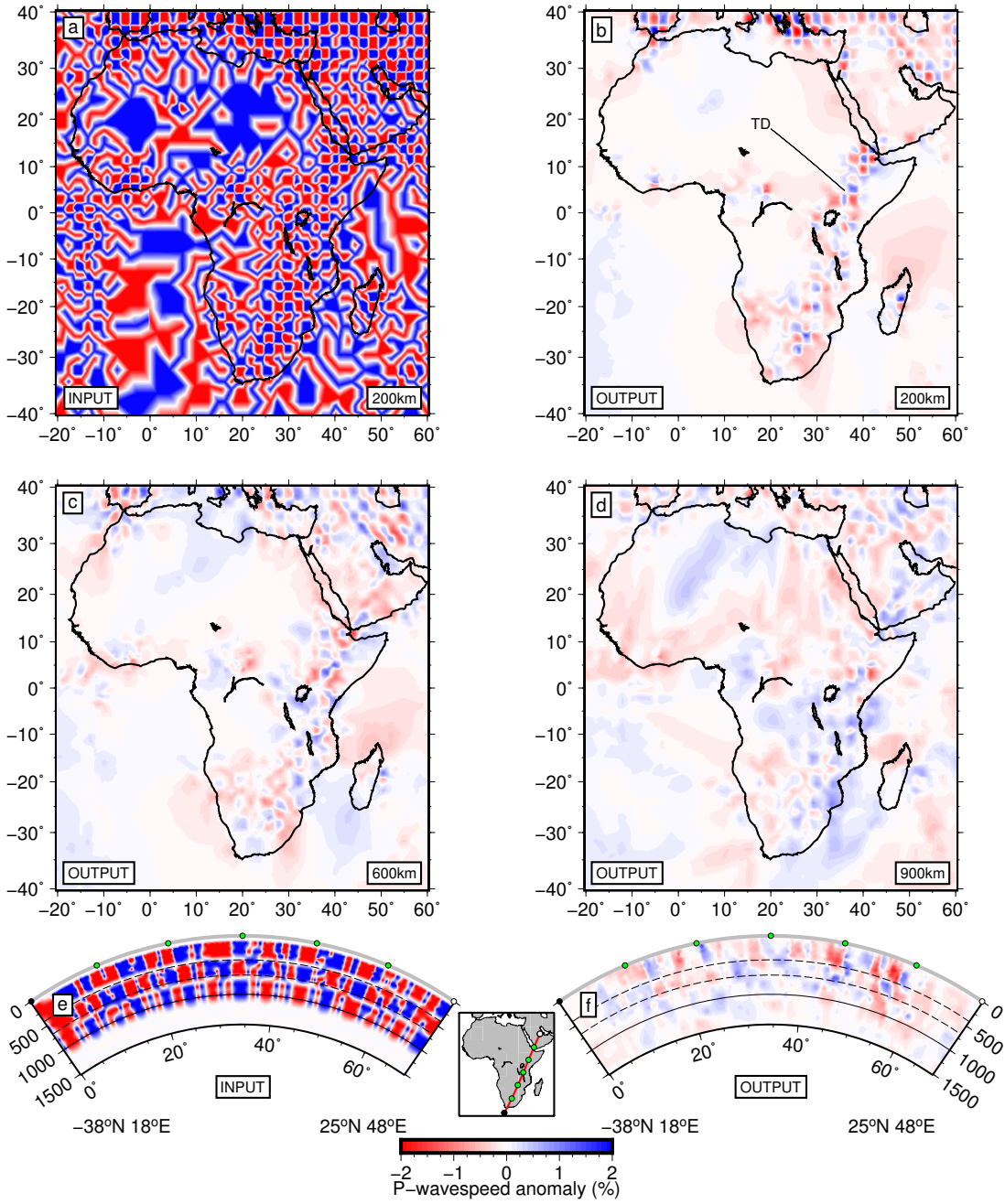


Figure S26. Checkerboard resolution test constructed with 2° width wavespeed anomalies of $\delta V_P = \pm 2.0\%$ input amplitude (*a,e*). Input anomalies are arranged in an alternating pattern at 200 km, 600 km and 900 km depth but exhibit defects that result from a coarsely parameterized grid in weakly sampled regions (Figure S15). (*b-d,f*) show recovered anomalies on the same color scale as the input.

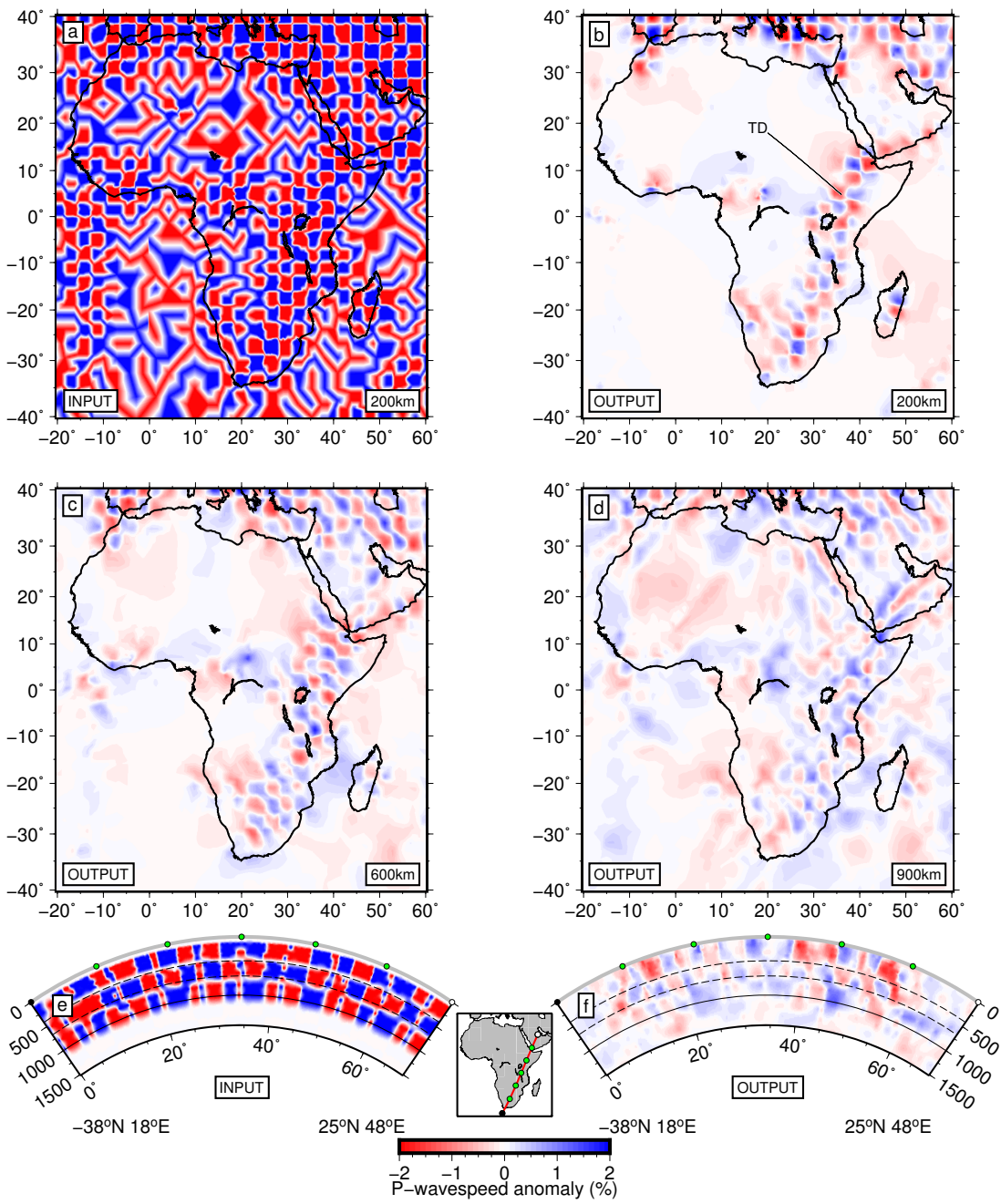


Figure S27. Checkerboard resolution test constructed with 3° width wavespeed anomalies of $\delta V_P = \pm 2.0\%$ input amplitude (a,e). Input anomalies are arranged in an alternating pattern at 200 km, 600 km and 900 km depth but exhibit defects that result from a coarsely parameterized grid in weakly sampled regions (Figure S15). (b-d,f) show recovered anomalies on the same color scale as the input.

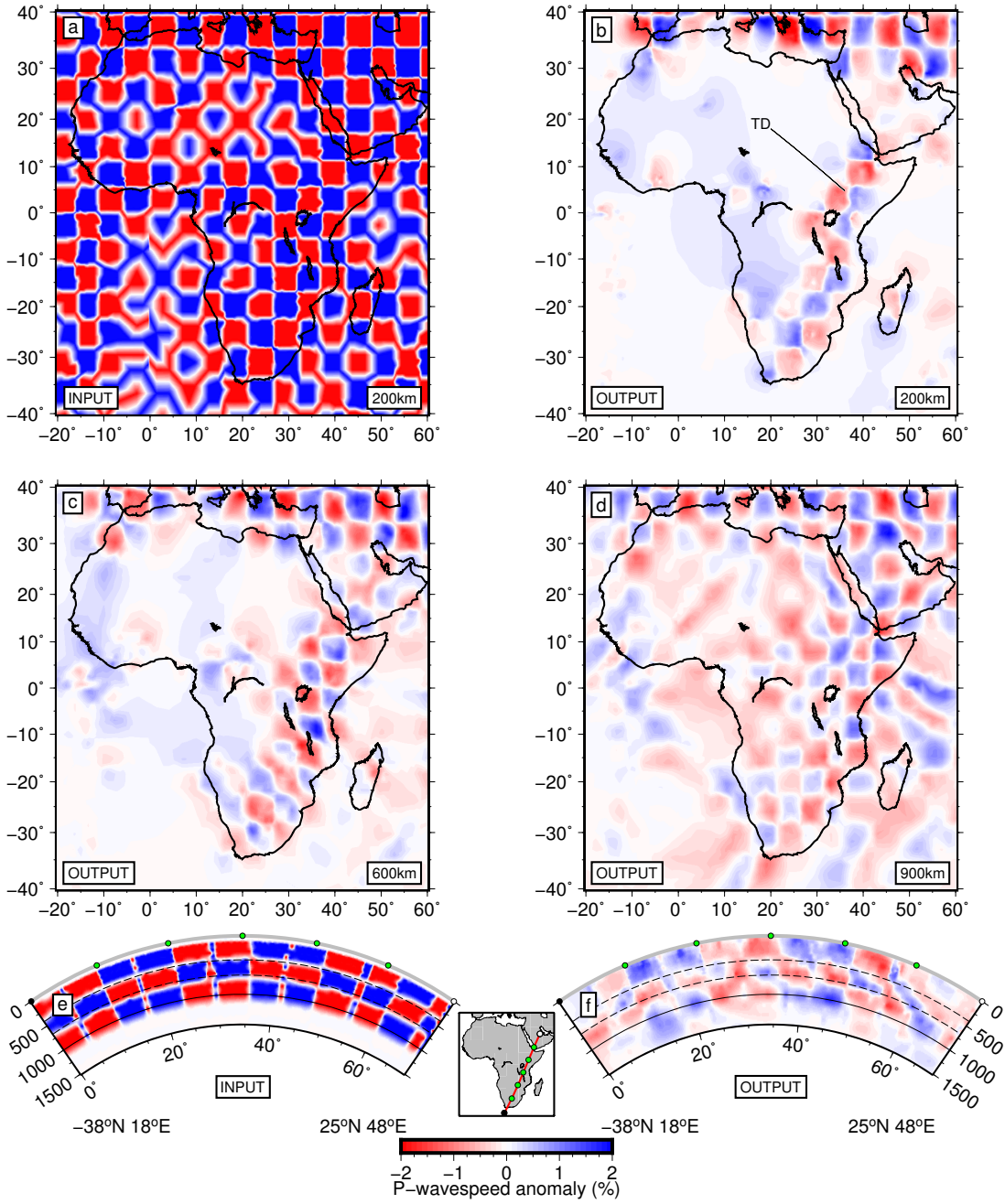


Figure S28. Checkerboard resolution test constructed with 5° width wavespeed anomalies of $\delta V_P = \pm 2.0\%$ input amplitude (a,e). Input anomalies are arranged in an alternating pattern at 200 km, 600 km and 900 km depth but exhibit defects that result from a coarsely parameterized grid in weakly sampled regions (Figure S15). (b-d,f) show recovered anomalies on the same color scale as the input.

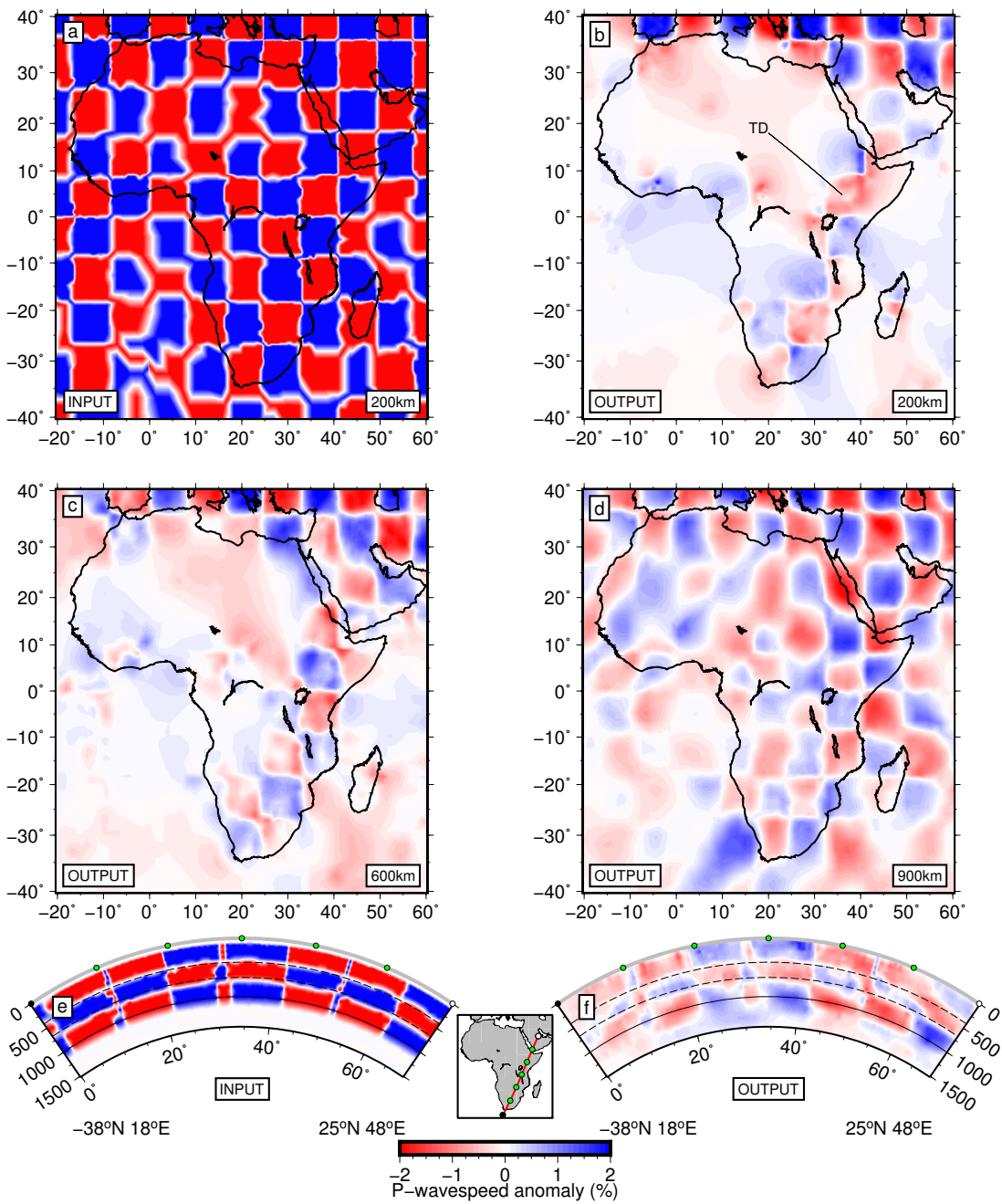


Figure S29. Checkerboard resolution test constructed with 7.5° width wavespeed anomalies of $\delta V_P = \pm 2.0\%$ input amplitude (a,e). Input anomalies are arranged in an alternating pattern at 200 km, 600 km and 900 km depth but exhibit defects that result from a coarsely parameterized grid in weakly sampled regions (Figure S15). (b-d,f) show recovered anomalies on the same color scale as the input.

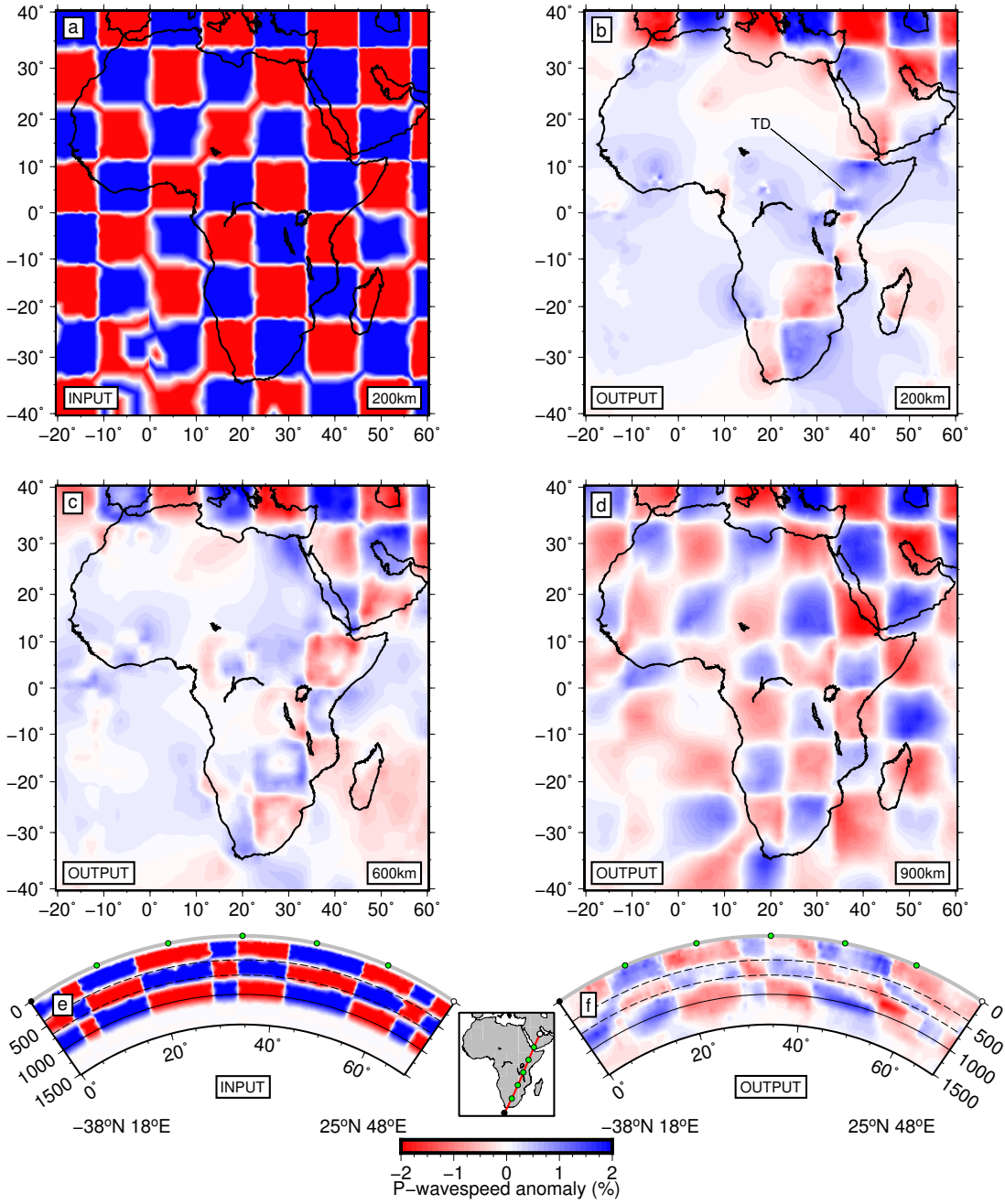


Figure S30. Checkerboard resolution test constructed with 10° width wavespeed anomalies of $\delta V_P = \pm 2.0\%$ input amplitude (a,e). Input anomalies are arranged in an alternating pattern at 200 km, 600 km and 900 km depth but exhibit defects that result from a coarsely parameterized grid in weakly sampled regions (Figure S15). (b-d,f) show recovered anomalies on the same color scale as the input.

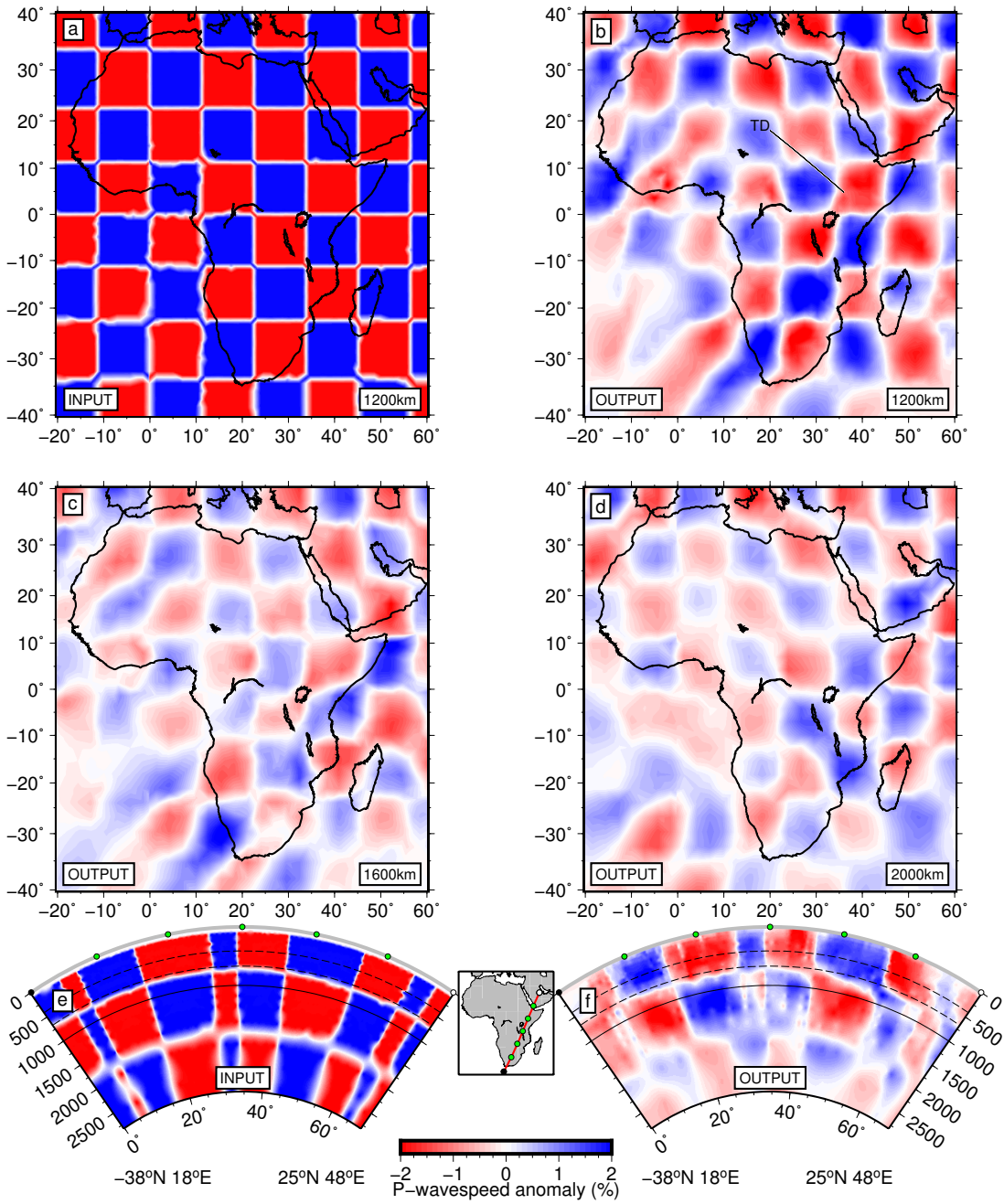


Figure S31. Checkerboard resolution test constructed with 10° width wavespeed anomalies of $\delta V_P = \pm 2.0\%$ input amplitude (a,e), extending into the lower mantle. Input anomalies exhibit defects that result from a coarsely parameterized grid in weakly sampled regions (Figure S15). (b-d,f) show recovered anomalies on the same color scale as the input.

Ray Path Masking

Illumination of the mantle by seismic waves can be approximated using the ray path masking technique outlined by Boyce et al. (2021) in instances such as this, where quantitative measures of tomographic resolution and grid cell hit count are not appropriate. We update the ray path mask of Boyce et al. (2021) to include ray paths from the new African direct-P phase data added here. Please see the supplementary material of Boyce et al. (2021) for further discussion.

AFRP22 Model

Here we plot maps and cross-sections through the continental-scale AFRP22 model (Figures S32–S35). These are chosen purposefully to facilitate comparison with Boyce et al. (2021).

3-D Model Volume Plots

We contour the $\delta V_P = -0.3\%$ wavespeed anomaly within AFRP22 and project the slow wavespeed structures from multiple perspectives (Figures S36–S39). We use AFRP22 without crustal correction to enhance lower mantle visibility because the crustal correction causes a static shift to slower upper mantle oceanic wavespeeds.

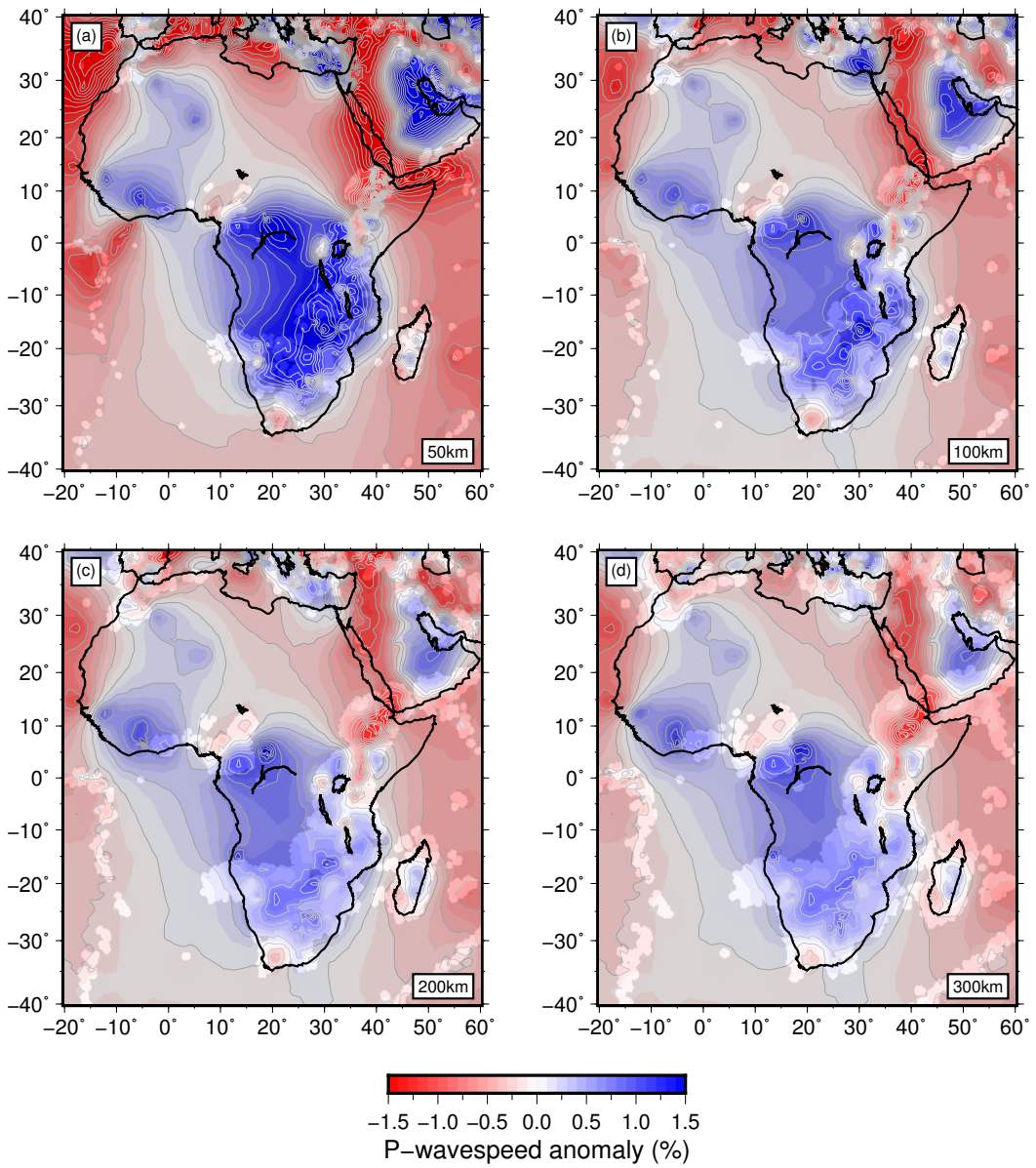


Figure S32. AFRP22 at upper mantle depths of 50 km, 100 km, 200 km and 300 km (*a-d*), plotted as percentage deviation from ak135 ($\delta V_P = \pm 1.5\%$). Regions with a gray mask are not constrained by the AARM-derived African data from temporary seismic stations, only by the global data set (Li et al., 2008).

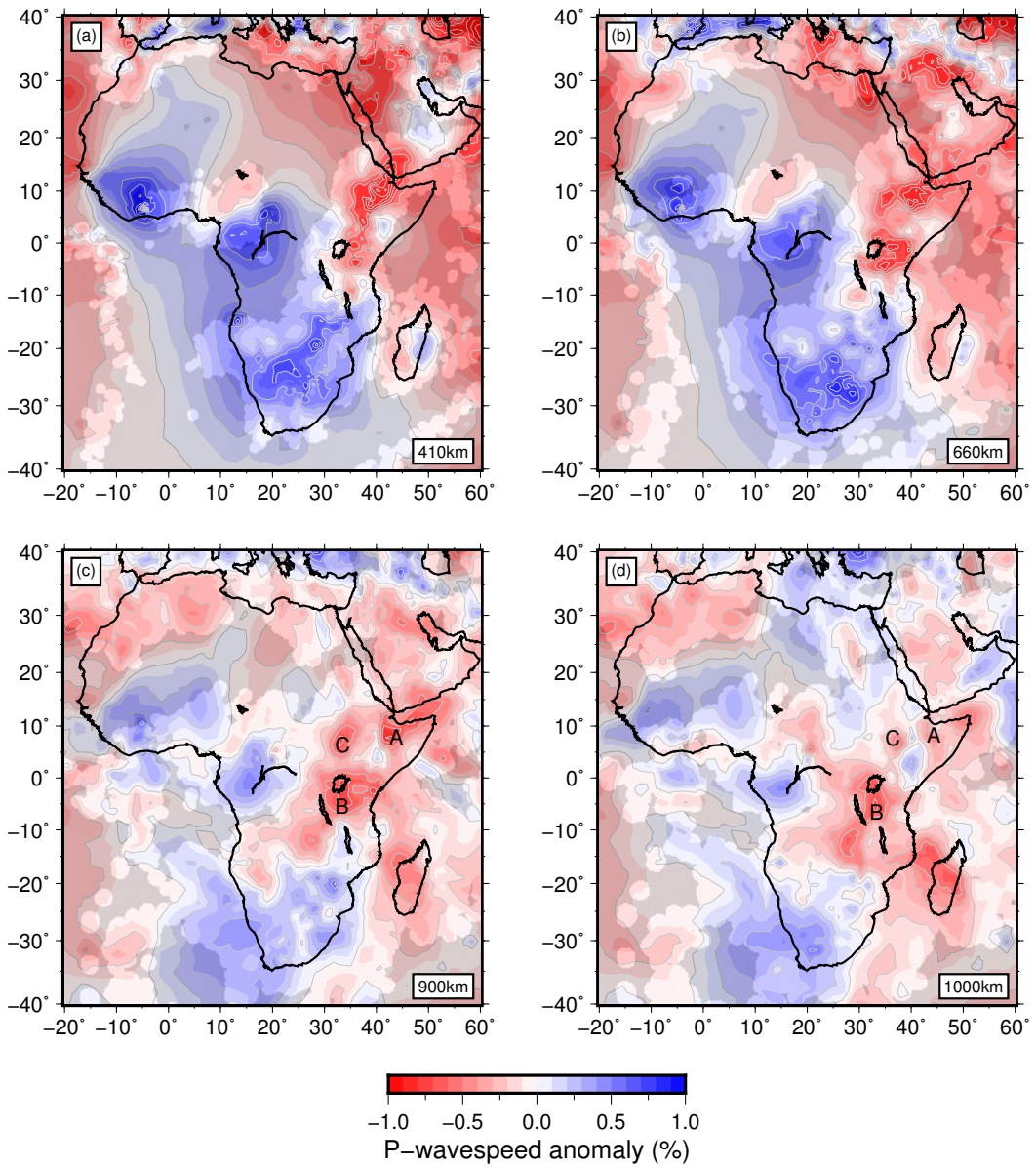


Figure S33. AFRP22 at upper mantle depths of 410 km, 660 km, 900 km and 1000 km (*a-d*), plotted as percentage deviation from ak135 ($\delta V_P = \pm 1.0\%$). Regions with a gray mask are not constrained by the AARM-derived African data from temporary seismic stations, only by the global data set (Li et al., 2008).

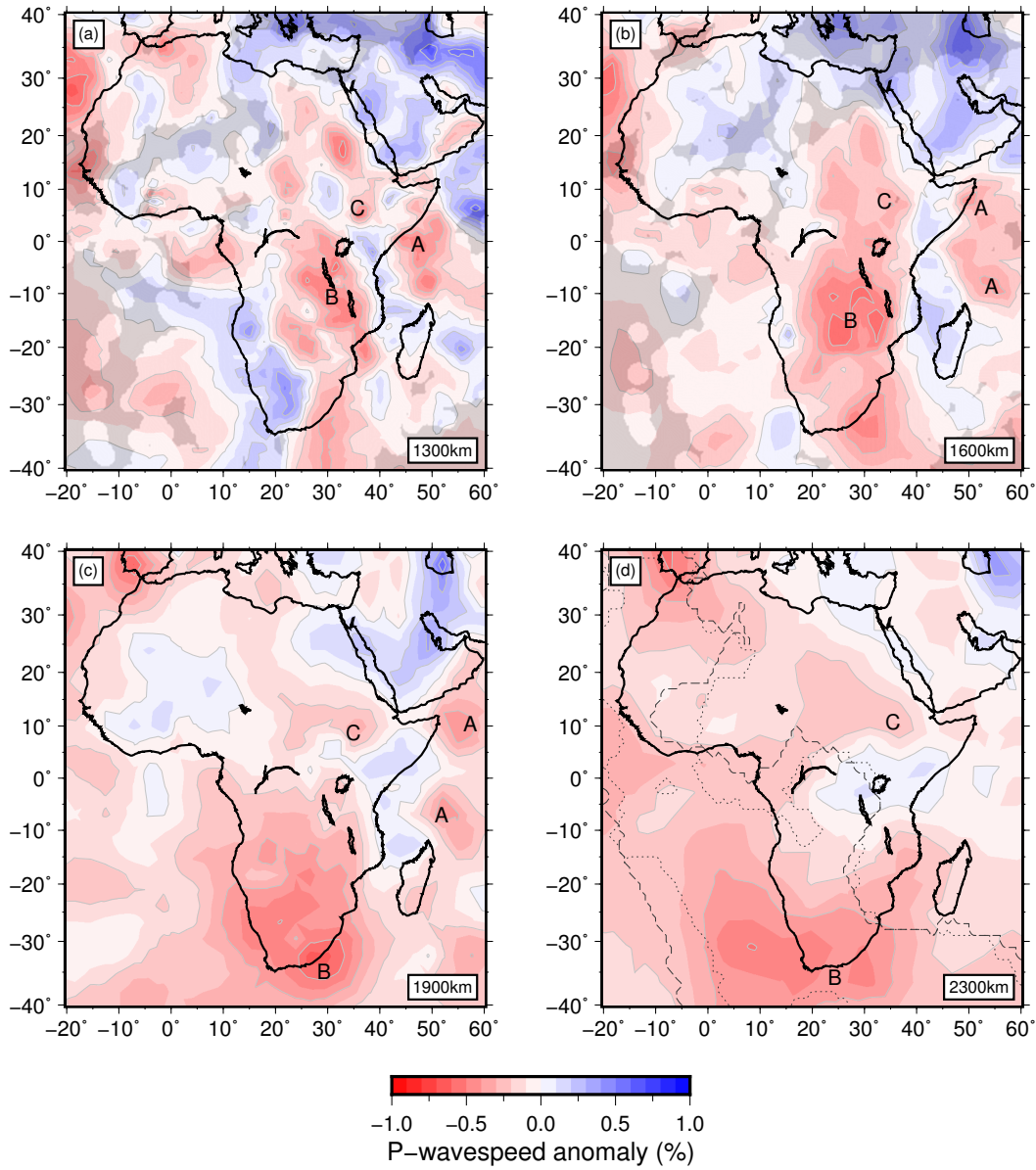


Figure S34. AFRP22 at upper mantle depths of 1300 km, 1600 km, 1900 km and 2300 km (a-d), plotted as percentage deviation from ak135 ($\delta V_P = \pm 1.0\%$). Regions with a gray mask are not constrained by the AARM-derived African data from temporary seismic stations, only by the global data set (Li et al., 2008). Subplot (d) indicates regions of 5/5 slow-wavespeed votes near the core-mantle boundary in δV_S and δV_P tomographic models, respectively as dashed and dotted dark gray lines. Anomaly B lies inside these contours while anomaly A lies outside.

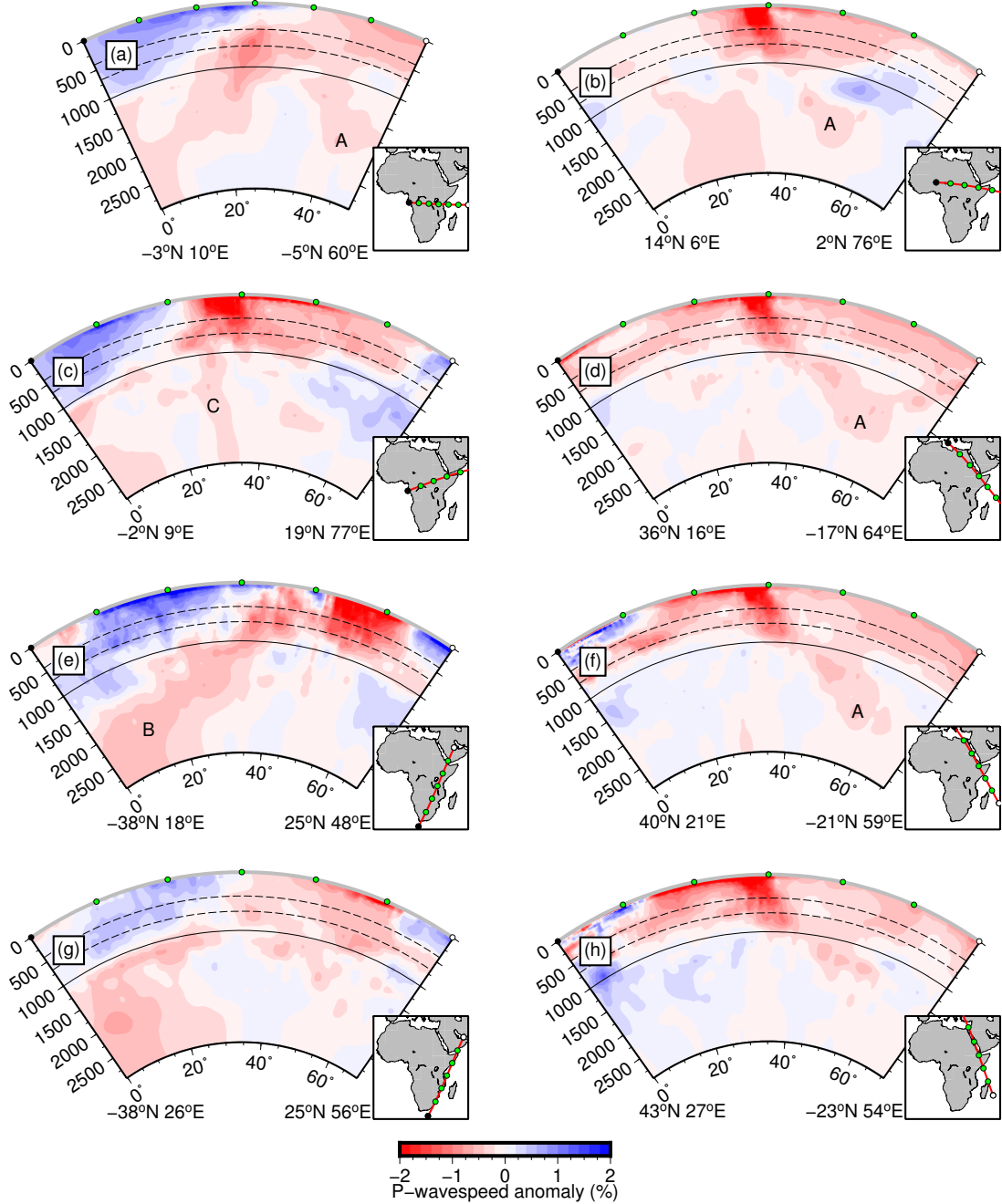


Figure S35. AFRP22 cross-sections (a-h), plotted as percentage deviation from ak135 ($\delta V_P = \pm 2\%$). Locations indicated by the inset map subfigures.

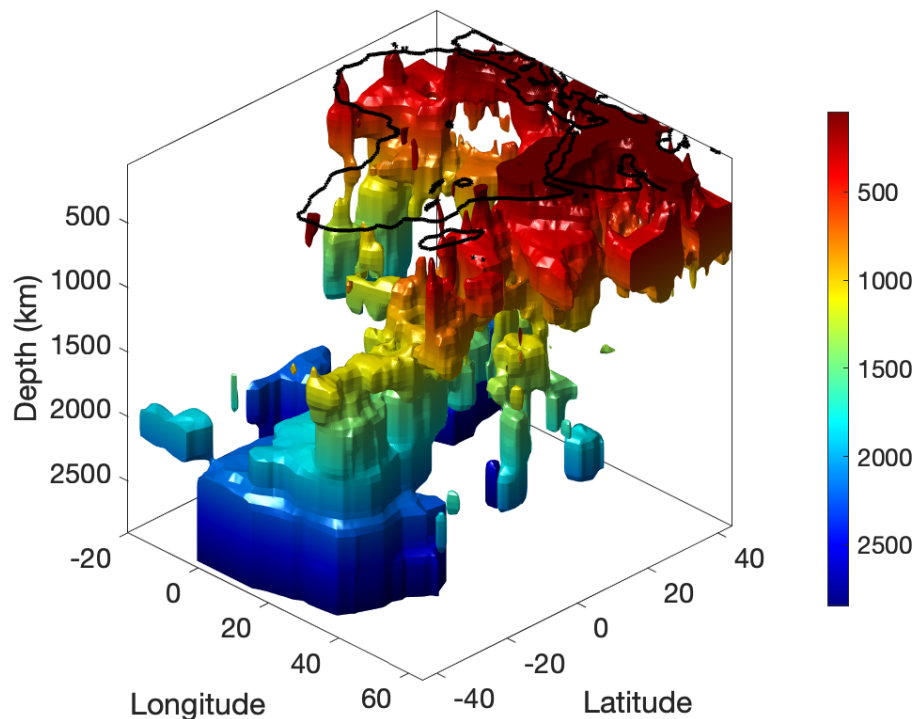


Figure S36. 3-D rendering of $\delta V_P = -0.3\%$ wavespeed anomaly contour within a regularly sampled, lightly smoothed AFRP22 model (50 km in depth, 0.25° horizontally). The African coastline is shown at the surface. Colors show depth within the mantle. View from the southeast, above ground.

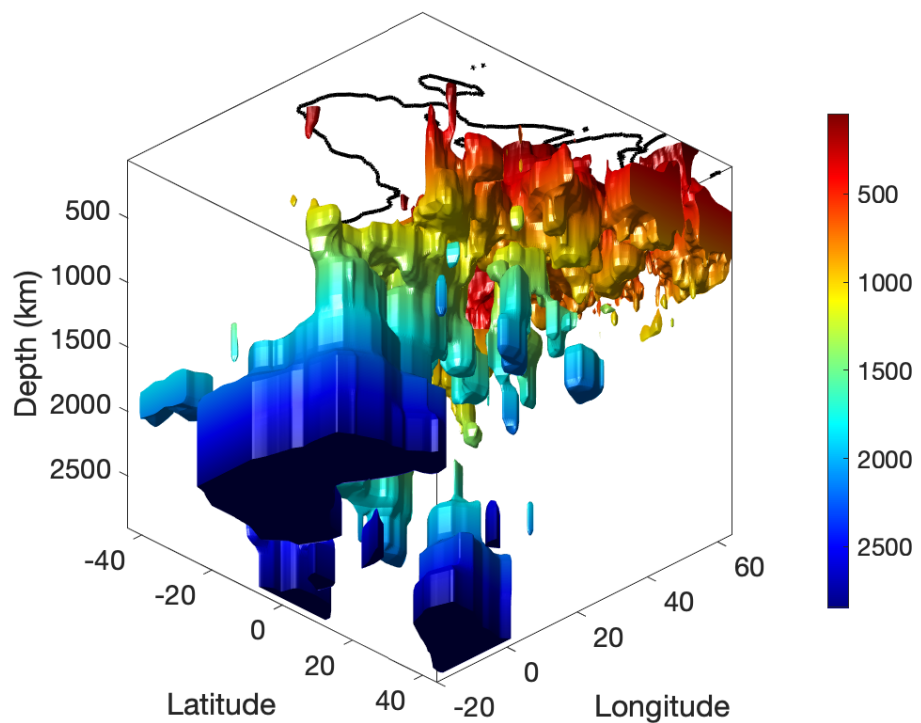


Figure S37. 3-D rendering of $\delta V_P = -0.3\%$ wavespeed anomaly contour within a regularly sampled, lightly smoothed AFRP22 model (50 km in depth, 0.25° horizontally). The African coastline is shown at the surface. Colors show depth within the mantle. View from the southeast, below ground.

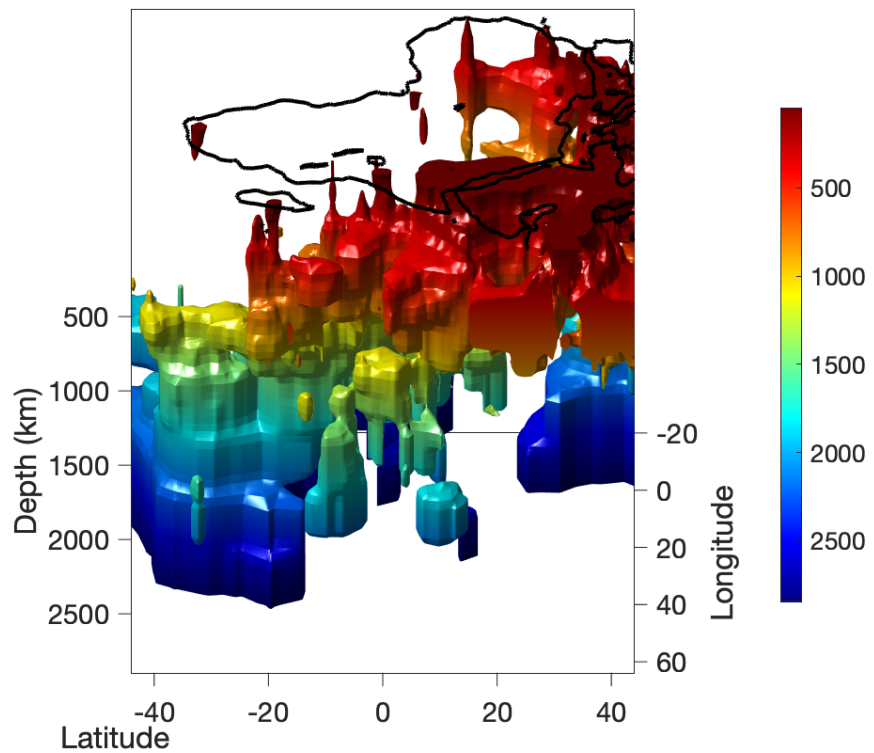


Figure S38. 3-D rendering of $\delta V_P = -0.3\%$ wavespeed anomaly contour within a regularly sampled, lightly smoothed AFRP22 model (50 km in depth, 0.25° horizontally). The African coastline is shown at the surface. Colors show depth within the mantle. View from the east, above ground.

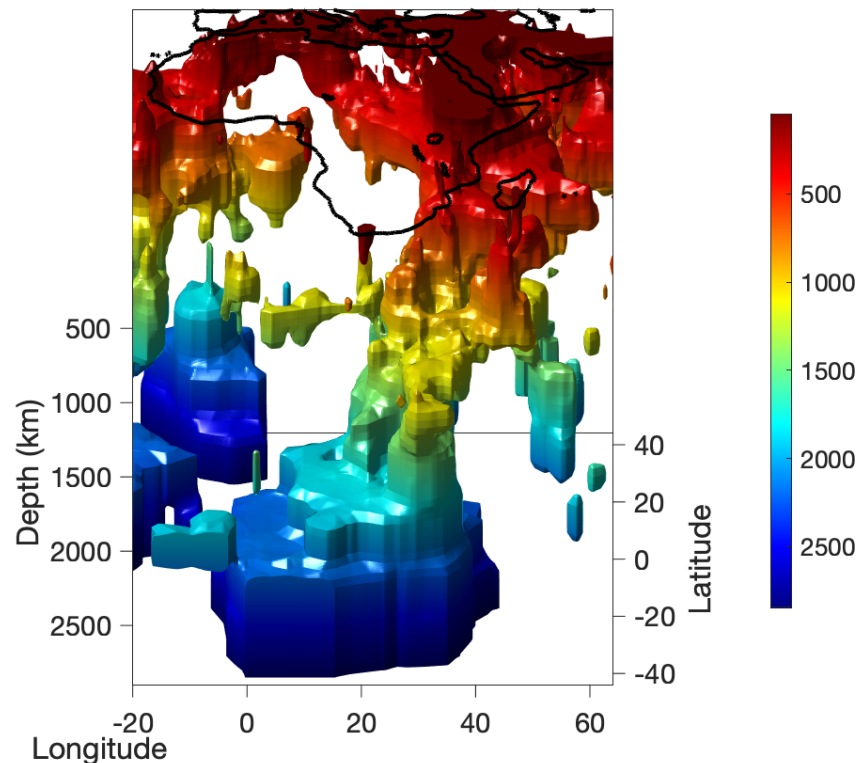


Figure S39. 3-D rendering of $\delta V_P = -0.3\%$ wavespeed anomaly contour within a regularly sampled, lightly smoothed AFRP22 model (50 km in depth, 0.25° horizontally). The African coastline is shown at the surface. Colors show depth within the mantle. View from the south, above ground.

P-wave Model Comparisons

We compare AFRP22 to the global P-wave models PRI-P05 (Montelli et al., 2006), MIT-P08 (Li et al., 2008), LLNL-G3Dv3 (Simmons et al., 2012) and DETOX-P2 (Hosseini et al., 2019) at upper-to-lower mantle depths in Figure S40.

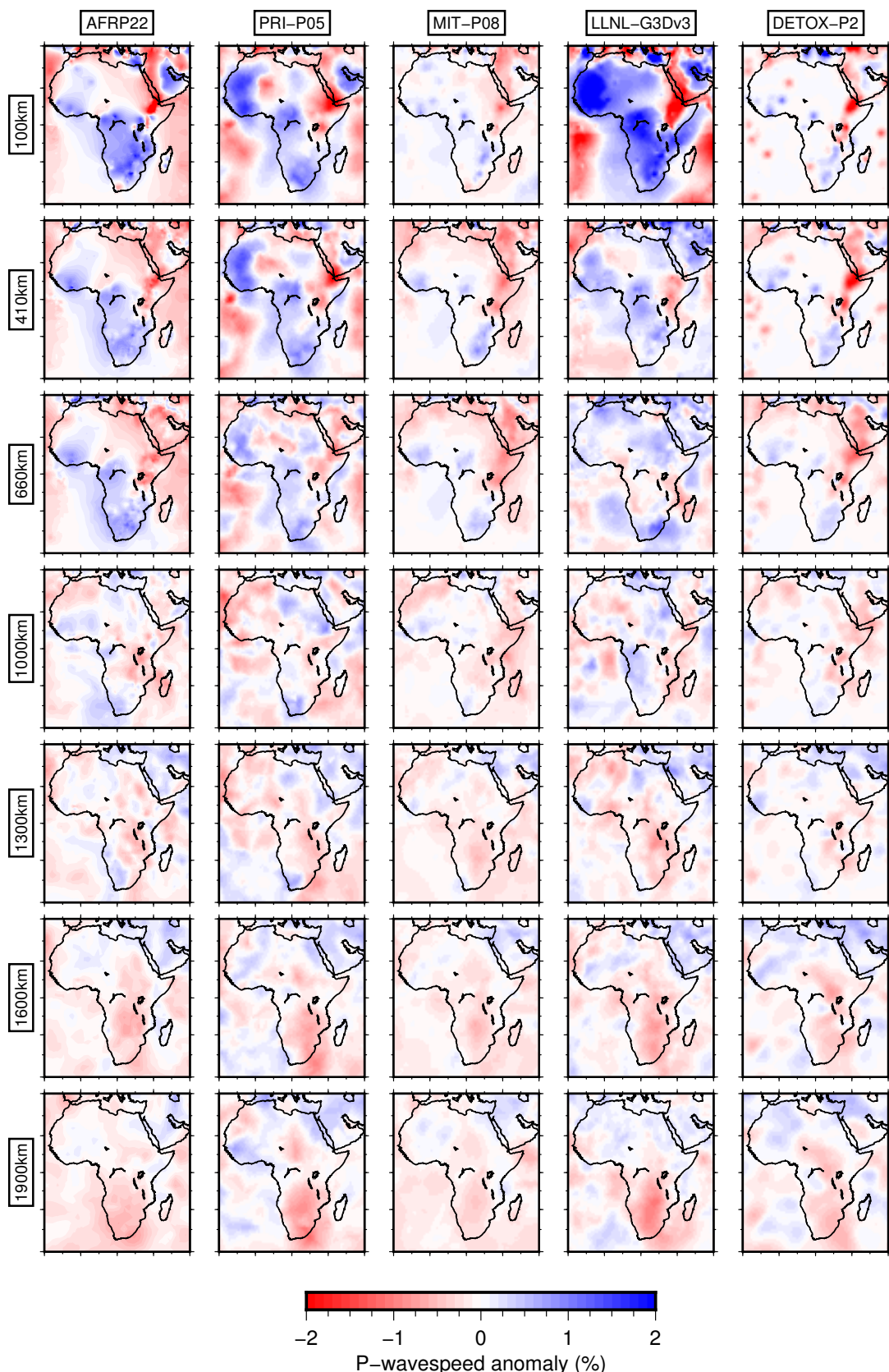


Figure S40. AFRP22 compared to global P-wave models PRI-P05 (Montelli et al., 2006), MIT-P08 (Li et al., 2008), LLNL-G3Dv3 (Simmons et al., 2012) and DETOX-P2 (Hosseini et al., 2019), plotted as percentage with respect to the reference model specific to each model. The closest depth slice within each distributed model is used at each depth.

Receiver Function Data set

Epicentral distance stacks for Pds, PPds and PKPds data sets are shown in Figures S41–S43. Within the distance ranges used, each plot shows clear converted arrivals from the d410 and d660 with very few interfering phases. Figure S44 shows P410s/PP410s/PKP410s piercing points of RFs in the African data set.

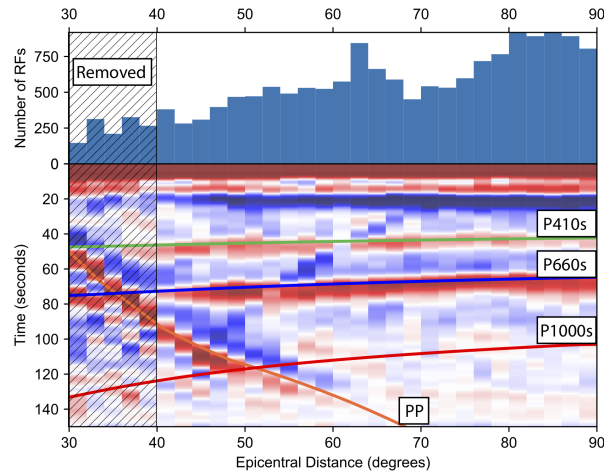


Figure S41. Stack and frequency distribution of 16,701 Pds receiver functions (pre-filtered at 0.01–0.2 Hz) binned by epicentral distance. Epicentral distance bins labeled as “removed” are excluded from further analysis to restrict interference from other phases/multiples with the converted arrivals from the MTZ. Converted phase moveout predictions are labeled.

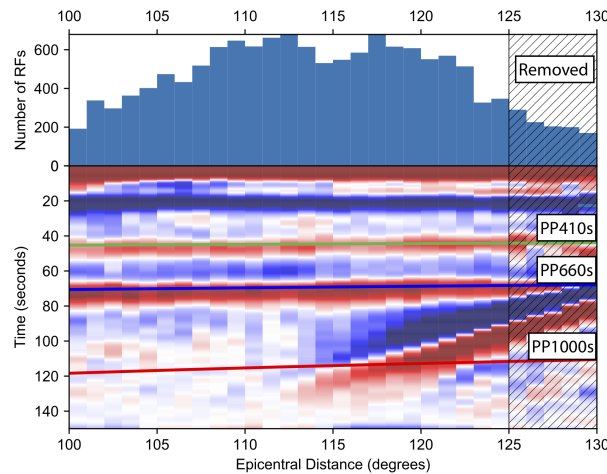


Figure S42. Stack and frequency distribution of 13,865 PPds receiver functions (pre-filtered at 0.01–0.2 Hz) binned by epicentral distance. Epicentral distance bins labeled as “removed” are excluded from further analysis to restrict interference from other phases/multiples with the converted arrivals from the MTZ. Converted phase moveout predictions are labeled.

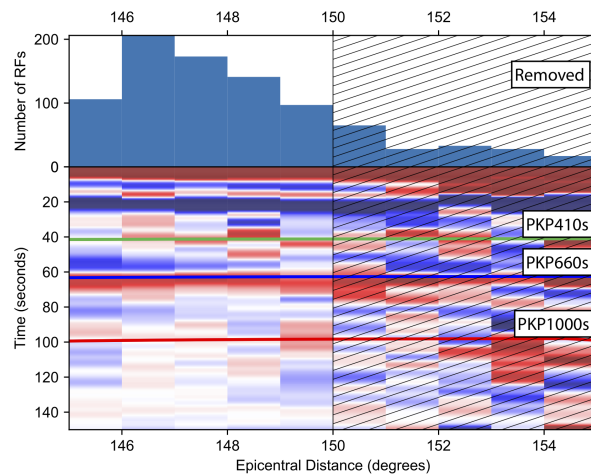


Figure S43. Stack and frequency distribution of 899 PKPds receiver functions (pre-filtered at 0.01–0.2 Hz) binned by epicentral distance. Epicentral distance bins labeled as “removed” are excluded from further analysis to restrict interference from other phases/multiples with the converted arrivals from the MTZ. Converted phase moveout predictions are labeled.

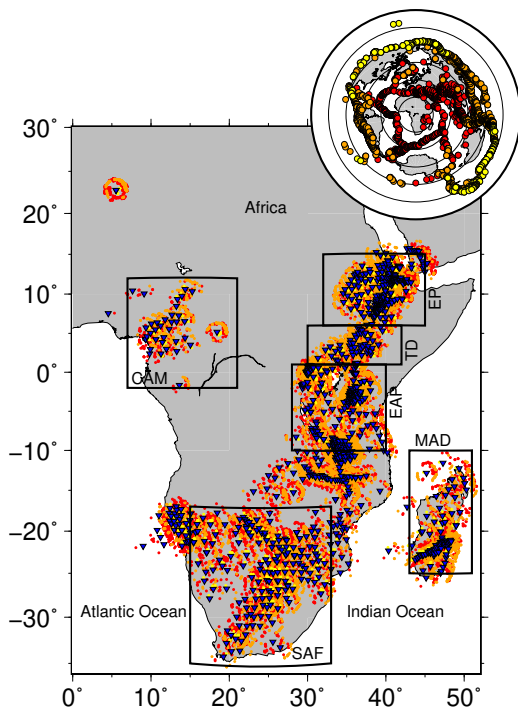


Figure S44. (a) Red/orange/yellow circles indicate P410s/PP410s/PKP410s piercing points; 947 seismograph stations are shown as blue triangles. Inset globe shows 2778 unique earthquakes used for three RF data sets using the same colors. The continent is divided into six subregions: CAM: Cameroon, EYP: Ethiopian-Yemen Plateau, EAP: East African Plateau, MAD: Madagascar, SAF: Southern Africa, TD: Turkana Depression, defined in Table S2.

Regional MTZ Depth and Slowness Stacks

Depth and slowness stacks for RFs whose piercing points at 410 km depth lie within Ethiopia (EYP), Turkana (TD) and East Africa (EAP) are shown in Figures S45–S46. Slowness stacking occurs in the time domain so is not dependent on an assumed velocity model, while depth stacks comprise RFs corrected to depth using AF2019 tomographic models (Celli et al., 2020, Figure S45) and AFRP22 (Figure S46). Regions are shown in Table S2. Conversions from the d410 and d660 are clearly observed with the expected slowness for all regions. No clear top-side multiples from the d410 are observed.

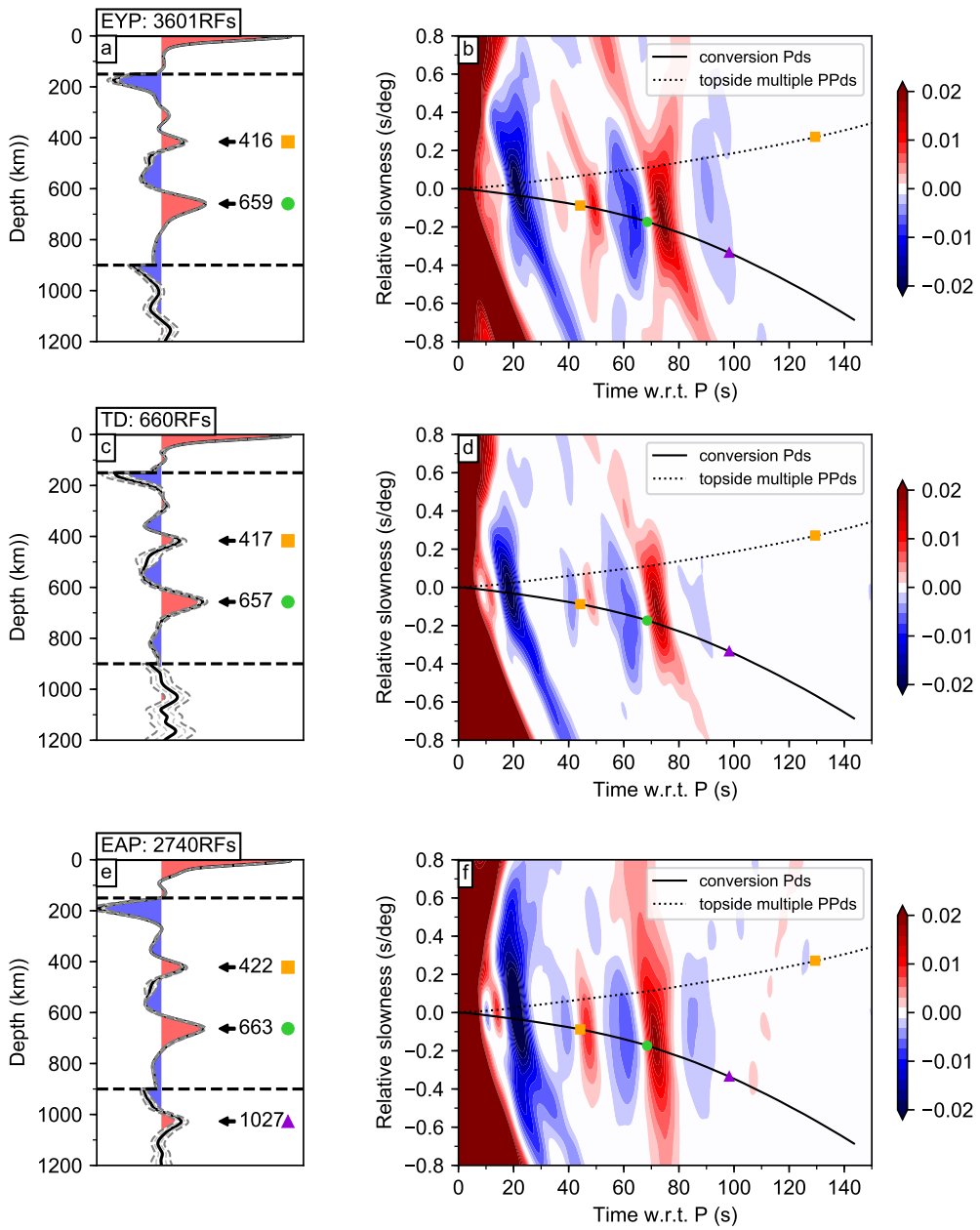


Figure S45. Regional depth (*a,c,e*) and slowness stacks (*b,d,f*) for Pds data whose piercing points at 410 km depth fall within regions EYP, TD, EAP (defined in table S2). RF max frequency is 0.2 Hz. Depth stacks comprise RFs corrected to depth using the AF2019 tomographic model (Celli et al., 2020) within which the depths of high amplitude positive peaks are labeled. Below 150 km and 900 km, depth stack amplitudes are multiplied by five and twenty respectively. Predicted slowness of converted Pds arrivals (solid line) and multiples (dashed line) are shown w.r.t. direct-P phase. Orange square: d410 conversion/multiple. Green circle: d660 conversion/multiple. Violet triangle: d1000 conversion/multiple.

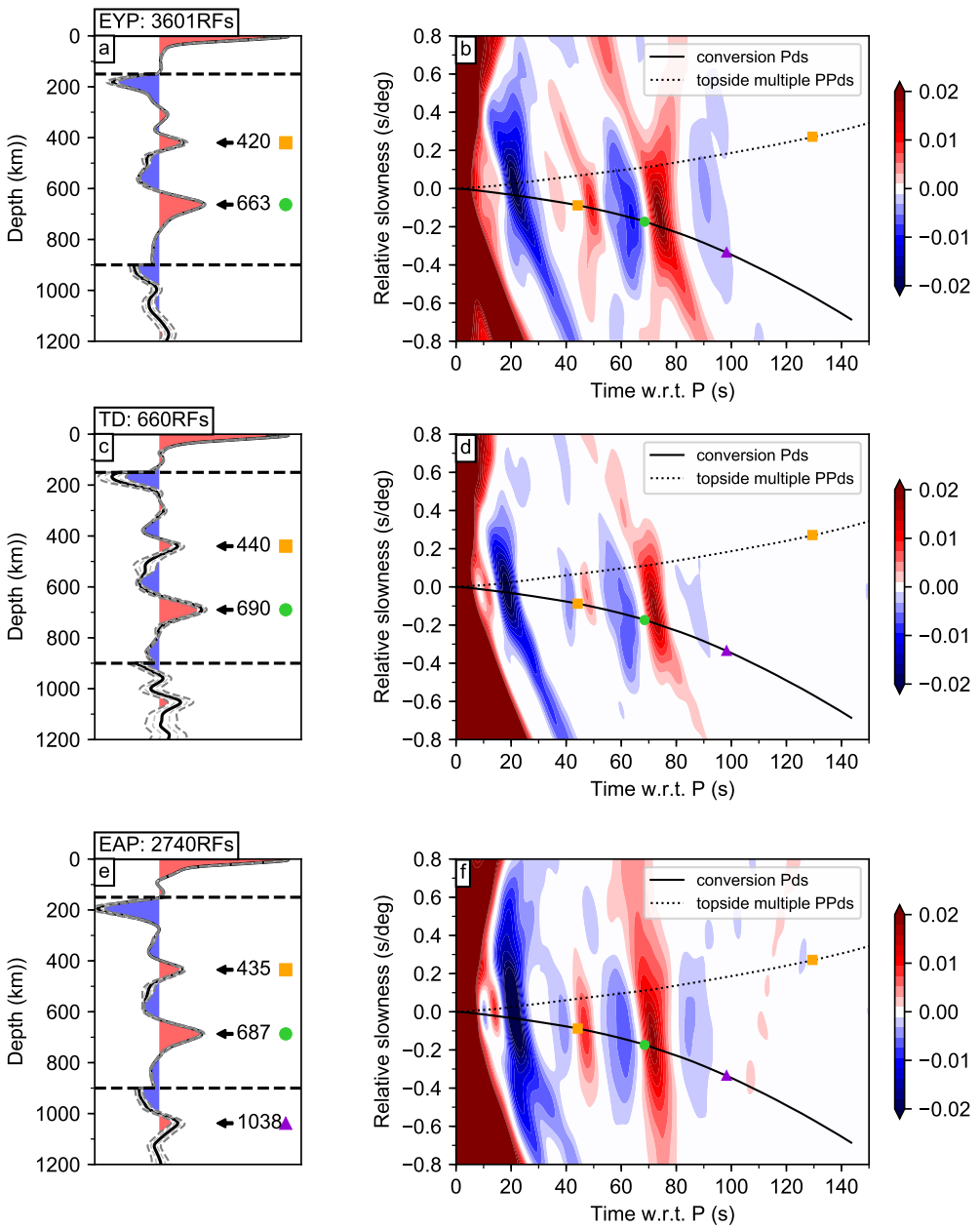


Figure S46. Regional depth (*a,c,e*) and slowness stacks (*b,d,f*) for Pds data whose piercing points at 410 km depth fall within regions EYP, TD, EAP (defined in table S2). RF max frequency is 0.2 Hz. Depth stacks comprise RFs corrected to depth using the AFRP22 tomographic model (presented in the main manuscript) within which the depths of high amplitude positive peaks are labeled. Below 150 km and 900 km, depth stack amplitudes are multiplied by five and twenty respectively. Predicted slowness of converted Pds arrivals (solid line) and multiples (dashed line) are shown w.r.t. direct-P phase. Orange square: d410 conversion/multiple. Green circle: d660 conversion/multiple. Violet triangle: d1000 conversion/multiple.

ak135-CCP: 1D Depth Correction and CCP Stack

We first correct Pds, PPds and PKPds RF data from time-to-depth using the 1D model ak135 and present the resulting common conversion point stack (ak135-CCP). Stacking weights at 410 km, and 660 km are shown in Figure S47, while apparent mantle transition zone discontinuity depth and thickness are shown in Figure S48. As expected, topography on the d410 and d660 is highly correlated (uplift beneath SAF, depression below EAP and EYP: Figure S48) indicating the variability of upper mantle 3D wavespeed structure below Africa.

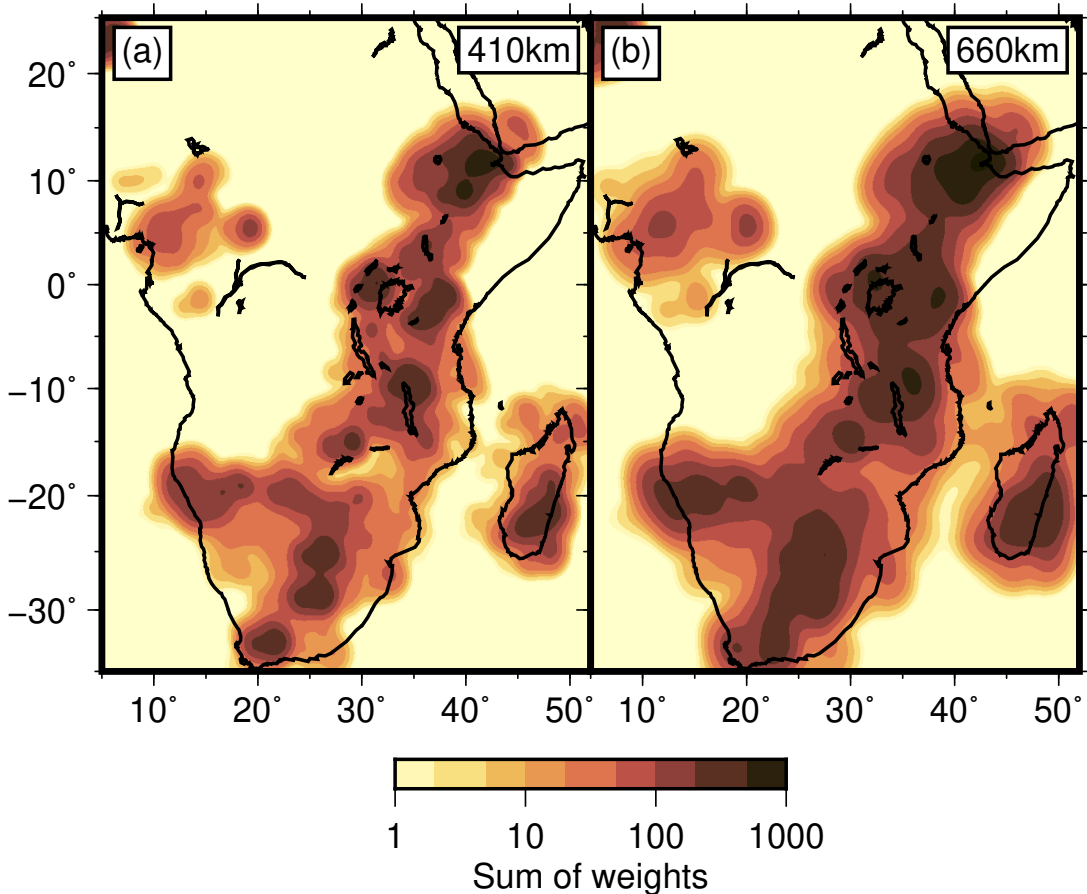


Figure S47. Stacking weights at 410 km (a) and 660 km (b) depth in common conversion point stack volumes combining Pds, PPds and PKPds data sets.

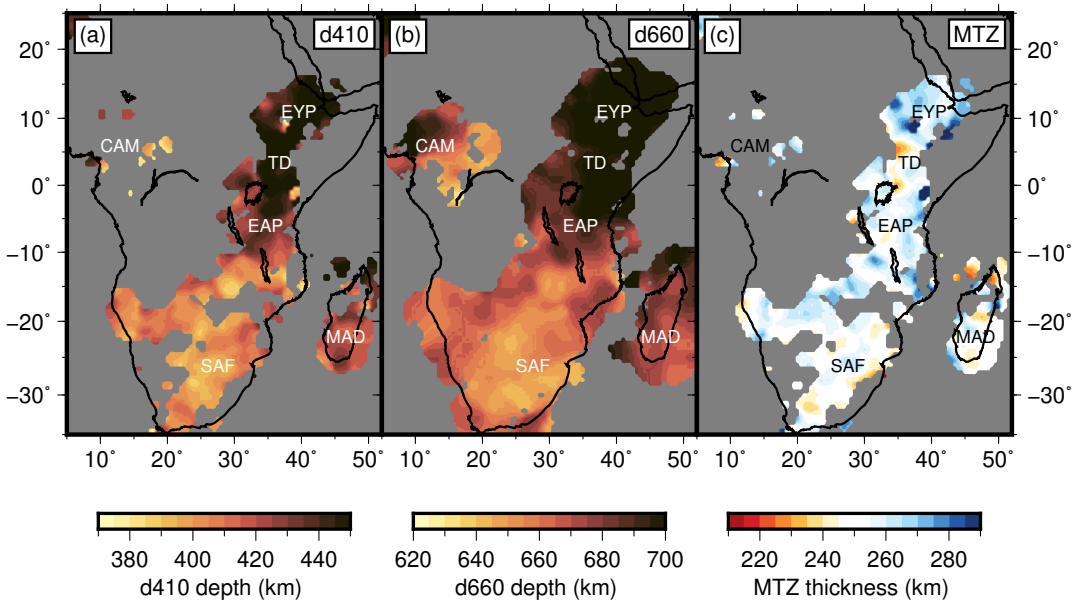


Figure S48. Mantle transition zone (MTZ) discontinuity depths (d410, d660: *a,b*) and thickness (*c*) calculated using Pds, PPds, PKPds data sets (up to 0.2 Hz) corrected to depth using the ak135 1D model and combined into a common conversion point stack (ak135-CCP). Regions are shown only where stacking weight is greater than 2 (Figure S47) and relative amplitude is greater than two standard error from the mean.

Quantitative Depth Correction Assessment

We quantitatively assess the 3D time-to-depth corrections used in our CCP stacks. Tomographic models used in the depth migration are often affected by smearing along ray paths and anomaly amplitude underestimation meaning apparent RF discontinuity depths are often under corrected. We follow the procedures outlined by (van Stiphout et al., 2019; Boyce & Cottaar, 2021), please see the supplementary material of those articles for detailed discussion of the concept. Where all six CCP volumes (ak135-CCP, AFRP22-CCP, AF2019-CCP, SL2013-CCP, SEMUCB-CCP, SGLOBEranı-CCP) exhibit stacking weight greater than 2 (Figure S47), and relative amplitude greater than two standard error from the mean, we extract values for d410 and d660 depths throughout each CCP grid across Africa.

Relative depths are defined compared to the global average $d^R_{410} = d_{410} - 410$, $d^R_{660} = d_{660} - 660$ and corrections on the d410 and d660 (c_{410} , c_{660}) are computed by comparing the depths of discontinuities in the 3D depth corrected CCP stacks (d^{3D}_{410} and d^{3D}_{660}) with those based on the 1D velocity model (d^{1D}_{410} and d^{1D}_{660}). Positive is defined as greater depth i.e. downwards, hence positive corrections occur when the discontinuity within the 3D depth corrected CCP is deeper than that obtained using a 1D velocity model. Negative corrections occur when the discontinuity within the 3D depth corrected CCP is shallower than that obtained using a 1D velocity model.

We measure the Pearson correlation co-efficient (r value) between three sets of variables:

1. Relative d410 depth and relative d660 depth : $r[d^R_{410} : d^R_{660}]$
2. Relative d410 depth and 410 correction : $r[d^R_{410} : c_{410}]$
3. Relative d660 depth and 660 correction : $r[d^R_{660} : c_{660}]$

This framework is used to test a number of properties of the 3D time-to-depth conversions. For a detailed discussion of the expected correlation values please see the Supplementary material to Boyce and Cottaar (2021). In summary, we desire a low value for $r[d^R_{410} : d^R_{660}]$, a negative value for $r[d^R_{410} : c_{410}]$ and a positive value for $r[d^R_{660} : c_{660}]$. It is particularly favorable to obtain values for $r[d^R_{410} : c_{410}]$ and $r[d^R_{660} : c_{660}]$ with equal amplitude and opposite sign because we expect similar Clapeyron slopes of opposite sign in an olivine dominated mantle for the d410 and d660. In regions where

the olivine phase transitions do not dominate the MTZ discontinuity signal, for example in high temperature garnet rich environments, $\mathbf{r}[d^R 660 : c660]$ may be negative.

Relationship between δV_S δV_P in depth migration

We test the relationship $\delta V_S = \delta V_P \times (\text{depth}/2891 + 2)$, assumed by Boyce and Cottaar (2021), for converting P-wavespeed anomalies into the appropriate S-wavespeed anomalies, required for time-to-depth conversion. To obtain δV_S anomalies we keep the multiplication factor of 3 fixed at the core-mantle boundary and vary the surface multiplication factor (F) between 2 and 3. The values between these bounds are scaled linearly. We note that values for F greater than 3, or greater than the core-mantle boundary constraint are uncommon in the literature so are not tested (e.g., Ritsema & Van Heijst, 2002; Tesoniero et al., 2016; Lu et al., 2019). The relationship then becomes the following:

$$\delta V_S = \delta V_P \times \frac{(3 - F) * \text{depth}}{2891} + F \quad (1)$$

We compute time-to-depth corrections for all RFs for this range of F values and subsequently construct CCP stacks from which we extract the three correlation values described above. We can use the same relationship to test the scaling of δV_S to δV_P anomalies used to construct AF2019-CCP.

Figure S49 shows for AFRP22-CCP, varying F produces significant change in all correlation parameters. Acceptable values occur in the range $2.5 \leq F \geq 3.0$, where amplitudes of the correlations on the corrections to the d410 and d660 are balanced at $F = 2.7$. We therefore select this value for use with AFRP22-CCP in the subsequent discussion. Conversely varying F while using AF2019 tomographic model has very little impact on the three correlation statistics and therefore does not yield an acceptable range for this parameter for the values of F that are tested here. We therefore conclude that when using a surface-wave dominated tomographic model for RF CCP stacking, the apparent depths within CCP stacks cannot be improved through exploration of the scaling factor between δV_S and δV_P . P-wavespeed tomographic models appear more sensitive to this scaling and so should be optimized as best as possible. This result is not entirely unexpected because the converted wave travels as a S-wave above the discontinuity in P-to-s RFs.

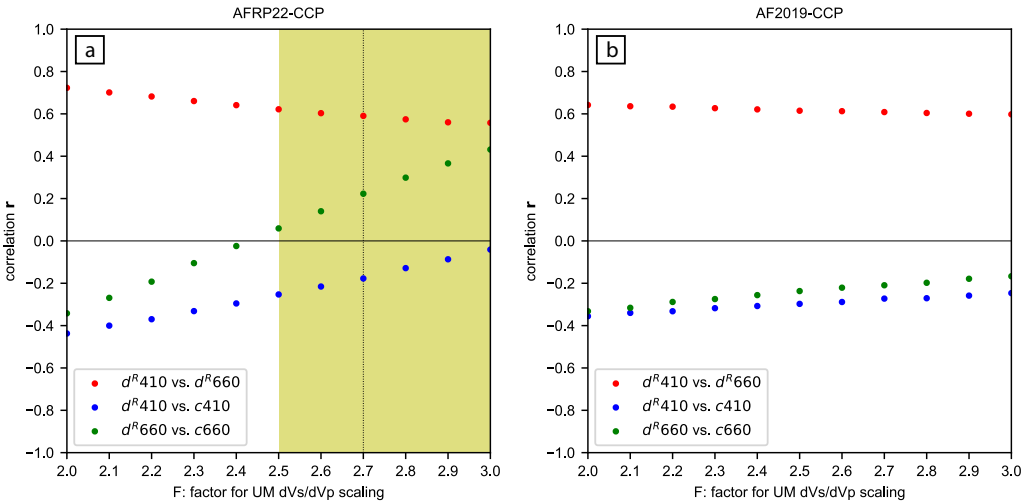


Figure S49. Scatter plots of Pearson correlation for $r[d^R410 : d^R660]$, $r[d^R410 : c410]$ and $r[d^R660 : c660]$ (red, blue and green dots respectively) against the factor for upper mantle δV_S to δV_P scaling (F) for AFRP22-CCP (a), AF2019-CCP (b). The sweet spot for the δV_S to δV_P scaling factor (F) is highlighted in yellow with best fitting scaling factor shown by the dashed vertical line for AFRP22-CCP only. Discussion and definitions are found in the text.

Correlations for final CCP stacks

Results for correlation parameters (Figure S50) for the three CCP stacks ak135-CCP, AFRP22-CCP, AF2019-CCP are broadly similar to that of Boyce and Cottaar (2021). The new data added here is primarily responsible for the significant differences.

As expected, using a 1D velocity model results in a very high $r[d^R410 : d^R660] = 0.90$, and so is not discussed further. AFRP22-CCP yields a moderate $r[d^R410 : d^R660] = 0.62$ and values of $r[d^R410 : c410] = -0.16$ and $r[d^R660 : c660] = 0.25$ with approximately equal magnitude and opposing sign. AFRP22 therefore offers acceptable depth corrections for both the d410 and d660 according to this metric. AF2019-CCP also yields a moderate $r[d^R410 : d^R660] = 0.65$ and negative values for both $r[d^R410 : c410] = -0.36$ and $r[d^R660 : c660] = -0.34$. Under the assumption of an d660 dominated by the olivine transition, the negative value for $r[d^R660 : c660]$ resulting from AF2019 is not desirable. The remaining 3D CCP stacks give the following results – SL2013-CCP: $r[d^R410 : d^R660] = 0.64$, $r[d^R410 : c410] = -0.34$ and $r[d^R660 : c660] = -0.32$; SEMUCB-CCP: $r[d^R410 : d^R660] = 0.52$, $r[d^R410 : c410] = 0.03$ and $r[d^R660 : c660] =$

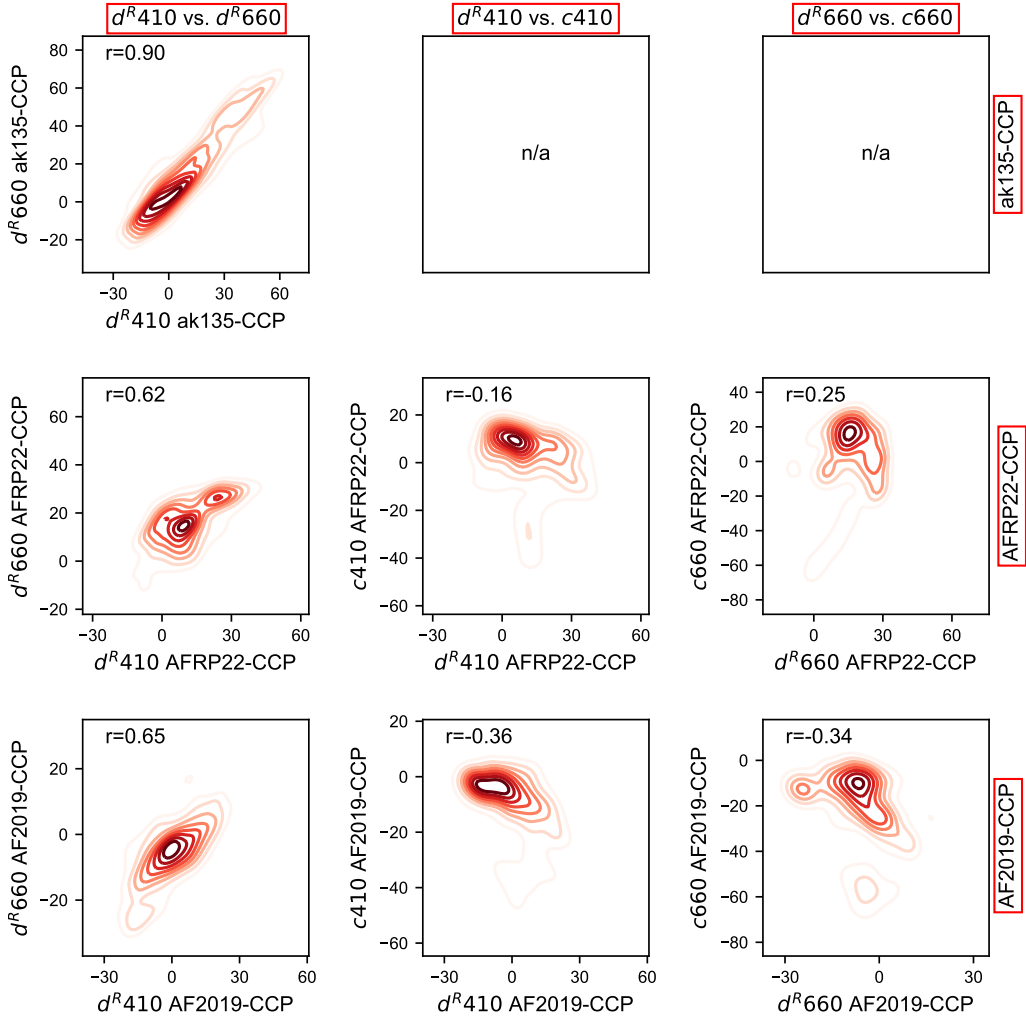


Figure S50. Correlation plot between parameters $\mathbf{r}[d^R_{410} : d^R_{660}]$, $\mathbf{r}[d^R_{410} : c_{410}]$ and $\mathbf{r}[d^R_{660} : c_{660}]$ for MTZ discontinuities in ak135-CCP, AFRP22-CCP, AF2019-CCP. Definitions are given in the text.

0.36; SGLOBE_{ani}-CCP: $\mathbf{r}[d^R_{410} : d^R_{660}] = 0.63$, $\mathbf{r}[d^R_{410} : c_{410}] = -0.39$ and $\mathbf{r}[d^R_{660} : c_{660}] = -0.40$.

It is challenging to categorically discern between these 3D time-to-depth corrected CCP stacks based on these metrics alone. SEMUCB-CCP has the lowest $\mathbf{r}[d^R_{410} : d^R_{660}]$ but has positive values for both correction correlation statistics. Meanwhile AF2019-CCP, SL2013-CCP and SGLOBE_{ani}-CCP have slightly higher $\mathbf{r}[d^R_{410} : d^R_{660}]$ values but have negative values for both correction correlation statistics. AFRP22-CCP has a sim-

ilar $\mathbf{r}[d^R 410 : d^R 660]$ values but is the only model with $\mathbf{r}[d^R 410 : c410]$ and $\mathbf{r}[d^R 660 : c660]$ values of opposing sign and approximately equal amplitude.

Re-scaling Topographic Corrections

To ascertain whether topographic corrections applied by 3D tomographic models (AFRP22, AF2019, SL2013SV, SEMUCB-WM1, SGLOBEran) are reasonable, we re-scale the corrections on the MTZ discontinuity topography, again following Boyce and Cottaar (2021). This approach is similar to that in Section ‘Quantitative Depth Correction Assessment’, but we do not compute a new CCP stack for each scaling factor, we instead assume that re-scaling the corrections approximates re-scaling tomographic amplitudes.

Topographic depth corrections ($c410$ and $c660$) applied by each 3D tomographic model are re-scaled from 0.5–1.9 and correlation parameters are extracted. We evaluate re-scaling factors based on the established reasoning above (e.g., see Figure S49). AF2019-CCP, SL2013-CCP and SGLOBEran-CCP all favor re-scaling to 1.2–1.3, suggesting under correction of discontinuities and underestimation of anomaly amplitudes in the respective tomographic models, as expected for damped least squares inversions (Schaeffer & Lebedev, 2013; Chang et al., 2015). Consistent with the waveform tomography used by French and Romanowicz (2014), SEMUCB-CCP suggests an optimal re-scaling of 0.9 to slightly lower amplitudes. Only AFRP22-CCP suggests a range of possible re-scaling factors could be appropriate (0.9–1.1) for which $\mathbf{r}[d^R 410 : d^R 660]$ is relatively low, and $\mathbf{r}[d^R 410 : c410]$ and $\mathbf{r}[d^R 660 : c660]$ have opposing sign. The preferred value is 1.0 suggesting that the P-wavespeeds in AFRP22 optimized to reduce correlations on the MTZ discontinuities as much as possible when used in conjunction with the appropriate δV_S to δV_P scaling factor (Section ‘Quantitative Depth Correction Assessment’).

3D Depth Correction and CCP Stacks

We use five recent tomographic models within 3D time-to-depth correction and subsequent stacking (AFRP22, AF2019, SL2013SV, SEMUCB-WM1 and SGLOBEran: Celli et al., 2020; Schaeffer & Lebedev, 2013; French & Romanowicz, 2014; Chang et al., 2015). Figures S51–S53 compare the $d410$ depths, $d660$ depths and MTZ thickness from ak135-CCP with that obtained from five 3D time-to-depth corrected CCP stacks: AFRP22-CCP, AF2019-CCP, SL2013-CCP, SEMUCB-CCP, SGLOBEran-CCP. In Figures S54–

S55 we show the mean and standard deviation of d410 depth, d660 depth and MTZ thickness obtained from all five 3D time-to-depth corrected CCP stacks. Average d410 depths beneath EYP are \sim 416 km, \sim 426 km beneath TD and \sim 425 km beneath EAP. Average d660 depths in EYP are \sim 660 km \sim 667 km in TD and \sim 670 km in EAP. Average MTZ thickness beneath EYP is \sim 244 km, \sim 241 km beneath TD and \sim 244 km beneath EAP.

In East Africa, the mean discontinuity depths for both d410 and d660 in EAP are deeper than below EYP (Figure S56) as observed by (Boyce et al., 2021). In Turkana there is significant uncertainty in the discontinuity depths (>10 km), likely due to the variable nature of constraints on upper mantle wavespeed structure below the region across the tomographic models used. However all five CCP stacks resulting from 3D time-to-depth corrections show significantly thinned MTZ (mean of \sim 241 km) and low uncertainty level (\sim 4 km).

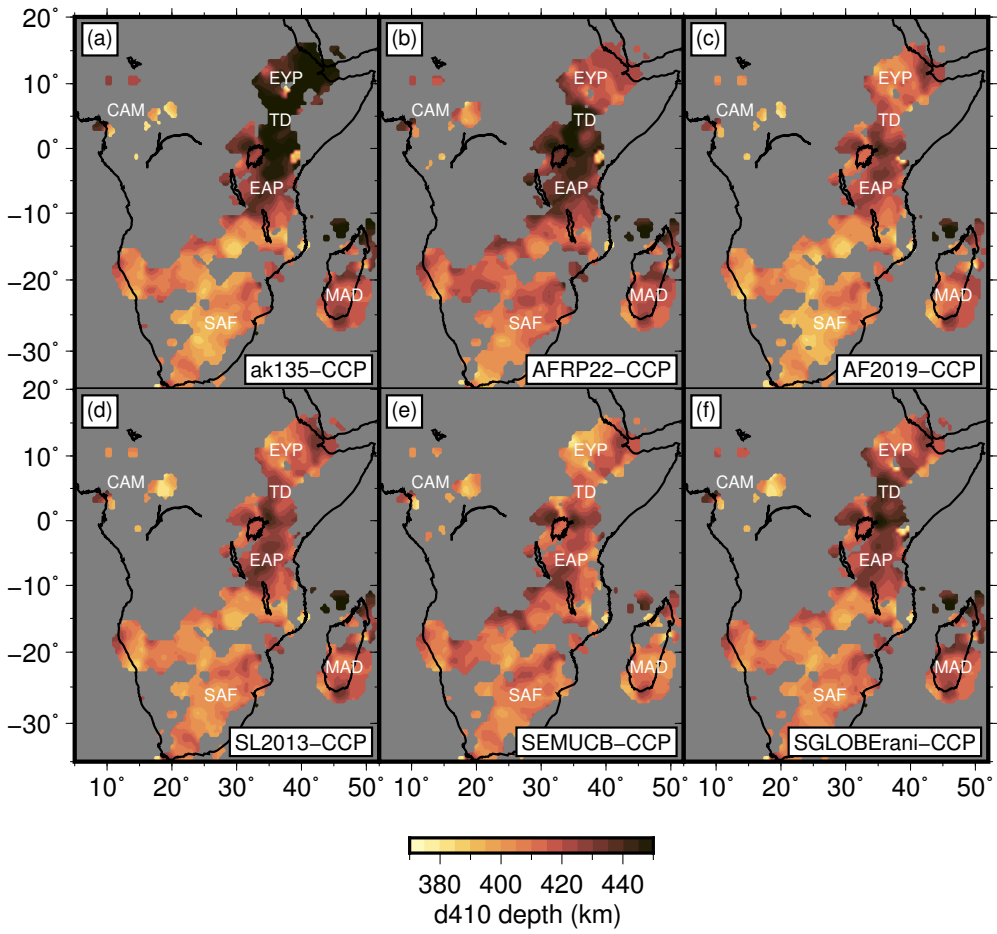


Figure S51. d410 discontinuity depths within common conversion point stacks constructed using RF data of maximum frequencies of 0.2 Hz with varying time-to-depth corrections: ak135-CCP (a), AFRP22-CCP (b), AF2019-CCP (c), SL2013-CCP (d), SEMUCB-CCP (e), SGLOBEani-CCP (f). Results are presented only where stacking weight is greater than 2 (Figure S47) and relative amplitude is greater than two standard error from the mean. CAM: Cameroon, EYP: Ethiopian Plateau, EAP: East African Plateau, MAD: Madagascar, SAF: Southern Africa, TD: Turkana Depression.

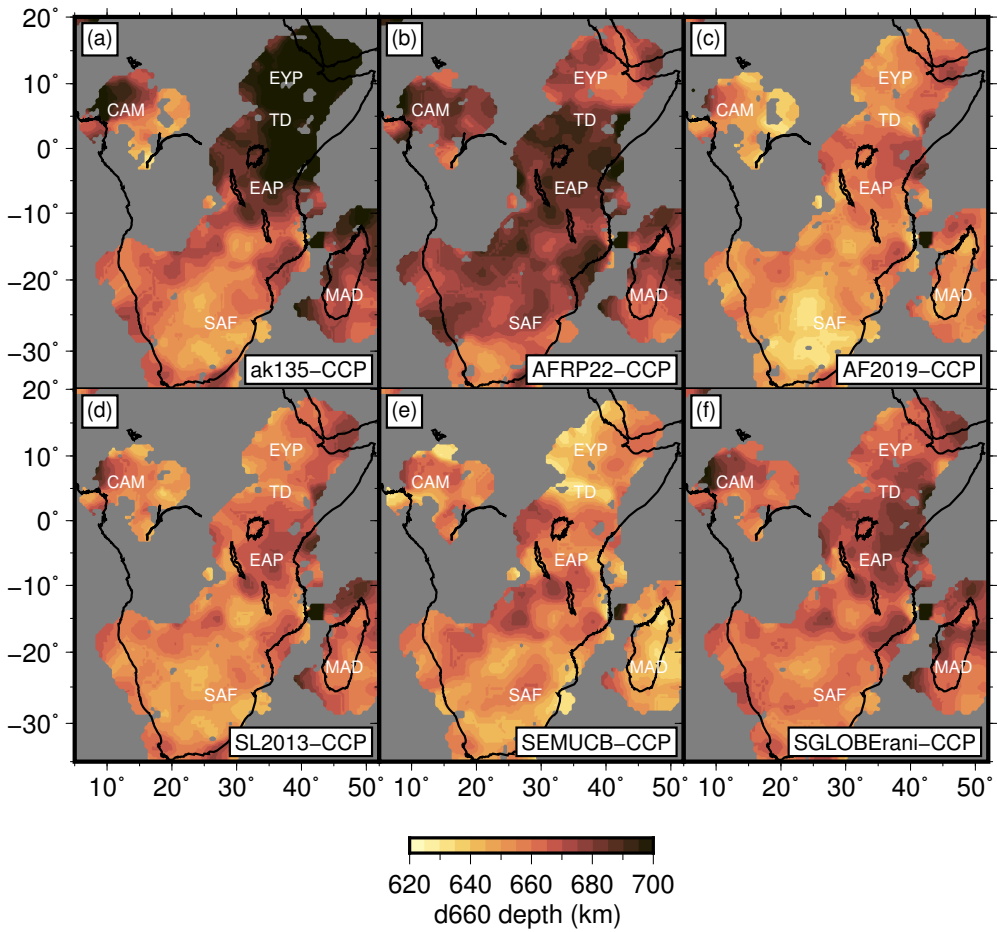


Figure S52. d660 discontinuity depths within common conversion point stacks constructed using RF data of maximum frequencies of 0.2 Hz with varying time-to-depth corrections: ak135-CCP (a), AFRP22-CCP (b), AF2019-CCP (c), SL2013-CCP (d), SEMUCB-CCP (e), SGLOBEani-CCP (f). Results are presented only where stacking weight is greater than 2 (Figure S47) and relative amplitude is greater than two standard error from the mean. CAM: Cameroon, EYP: Ethiopian Plateau, EAP: East African Plateau, MAD: Madagascar, SAF: Southern Africa, TD: Turkana Depression.

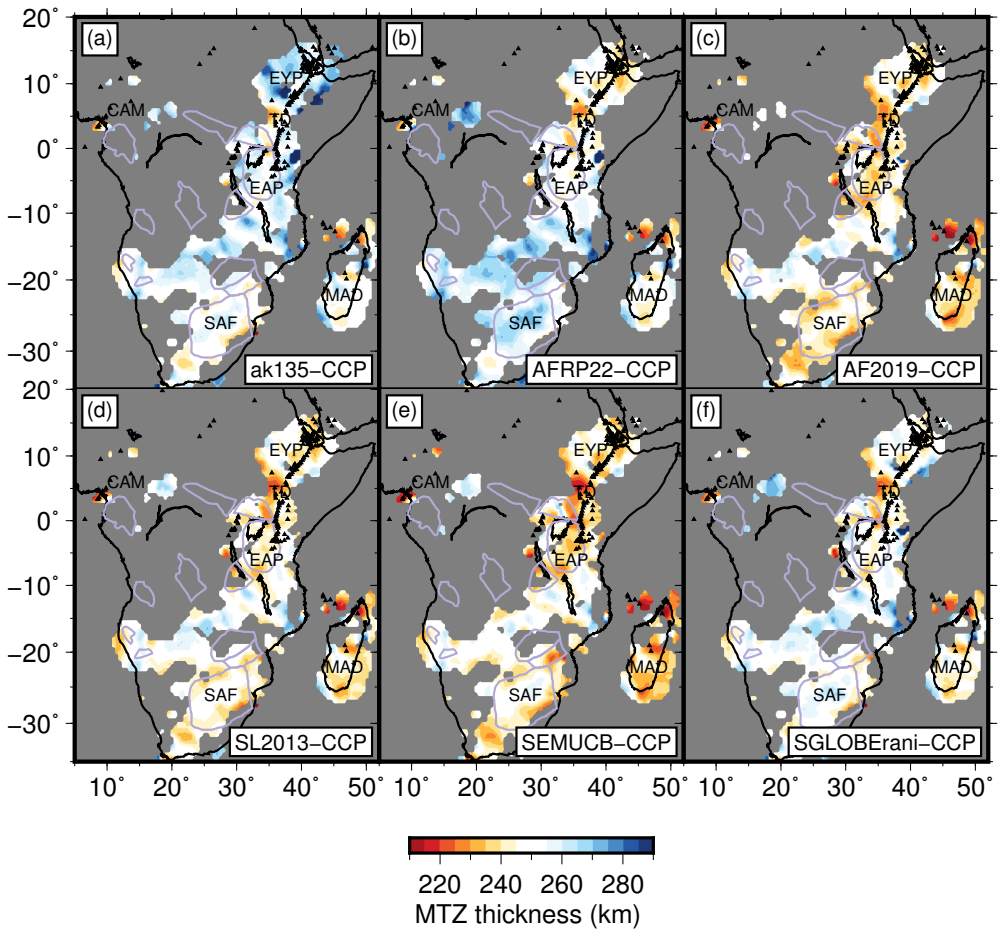


Figure S53. MTZ thickness within common conversion point stacks constructed using RF data of maximum frequencies of 0.2 Hz with varying time-to-depth corrections: ak135-CCP (a), AFRP22-CCP (b), AF2019-CCP (c), SL2013-CCP (d), SEMUCB-CCP (e), SGLOBEranı-CCP (f). Results are presented only where stacking weight is greater than 2 (Figure S47) and relative amplitude is greater than two standard error from the mean. Violet lines: outlines of Archean cratons. CAM: Cameroon, EYP: Ethiopian Plateau, EAP: East African Plateau, MAD: Madagascar, SAF: Southern Africa, TD: Turkana Depression.

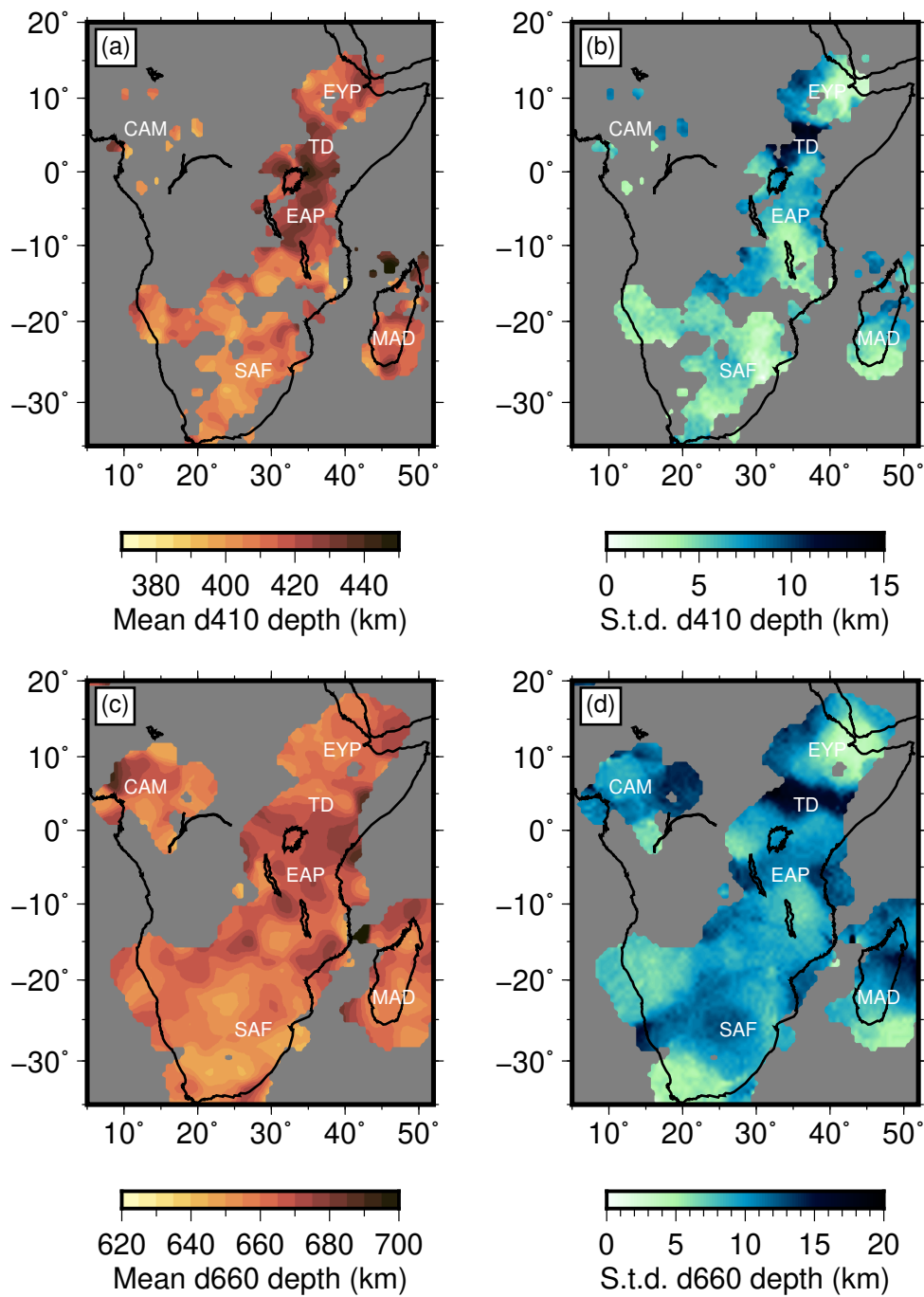


Figure S54. The mean (*a,c*) and standard deviation (*b,d*) of d410 and d660 discontinuity depths are extracted from five 3D time-to-depth corrected CCP stacks: AFRP22-CCP, AF2019-CCP, SL2013-CCP, SEMUCB-CCP, SGLOBEranı-CCP, constructed using RF data of 0.2 Hz maximum frequency. Regions are presented only where all five CCP stacks exhibit stacking weight greater than 2 (Figure S47) and relative amplitude greater than two standard error from the mean. CAM: Cameroon, EYP: Ethiopian Plateau, EAP: East African Plateau, MAD: Madagascar, SAF: Southern Africa, TD: Turkana Depression.

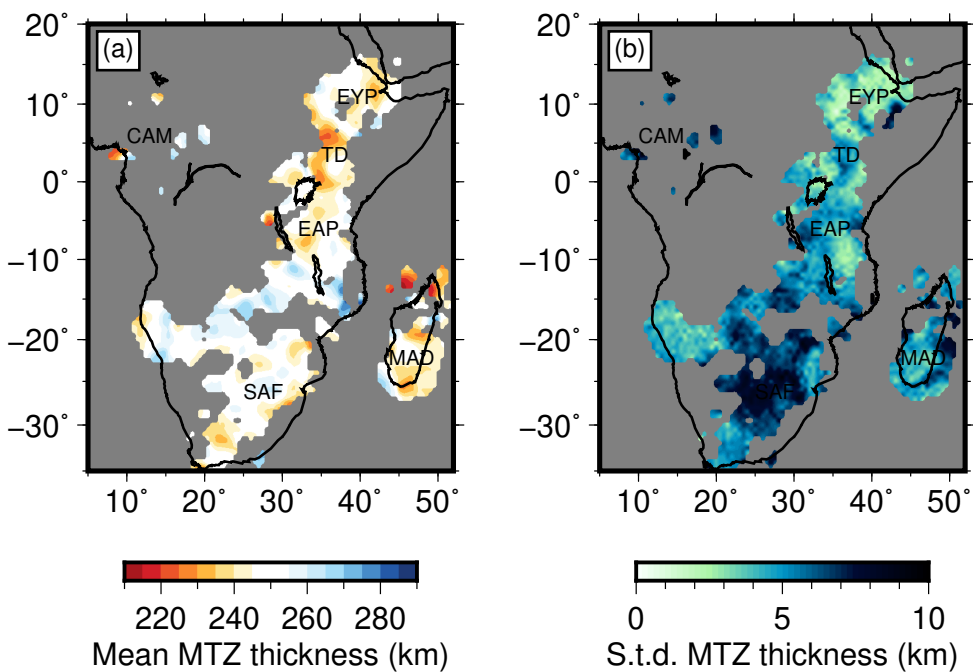


Figure S55. The mean (a) and standard deviation (b) of MTZ thickness are extracted from five 3D time-to-depth corrected CCP stacks: AFRP22-CCP, AF2019-CCP, SL2013-CCP, SEMUCB-CCP, SGLOBEmani-CCP, constructed using RF data of 0.2 Hz maximum frequency. Regions are presented only where all five CCP stacks exhibit stacking weight greater than 2 (Figure S47) and relative amplitude greater than two standard error from the mean. CAM: Cameroon, EYP: Ethiopian Plateau, EAP: East African Plateau, MAD: Madagascar, SAF: Southern Africa, TD: Turkana Depression.

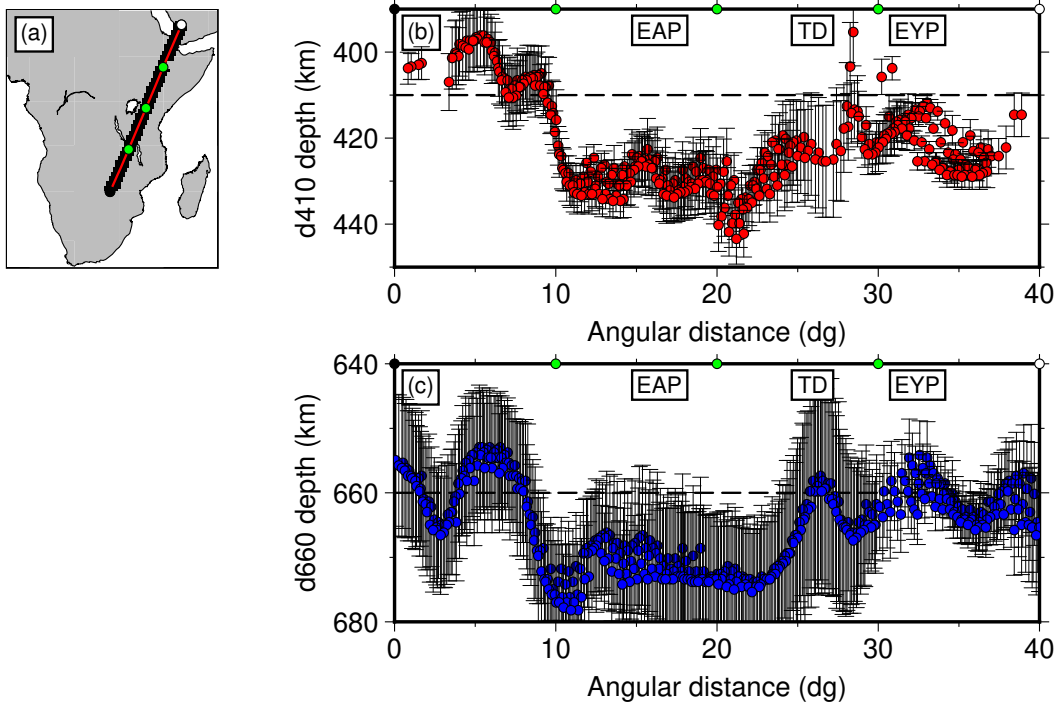


Figure S56. d410 and d660 sampling points (black squares) within 150 km distance of the red profile shown in (a) are extracted from the mean CCP stack (Figure S54) and projected into plane in subfigures (b,c). Mean d410 (red points - b) and d660 (blue points - c) depths are shown. Error bars are associated with the standard deviation of discontinuity depths resulting from variable time-to-depth corrections from the five tomographic models. EYP: Ethiopian Plateau, EAP: East African Plateau, TD: Turkana Depression.

AFRP22-CCP Frequency Testing

Figures S57–S58 show d410 and d660 depths for AFRP22-CCP and AF2019-CCP for a range of RF maximum frequencies (0.2–0.9 Hz). Similarly to Boyce and Cottaar (2021), the d660 depth varies with maximum RF frequency below EAP whilst the d410 is largely insensitive to RF maximum frequency throughout Africa.

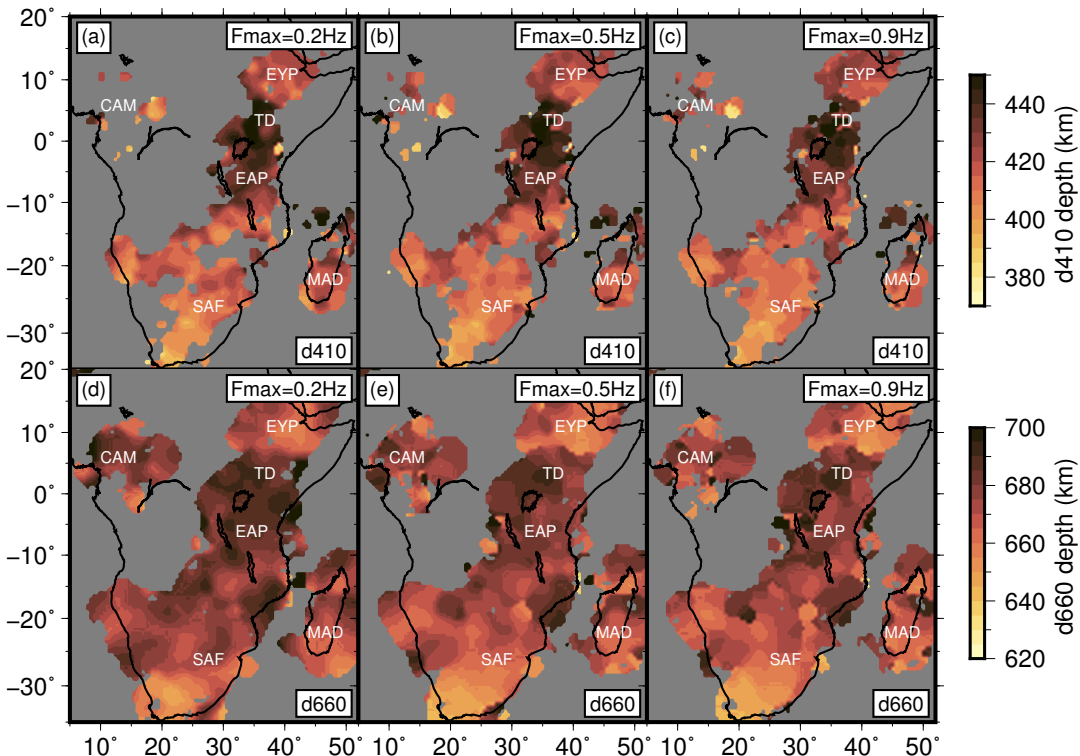


Figure S57. Maps of d410 (a–c) and d660 (d–f) depth for AFRP22-CCP computed using RFs with maximum frequencies ranging from 0.2–0.9 Hz.

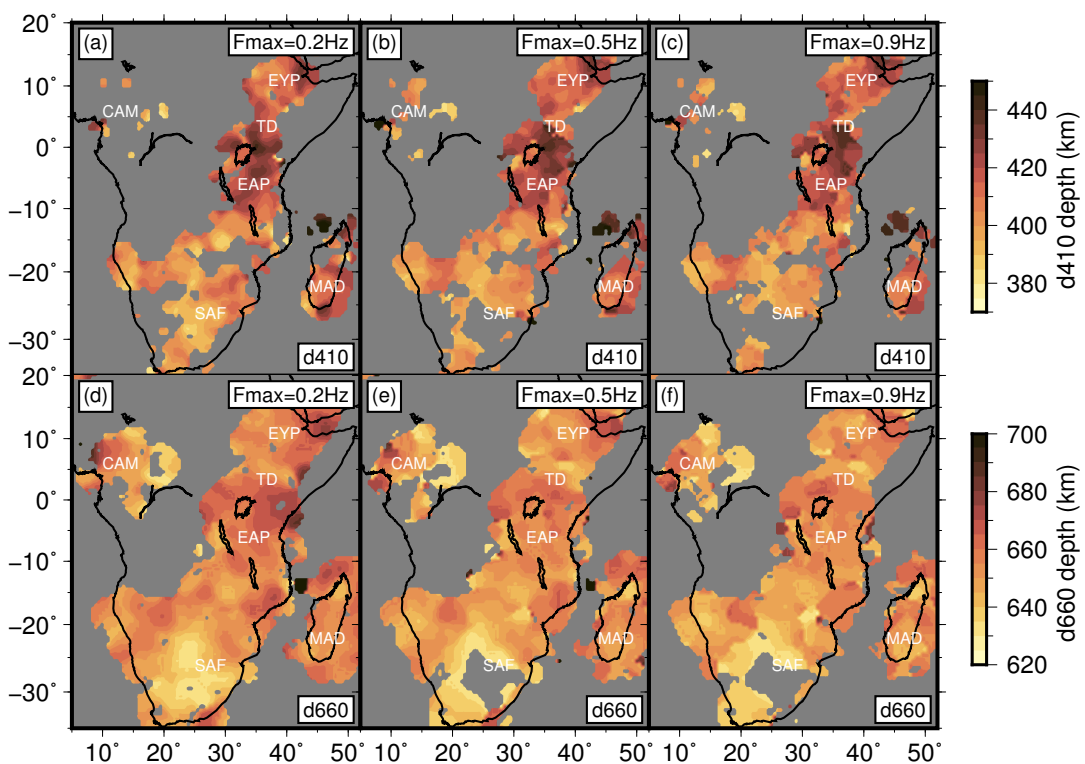


Figure S58. Maps of d410 (a–c) and d660 (d–f) depth for AF2019-CCP computed using RFs with maximum frequencies ranging from 0.2–0.9 Hz.

Mantle Transition Zone Discontinuity Values

We provide median, mean and standard deviation of d410, d660 depths and MTZ thicknesses within the regions defined in Table S2 within AFRP22-CCP, AF2019-CCP, SL2013-CCP, SEMUCB-CCP and SGLOBEranı-CCP in Tables S3–S5. Values are derived from CCP stacks calculated using RF data of maximum frequency 0.2 Hz and two Fresnel zone half width smoothing. Regional definitions are also appropriate for depth and slowness stacks (Section ‘Regional MTZ Depth and Slowness Stacks’).

| Region | Regional bounds | | | |
|--------|-----------------|---------------|---------------|---------------|
| | Min. Lon. (°) | Max. Lon. (°) | Min. Lat. (°) | Max. Lat. (°) |
| AFR | 5 | 52 | -35 | 20 |
| EYP | 32 | 45 | 6 | 15 |
| TD | 30 | 42 | 1 | 6 |
| EAP | 28 | 40 | -10 | 1 |
| CAM | 7 | 21 | -2 | 12 |
| MAD | 43 | 51 | -25 | -10 |
| SAF | 15 | 33 | -35 | -17 |

Table S2. Geographic bounds for regions reporting d410, d660 depths and MTZ thickness, depth and slowness stacks.

| Region | CCP d410 depths (km) | | | | | | | | | | | | | | | | |
|--------|----------------------|-------|--------|-------|------------|--------|-------|-------|------------|-------|-------|--------|------------|-------|--------|-----|----------------|
| | AFRP22-CCP | | | | AF2019-CCP | | | | SL2013-CCP | | | | SEMUCB-CCP | | | | SGLOBEmani-CCP |
| | MED. | MN. | S.T.D. | MED. | MN. | S.T.D. | MED. | MN. | S.T.D. | MED. | MN. | S.T.D. | MED. | MN. | S.T.D. | MN. | S.T.D. |
| AFR | 418.6 | 420.4 | 13.4 | 408.6 | 409.8 | 12.5 | 412.6 | 413.2 | 12.2 | 410.6 | 411.7 | 10.2 | 414.6 | 415.7 | 12.8 | | |
| EYP | 420.6 | 421.8 | 7.6 | 412.6 | 413.8 | 8.6 | 416.6 | 415.9 | 9.0 | 408.6 | 408.4 | 10.6 | 420.6 | 419.2 | 10.0 | | |
| TD | 440.6 | 440.9 | 8.8 | 420.6 | 419.3 | 8.4 | 422.6 | 421.5 | 8.1 | 414.6 | 415.5 | 9.5 | 434.6 | 431.0 | 9.6 | | |
| EAP | 434.6 | 434.4 | 9.9 | 420.6 | 421.3 | 8.7 | 424.6 | 423.8 | 7.4 | 418.6 | 419.9 | 9.3 | 426.6 | 426.3 | 10.2 | | |
| CAM | 410.6 | 411.7 | 13.9 | 396.5 | 401.3 | 15.0 | 398.5 | 400.7 | 14.8 | 401.6 | 402.3 | 10.9 | 400.5 | 404.2 | 17.6 | | |
| MAD | 420.6 | 423.7 | 13.2 | 416.6 | 417.8 | 14.1 | 418.6 | 422.0 | 14.4 | 408.6 | 410.0 | 11.5 | 420.6 | 423.7 | 12.0 | | |
| SAF | 410.6 | 410.8 | 7.8 | 400.5 | 400.9 | 7.3 | 406.6 | 406.1 | 6.8 | 408.6 | 408.8 | 6.9 | 406.6 | 407.2 | 6.3 | | |

Table S3. d410 depths for each region within the five 3D time-to-depth corrected CCP stacks. MED. = Median, MN. = Mean, S.T.D. = Standard Deviation. All values presented in kilometers.

| Region | CCP d660 depths (km) | | | | | | | | | | | | | | | | |
|--------|----------------------|-------|--------|-------|------------|--------|-------|-------|------------|-------|-------|--------|------------|-------|--------|------|----------------|
| | AFRP22-CCP | | | | AF2019-CCP | | | | SL2013-CCP | | | | SEMUCB-CCP | | | | SGLOBEmani-CCP |
| | MED. | MN. | S.T.D. | MED. | MN. | S.T.D. | MED. | MN. | S.T.D. | MED. | MN. | S.T.D. | MED. | MN. | S.T.D. | MN. | S.T.D. |
| AFR | 677.0 | 676.3 | 10.8 | 655.0 | 654.5 | 10.2 | 659.0 | 660.0 | 10.1 | 655.0 | 654.1 | 10.1 | 665.0 | 666.7 | 666.7 | 9.7 | |
| EYP | 669.0 | 668.8 | 7.1 | 657.0 | 657.3 | 6.1 | 659.0 | 659.8 | 6.3 | 648.9 | 648.7 | 8.5 | 667.0 | 667.3 | 667.3 | 5.7 | |
| TD | 688.0 | 687.4 | 5.5 | 659.0 | 658.7 | 7.4 | 661.0 | 661.2 | 6.7 | 648.9 | 650.3 | 10.9 | 673.0 | 674.1 | 674.1 | 6.9 | |
| EAP | 687.0 | 685.4 | 4.2 | 661.0 | 661.3 | 6.8 | 667.0 | 666.1 | 6.6 | 660.0 | 659.8 | 7.8 | 673.0 | 673.1 | 673.1 | 7.2 | |
| CAM | 679.0 | 677.9 | 9.5 | 648.9 | 650.5 | 11.0 | 655.0 | 657.0 | 10.1 | 657.0 | 655.4 | 10.2 | 663.0 | 667.4 | 667.4 | 10.7 | |
| MAD | 673.0 | 674.3 | 8.7 | 655.0 | 656.8 | 8.0 | 663.0 | 666.0 | 10.7 | 644.9 | 645.7 | 7.2 | 670.0 | 670.5 | 670.5 | 8.8 | |
| SAF | 673.0 | 670.8 | 9.9 | 648.9 | 647.2 | 8.9 | 653.0 | 653.8 | 6.5 | 653.0 | 653.1 | 7.6 | 659.0 | 659.4 | 659.4 | 5.7 | |

Table S4. d660 depths for each region within the five 3D time-to-depth corrected CCP stacks. MED. = Median, MN. = Mean, S.T.D. = Standard Deviation. All values presented in kilometers.

| Region | CCP MTZ thickness (km) | | | | | | | | | | | | | | | | SGLOBEmani-CCP | |
|--------|------------------------|-------|--------|-------|------------|--------|-------|-------|------------|-------|-------|--------|------------|-------|--------|------|----------------|--------|
| | AFRP22-CCP | | | | AF2019-CCP | | | | SL2013-CCP | | | | SEMUCB-CCP | | | | SGLOBEmani-CCP | |
| | MED. | MN. | S.T.D. | MED. | MN. | S.T.D. | MED. | MN. | S.T.D. | MED. | MN. | S.T.D. | MED. | MN. | S.T.D. | MED. | MN. | S.T.D. |
| AFR | 254.4 | 255.0 | 11.4 | 244.4 | 243.9 | 9.5 | 246.4 | 245.9 | 9.4 | 242.4 | 242.8 | 9.9 | 250.4 | 250.1 | 10.4 | | | |
| EYP | 246.4 | 246.2 | 7.7 | 244.4 | 243.7 | 7.8 | 244.4 | 244.4 | 8.3 | 242.4 | 241.8 | 8.2 | 248.4 | 249.1 | 9.7 | | | |
| TD | 246.4 | 246.5 | 9.6 | 240.4 | 240.1 | 8.6 | 240.4 | 240.1 | 9.3 | 236.4 | 236.7 | 11.6 | 242.4 | 243.1 | 10.4 | | | |
| EAP | 250.4 | 251.6 | 9.8 | 240.4 | 240.9 | 7.7 | 244.4 | 243.8 | 6.8 | 240.4 | 240.6 | 8.2 | 248.4 | 248.1 | 10.5 | | | |
| CAM | 268.4 | 263.9 | 15.2 | 248.4 | 243.8 | 12.0 | 254.4 | 250.5 | 12.6 | 252.4 | 248.0 | 15.3 | 263.4 | 257.9 | 15.4 | | | |
| MAD | 248.4 | 248.6 | 11.8 | 236.4 | 237.2 | 10.9 | 240.4 | 241.2 | 10.8 | 234.4 | 234.4 | 10.2 | 244.4 | 244.7 | 10.9 | | | |
| SAF | 260.4 | 260.2 | 7.8 | 244.4 | 245.3 | 8.1 | 246.4 | 247.0 | 7.9 | 244.4 | 244.9 | 7.8 | 252.4 | 251.2 | 7.6 | | | |

Table S5. MTZ thickness for each region within the five 3D time-to-depth corrected CCP stacks. MED. = Median, MN. = Mean, S.T.D. = Standard Deviation.

All values presented in kilometers.

References

- Andriampenomanana, F., Nyblade, A. A., Durrheim, R., Tugume, F., & Nyago, J. (2021). Shear wave splitting measurements in northeastern Uganda and southeastern Tanzania: corroborating evidence for sublithospheric mantle flow beneath East Africa [Dataset]. *Geophys. J. Int.*, 226(3), 1696-1704. doi: 10.1093/gji/ggab167
- Bastow, I. D. (2019). *Turkana Rift Arrays to Investigate Lithospheric Strains (TRAILS) - UK component* [Dataset]. International Federation of Digital Seismograph Networks. (Seismic Network) doi: 10.7914/SN/9A_2019
- Boyce, A., Bastow, I. D., Cottaar, S., Kounoudis, R., Guilloud De Courbeville, J., Caunt, E., & Desai, S. (2021). AFRP20: New P-wavespeed Model for the African Mantle Reveals Two Whole-Mantle Plumes Below East Africa and Neoproterozoic Modification of the Tanzania Craton. *Geochem. Geophys. Geosyst.*, 22(3). doi: 10.1029/2020GC009302
- Boyce, A., Bastow, I. D., Rondenay, S., & Van der Hilst, R. D. (2017). From relative to absolute teleseismic travel-times: the Absolute Arrival-time Recovery Method (AARM) [Software]. *Bull. Seis. Soc. Am.*, 107(5), 2511–2520. doi: 10.1785/0120170021
- Boyce, A., & Cottaar, S. (2021). Insights into Deep Mantle Thermochemical Contributions to African Magmatism from Converted Seismic Phases. *Geochem. Geophys. Geosyst.*, 22(3). doi: 10.1029/2020GC009478
- Braile, L., Wang, B., Daudt, C., Keller, G., & Patel, J. P. (1994). Modeling the 2-D seismic velocity structure across the Kenya rift. *Tectonophysics*, 236(1-4), 251–269.
- Celli, N. L., Lebedev, S., Schaeffer, A. J., & Gaina, C. (2020). African cratonic lithosphere carved by mantle plumes. *Nat. Comms.*, 11(1), 92. doi: 10.1038/s41467-019-13871-2
- Chang, S. J., Ferreira, A. M. G., Ritsema, J., Van Heijst, H.-J., & Woodhouse, J. H. (2015). Joint inversion for global isotropic and radially anisotropic mantle structure including crustal thickness perturbations. *J. Geophys. Res.*, 120(6), 4278–4300. doi: 10.1002/2014jb011824
- Durrheim, R. J., & Nyblade, A. A. (2009). AfricaArray Special Volume – Introduction [Dataset]. *South African Journal of Geology*, 112, 209-212.

- Ebinger, C. J. (2018). *Crust and mantle structure and the expression of extension in the Turkana Depression of Kenya and Ethiopia* [Dataset]. International Federation of Digital Seismograph Networks. (Seismic Network) doi: 10.7914/SN/Y1_2018
- Engdahl, E. R., Van der Hilst, R. D., & Buland, R. (1998). Global teleseismic earthquake relocation with improved travel times and procedures for depth determination. *Bull. Seis. Soc. Am.*, 88(3), 722–743.
- Fonseca, J. F. B. D., Chamussa, J., Domingues, A., Helffrich, G., Antunes, E., van Aswegen, G., ... Manhiça, V. J. (2014). MOZART: A Seismological Investigation of the East African Rift in Central Mozambique [Dataset]. *Seis. Res. Lett.*, 85(1), 108-116. doi: 10.1785/0220130082
- French, S. W., & Romanowicz, B. (2014). Whole-mantle radially anisotropic shear velocity structure from spectral-element waveform tomography. *Geophys. J. Int.*, 199(3), 1303–1327. doi: 10.1093/gji/ggu334
- Heit, B., Yuan, X., Weber, M., Geissler, W., Jokat, W., Lushetile, B., & Hoffmann, K. (2015). Crustal thickness and Vp/Vs ratio in NW Namibia from receiver functions: Evidence for magmatic underplating due to mantle plume-crust interaction. *Geophys. Res. Lett.*, 42(9). doi: 10.1002/2015gl063704
- Helffrich, G. R., & Fonseca, J. F. B. D. (2011). *Mozambique Rift Tomography* [Dataset]. International Federation of Digital Seismograph Networks. (Seismic Network) doi: 10.7914/SN/6H_2011
- Hosseini, K., Sigloch, K., Tsekhnistrenko, M., Zaheri, A., Nissen-Meyer, T., & Igel, H. (2019). Global mantle structure from multifrequency tomography using P, PP and P-diffracted waves. *Geophys. J. Int.*, 220(1), 96–141. doi: 10.1093/gji/ggz394
- Kennett, B. L. N., & Gudmundsson, O. (1996). Ellipticity corrections for seismic phases. *Geophys. J. Int.*, 127(1), 40–48. doi: 10.1111/j.1365-246x.1996.tb01533.x
- Kounoudis, R., Bastow, I. D., Ebinger, C. J., Ogden, C. S., Ayele, A., Bendick, R., ... Kibret, B. (2021). Body-Wave Tomographic Imaging of the Turkana Depression: Implications for Rift Development and Plume-Lithosphere Interactions [Dataset]. *Geochem. Geophys. Geosyst.*, 22(8). doi: 10.1029/2021gc009782

- Laske, G., Masters, G., Ma, Z., & Pasyanos, M. E. (2013). Update on CRUST1.0 - A 1-degree Global Model of Earth's Crust. In *Geophys. res. abstracts, 15, abstract egu2013-2658* (p. EGU2013-2658).
- Li, C., Van der Hilst, R. D., Engdahl, R., & Burdick, S. (2008). A new global model for P wave speed variations in Earth's mantle. *Geochem. Geophys. Geosyst.*, 9(5). doi: 10.1029/2007GC001806
- Lu, C., Grand, S. P., Lai, H., & Garnero, E. J. (2019). TX2019slab: A New P and S Tomography Model Incorporating Subducting Slabs. *J. Geophys. Res.*, 124(11), 11549–11567. doi: 10.1029/2019jb017448
- Mechie, J., Keller, G., Prodehl, C., Gaciri, S., Braile, L., Mooney, W., ... Sandmeier, K. (1994). Crustal structure beneath the Kenya Rift from axial profile data. *Tectonophysics*, 236(1-4), 179–200.
- Montelli, R., Nolet, G., Dahlen, F., & Masters, G. (2006). A catalogue of deep mantle plumes: new results from finite-frequency tomography. *Geochem. Geophys. Geosyst.*, 7, Q11007. doi: 10.1029/2006GC001248
- Nyblade, A. A. (2015). *AfricaArray - Namibia* [Dataset]. IRIS. (Seismic Network) doi: 10.7914/SN/8A_2015
- Nyblade, A. A. (2017). *Broadband seismic experiment in NE Uganda to investigate plume-lithosphere interactions* [Dataset]. International Federation of Digital Seismograph Networks. (Seismic Network) doi: 10.7914/SN/XW_2017
- Ogden, C. S., Bastow, I. D., Ebinger, C. J., Ayele, A., Kounoudis, R., Musila, M., ... Kibret, B. (2023). The development of multiple phases of superposed rifting in the Turkana Depression, East Africa: Evidence from receiver functions. *Earth Planet. Sci. Lett.*, 609, 118088. doi: 10.1016/j.epsl.2023.118088
- Prodehl, C., Jacob, A., Thybo, H., Dindi, E., & Stangl, R. (1994). Crustal structure on the northeastern flank of the Kenya rift. *Tectonophysics*, 236(1-4), 271–290.
- Ritsema, J., & Van Heijst, H.-J. (2002). Constraints on the correlation of P- and S-wave velocity heterogeneity in the mantle from P, PP, PPP and PKPab traveltimes. *Geophys. J. Int.*, 149(2), 482–489. doi: 10.1046/j.1365-246x.2002.01631.x
- Schaeffer, A., & Lebedev, S. (2013). Global shear speed structure of the upper mantle and transition zone. *Geophys. J. Int.*, 194(1), 417–449. doi: 10.1093/gji/gji/

ggt095

- Simmons, N. A., Myers, S. C., Johannesson, G., & Matzel, E. (2012). LLNL-G3Dv3: Global P wave tomography model for improved regional and teleseismic travel time prediction. *J. Geophys. Res.*, 117(B10). doi: 10.1029/2012jb009525
- Tesoniero, A., Cammarano, F., & Boschi, L. (2016). S-to-P heterogeneity ratio in the lower mantle and thermo-chemical implications. *Geochem. Geophys. Geosyst.*, 17(7), 2522–2538. doi: 10.1002/2016gc006293
- van Stiphout, A. M., Cottaar, S., & Deuss, A. (2019). Receiver function mapping of mantle transition zone discontinuities beneath Alaska using scaled 3-D velocity corrections. *Geophys. J. Int.*, 219(2), 1432–1446. doi: 10.1093/gji/ggz360
- VanDecar, J., & Crosson, R. (1990). Determination of teleseismic relative phase arrival times using multi-channel cross-correlation and least squares. *Bull. Seis. Soc. Am.*, 80(1), 150–169.